1949

Light-induced non-adiabatic processes in diatomic systems

Doctoral (PhD) dissertation

Péter Badankó
Supervisor: Dr. Ágnes Vibók

University of Debrecen
Doctoral Committee of Natural Sciences and Information Technology
Doctoral School of Physics
Debrecen, 2020.

Ezen értekezést a Debreceni Egyetem Természettudományi és Informatikai Doktori Tanács Fizikai Tudományok Doktori Iskolája Atom- és molekulafizika programja keretében készítettem a Debreceni Egyetem természettudományi doktori (PhD) fokozatának elnyerése céljából.

Nyilatkozom arról, hogy a tézisekben leírt eredmények nem képezik más PhD disszertáció részét.

Debrecen, 2020.

Badankó Péter
doktorjelölt

Tanúsítom, hogy Badankó Péter doktorjelölt 2014-2020 között a fent megnevezett Doktori Iskola Atom- és molekulafizika programjának keretében irányításommal végezte munkáját. Az értekezésben foglalt eredményekhez a jelölt önálló alkotó tevékenységével meghatározóan hozzájárult.

Nyilatkozom továbbá arról, hogy a tézisekben leírt eredmények nem képezik más PhD disszertáció részét. Az értekezés elfogadását javasolom.

Debrecen, 2020.

Vibók Ágnes
témavezető

Light-induced non-adiabatic processes in diatomic systems

Értekezés a doktori (Ph.D.) fokozat megszerzése érdekében a fizika tudományágban

Írta: Badankó Péter okleveles fizikus

Készült a Debreceni Egyetem Fizikai Tudományok Doktori Iskolája Atom- és molekulafizika programja keretében

Témavezető: Dr. Vibók Ágnes

A doktori szigorlati bizottság:

elnök:	Dr.	.....
tagok:	Dr.	.....
	Dr.	.....

A doktori szigorlat időpontja: .....

Az értekezés bírálói:

Dr.	.....
Dr.	.....

A bírálóbizottság:

elnök:	Dr.	.....
tagok:	Dr.	.....
	Dr.	.....
	Dr.	.....
	Dr.	.....

Az értekezés védésének időpontja: .....

Contents

Glossary of frequently used abbreviations

AC – Avoided Crossing

ADT – Adiabatic-to-diabatic transformation

AO – Atomic Orbital

aug-cc-pVQZ – augmented correlation-consistent polarized Valence Quadruple Zeta

BO – Born-Oppenheimer

CAP – Complex Absorbing Potential

CASSCF – Complete Active Space Self-Consistent Field

CI – Conical Intersection or Configuration Interaction

CSF – Configuration State Function

DCI – Doubly Configuration Interaction

DVR – Discrete Variable Representation

DZ – Double Zeta

FCI – Full Configuration Interaction

FFT-DVR – Fast Fourier-Transformation Discrete Variable Representation

FWHM – Full Width At Half-Maximum

GTO – Gaussian Type Orbital

HF – Hartree-Fock

HFR – Hartree-Fock-Roothan

KER – Kinetic Energy Release

LCAO – Linear Combination of Atomic Orbitals

LIAC – Light-Induced Avoided Crossing

LICI – Light-Induced Conical Intersection

MC – Multi-Configuration

MCTDH – Multi-configuration time-dependent Hartree

MCSCF – Multi-Configuration Self-Consistent Field

MRCI – Multi-Reference Configuration Interaction

NACT – Non-Adiabatic Coupling Term

PBF – Primitive Basis Function

PDM – Permanent Dipole Moment

RHF – Restricted Hartree-Fock

RWA – Rotating Wave Approximation

SCF – Self-Consistent Field

SDCI – Singly-Doubly Configuration Interaction

SPF – Single-Particle Function

STO – Slater-Type Orbital

STO-NG – Slater-Type N-Gaussian

TDH – Time-Dependent Hartree

TDM – Transition Dipole Moment

TDSE – Time-Dependent Schrödinger-equation

TISE – Time-Independent Schrödinger-equation

TZ – Triple-Zeta

UHF – Unrestricted Hartree-Fock

Introduction

The following dissertation compiles the results that have been achieved during my PhD studies in the Doctoral School of Physics in Debrecen between 2014 and 2017, complemented by the results of another year of research conducted from 2017 to 2018. Most compelling to me with these works was the deep and direct links to possible experimental setups, either already done, planned or expected in the future.

In my research I studied the dynamics, particularly non-adiabatic dynamics of the nuclei of small diatomic systems such as D_2^+, MgH^+ or LiF. Non-adiabatic effects play an important role in several biological, chemical and physical processes. Their significance becomes more and more apparent as the potential energies of the electronic states included in the dynamical description approach each other more and more closely, eventually becoming degenerate. Their impact on the nuclear dynamics can then be quantitatively addressed by comparing, for example, the results of a calculation made within the framework of the Born-Oppenheimer-approximation which neglects the non-adiabatic couplings, and different calculations which take them into account. The breakdown of the BO-approximation has been studied extensively over the past decades giving rise to the theory and reviews that go past the BO-method [1–4].

It has also been shown, first by Hund [5], that potential energy curves of diatomic molecules cannot cross in general, unless the corresponding electronic states differ either in their symmetry, multiplicity or some other important property [6]. In general, there are two independent conditions that are needed to be satisfied so that a crossing can be formed. This requires at least two degrees of freedom to be present in the system and diatomic systems provide only one, the vibrational degrees of freedom associated to the relative motions of atoms constituting the molecule. Therefore, only avoided crossings can be formed, as stated by the non-crossing rule [7].

On the other hand, in polyatomic systems, due to the large number of degrees of freedom present, the crossings between electronic states are more abundant and they give rise to several non-adiabatic processes. In

polyatomic molecules these degeneracies are given by nature and they are intrinsic properties of the system.

It has been shown recently that light-induced crossings can be formed even in diatomic molecules, when the molecule is subjected to an external laser field [8, 9]. In this case the angle between the polarisation direction of the field and the direction of the transition dipole can deliver the missing degree of freedom that is needed to form a crossing between the electronic states. These resulting degeneracies are called light-induced conical intersections (LICIs) and they behave similarly to their naturally present counterpart, except for a significant difference. For conical intersections that are intrinsic to the molecule, the position and strength of the degeneracy can not be easily modified. In contrast, the position of a light-induced CI can be shifted to different internuclear positions by varying the frequency of the laser field and their strength, on the other hand, can be controlled by the intensity of the laser field. This makes the manipulation of LICIs by the above means possible, establishing new prospects in the field of quantum control of molecular dynamics and processes.

Although in my research I only studied simple diatomic systems, what made these works interesting is, that all of them was focused on some aspect of light-induced non-adiabatic effects.

My results include the calculation of Berry's phase of a LICI for which there are only a few results [10, 11] in the literature. My objective was to complement those earlier findings with the implementation of an adiabatic time-dependent approach. Within this framework I calculated Berry's phase for a LICI.

Another study was focused on the so called vibrational trapping effect. The vibrational trapping presents a straightforward explanation for the findings where using a particular field frequency leads to suppressed dissociation rates. The explanation relies on the difference of diabatic and adiabatic eigenenergies and the similarity of the diabatic and adiabatic eigenfunctions. The main purpose of my work here was to put the bases of the above explanation to a quantitative test in the case of D_2^+. A new finding of this work is also presented that claims the nodal structure of the diabatic eigenstates to be of importance.

Two other, in several ways more complex systems discussed in this dissertation are the LiF and MgH^+ molecules. In case of the former, an electronic state that is often neglected in the literature was included in the dynamical calculations. This system also possesses an avoided crossing between its two lowest lying Σ electronic states, resulting in non-adiabatic dynamics even under field-free conditions.

As for the case of MgH^+, the dynamical studies were motivated by the fact that beside the system having a permanent dipole moment (PDM), it has also got a transition dipole moment (TDM) that is perpendicular to the PDM of the molecule. Utilising a model system in which the TDM is artificially rotated in such a way that it becomes parallel to the PDM, I found significant differences in the angular distribution of the photofragments.

The main parts of this dissertation are structured as follows.

Chapter 1 provides some general theoretical background that are either frequently used in computational chemistry/physical chemistry or hold some special historical significance. Describing these parts, I will mostly confine the discussion to the elements of theory which are the most relevant to the computational methods I have used throughout my simulations.

From Chapter 2 through Chapter 5, the results of my research dealing with the vibrational trapping in D_2^+ , calculation of Berry's phase, the studies with MgH^+ and LiF will be presented and discussed in detail.
A common feature of these chapters is that all of them sets off by touching on some of the works relevant to my results and I also describe what motivated the project at hand.

Chapter 6 gives a brief summary of my results with Chapter 7 repeating the same in Hungarian.

Chapter 1

Theoretical background

This chapter summarizes the most important elements of the theory which are, at least in some aspects, relevant to my results. These include the cornerstone of the earliest results of computational chemistry, the Born-Oppenheimer-approximation. From now on, I will often use the abbreviation BO to refer to quantities obtained within this framework, eg. BO-eigenenergies, BO-states. Although many challenges of modern computational chemistry require more sophisticated methods than the BO-approximation [12], still, its results can be useful in several cases, for example BO-wave functions may serve as initial states to more sophisticated analyses. Additionally, its historical significance can be hardly overemphasized and in many introductory courses to atomic physics or quantum chemistry it serves as the first approximation that is discussed.

My simulations of nuclear dynamics often needed supporting calculations to be made that provide the potential energy surfaces, electronic dipoles (PDM, TDM) or non-adiabatic coupling terms (NACT). I determined these quantities with the help of the MOLPRO package [13] which is widely used for electronic structure calculations. There are many methods in electronic structure theory that can be used to obtain the above quantities. I will mention three of them that I have used to support the nuclear dynamical calculations with LiF and MgH^+. These are the Hartree-Fock (HF), Complete Active Space Self-Consistent Field (CASSCF) and Multi-Reference Configurational Interaction (MRCI) methods. The HF-method is considered in more details due to its role as a stepping-stone in all of the electronic structure calculations I have carried out.

Once the proper quantities from an electronic structure calculation have been obtained, they serve as an input to the quantum dynamical simulations of the nuclei and the time-dependent Schrödinger equation

is solved. To carry out these, I have utilised the Heidelberg Multi-Configurational Time-Dependent Hartree [14–16] (MCTDH) package. The details of this method will be discussed in detail as well.

In the case of the calculation of Berry's phase, I wrote a computer code in C language that relied on the numerical integrators implemented in the GNU Scientific Library [17] (GSL) to evaluate the path integrals needed.

The chapter of the background theory closes with a brief description of the Floquet-method, a framework I used during different phases of my studies.

1.1 Born-Oppenheimer approximation

Let us consider a molecular system consisting of N_C nuclei and n_e electrons. Let $\vec{R}_\alpha$, M_α and $Z_\alpha e$ denote the position, mass and charge of the αth nuclei, respectively. Similarly, $\vec{r}_i$ stands for the position of the ith electron in the system and m_e is the mass of the electron. Then the Hamiltonian of the full system takes the form

$$\begin{aligned}\hat{H} = &\sum_{\alpha=1}^{N_C} -\frac{\hbar^2}{2M_\alpha}\nabla^2_{R_\alpha} + \sum_{i=1}^{n_e} -\frac{\hbar^2}{2m_e}\nabla^2_{r_i} + \\ &+ \sum_{\alpha=1}^{N_C}\sum_{\substack{\beta=1\\ \beta>\alpha}}^{N_C} \frac{1}{4\pi\varepsilon_0}\frac{Z_\alpha Z_\beta e^2}{|\vec{R}_\alpha - \vec{R}_\beta|} + \sum_{i=1}^{n_e}\sum_{\substack{j=1\\ j>i}}^{n_e} \frac{1}{4\pi\varepsilon_0}\frac{e^2}{|\vec{r}_i - \vec{r}_j|} + \\ &- \sum_{\alpha=1}^{N_C}\sum_{i=1}^{n_e} \frac{1}{4\pi\varepsilon_0}\frac{Z_\alpha e^2}{|\vec{R}_\alpha - \vec{r}_i|},\end{aligned} \tag{1.1.1}$$

where $\nabla^2_{R_\alpha}$ and $\nabla^2_{r_i}$ stands for derivation with respect to the coordinates of the αth nuclei and ith electron, respectively. $\hbar$ and ε_0 as usual, denote the reduced Planck's constant and the vacuum permittivity. The first two terms in $\hat{H}$ constitute the kinetic energy operators of the system for the nuclei and the electrons, $\hat{T} = \hat{T}_N + \hat{T}_e$. The next pair of terms describe the repulsive Coulomb-interaction between any pair of nuclei, V_{NN}, and electrons, V_{ee}. The last term is responsible for the interaction holding the system together, the attraction between the electrons and nuclei, V_{Ne}.

It is favorable in atomic physics and quantum chemistry calculations to use the system of atomic units. In this case $\hbar, m_e, \frac{1}{4\pi\varepsilon_0}$ and e are all taken to be unity. This way eq. (1.1.1) takes a simpler form. From now on, I will continue using atomic units.

The Born-Oppenheimer-approximation takes advantage of the fact that $m_e/M_\alpha \approx 1/1860$, that is, the nuclei are much heavier, therefore, slower than the electrons. This makes reasonable to imagine the dynamics determined by eq. (1.1.1) from the perspective of the electrons as one where the nuclei are frozen: the electrons, since they are much lighter, can instantaneously respond to any change in the arrangement of the nuclei. In this situation it is possible to separate the dynamics of the electrons and nuclei. The wave function $\psi(\{\vec{R}\}, \{\vec{r}\})$ can be written as

$$\psi(\{\vec{R}\}, \{\vec{r}\}) = \chi(\{\vec{R}\}) \cdot \phi(\{\vec{r}\}; \{\vec{R}\}). \tag{1.1.2}$$

Here $\{\vec{R}\}$ and $\{\vec{r}\}$ denote the set of coordinates of all nuclei and all electrons, respectively. χ is the nuclear wave function and ϕ signs the

electronic wave function which contains only a parametric dependence on the positions of all nuclei. Substituting the ansatz eq. (1.1.2) into the full Hamiltonian in eq. (1.1.1), the time-independent Schrödinger-equation (TISE), $\hat{H}\psi = E\psi$, gives,

$$\hat{H}\psi = \left\{\hat{T}_N + \hat{H}_e\right\}\psi = \left\{\hat{T}_N + \hat{H}_e\right\}\chi\cdot\phi = \hat{T}_N\chi\phi + \chi\hat{H}_e\phi = E\chi\phi. \tag{1.1.3}$$

Evaluating $\hat{T}_N\chi\phi$ yields

$$\begin{aligned}\hat{T}_N\chi\phi &= \sum_{\alpha=1}^{N_C} -\frac{1}{2M_\alpha}\nabla_{R_\alpha}^2\chi\cdot\phi = \sum_{\alpha=1}^{N_C} -\frac{1}{2M_\alpha}\left\{\frac{\partial^2}{\partial X_\alpha^2} + \frac{\partial^2}{\partial Y_\alpha^2} + \frac{\partial^2}{\partial Z_\alpha^2}\right\}\chi\cdot\phi = \\ &= \phi\hat{T}_N\chi + \sum_{\alpha=1}^{N_C} -\frac{1}{2M_\alpha}\left\{\chi\nabla_{R_\alpha}^2\phi + 2\cdot(\nabla_{R_\alpha}\chi)\cdot(\nabla_{R_\alpha}\phi)\right\} = \\ &= \phi\hat{T}_N\chi + \sum_{\alpha=1}^{N_C} -\frac{1}{2M_\alpha}D_{R_\alpha}^{\phi\chi}.\end{aligned} \tag{1.1.4}$$

In the last term a shorthand-notation $D_{R_\alpha}^{\phi\chi}$ for the quantity in braces is introduced. Since ϕ depends on the nuclear geometry $\{\vec{R}\}$ parametrically, $D_{R_\alpha}^{\phi\chi}$ differs from 0 in general. On the other hand, it is also weighted by $\frac{1}{2M_\alpha}$, therefore, the sum can be assumed to be small and neglected. Doing so results in the approximation

$$\hat{T}_N\chi\phi \approx \phi\hat{T}_N\chi. \tag{1.1.5}$$

Substituting this result back into eq. (1.1.3) yields

$$\phi\hat{T}_N\chi + \chi\hat{H}_e\phi = \phi\hat{T}_N\chi + \chi\hat{T}_e\phi + V\chi\phi = \phi\hat{T}_N\chi + (\hat{T}_e\phi + V\phi)\chi = E\chi\phi \tag{1.1.6}$$

Following standard procedures [18], eq. (1.1.6) is solved in two steps. First the electronic TISE,

$$\hat{T}_e\phi + V\phi = E_e(\{\vec{R}\})\phi \tag{1.1.7}$$

is to be solved, where $E_e(\{\vec{R}\})$ is the electronic energy corresponding to a particular $\{\vec{R}\}$ arrangement of the nuclei. Eq. (1.1.7), being an eigenvalue-equation, has in general several $\phi_i(\{\vec{r}\};\{\vec{R}\})$ and $E_{e_i}(\{\vec{R}\})$ $(i = 1, 2, \dots)$ solutions for a fixed nuclear geometry $\{\vec{R}\}$. Moreover, the procedure of solving eq. (1.1.7) must be repeated for several different

nuclear geometries $\{\vec{R}\}$ of interest. This procedure provides the BO-potential energy surfaces as the geometry is varied.

In the second step, the electronic BO-eigenenergies $E_{e_i}(\{\vec{R}\})$ are put into eq. (1.1.6)

$$\phi_i \hat{T}_N \chi + E_{e_i}(\{\vec{R}\})\phi_i \chi = E\chi\phi_i \tag{1.1.8}$$

which, upon canceling by ϕ_i, simplifies to

$$\hat{T}_N \chi + E_{e_i}(\{\vec{R}\})\chi = E\chi. \tag{1.1.9}$$

This is the TISE for the nuclei in the ith (BO) electronic state, where the electronic eigenenergies provide the potential energy for the nuclear motion and E is the eigenenergy of the nuclei in the BO-scheme.

Since the approximation in eq. (1.1.5) was used, it is clear that the solutions acquired are not exact. In particular, neglecting $\sum_{\alpha=1}^{N_C} -\frac{1}{2M_\alpha} D_{R_\alpha}^{\phi\chi}$ in the effect of $\hat{T}_N$ on $\chi \cdot \phi$ means neglecting the so called non-adiabatic effects between the electronic states. These can be very significant around geometries where different electronic states get very close to each other energetically, as it was mentioned in the introduction earlier. This also means a stronger parametric dependence of ϕ on the geometry $\{\vec{R}\}$. The electronic and nuclear degrees of freedom become more strongly coupled, eventually leading to the breakdown of the BO-approximation and the separation in eq. (1.1.2) does not hold anymore.

In some cases it might be reasonable to take into account an average of non-adiabatic effects with respect to a particular electronic eigenfunction ϕ':

$$\begin{aligned}
&\Big\langle \sum_{\alpha=1}^{N_C} -\frac{1}{2M_\alpha} D_{R_\alpha}^{\phi'\chi} \Big\rangle = \sum_{\alpha=1}^{N_C} -\frac{1}{2M_\alpha} \times \\
&\times \int_{-\infty}^{\infty} \dots \int_{-\infty}^{\infty} \phi'^{*} (\chi \nabla_{R_\alpha}^2 + 2 \cdot (\nabla_{R_\alpha}\chi) \cdot \nabla_{R_\alpha}) \phi' \prod_{i=1}^{n_e} d\vec{r_i} = \\
&= \sum_{\alpha=1}^{N_C} -\frac{1}{2M_\alpha} \Big(\chi \langle \phi' | \nabla_{R_\alpha}^2 | \phi' \rangle + 2 \cdot (\nabla_{R_\alpha}\chi) \cdot \langle \phi' | \nabla_{R_\alpha} | \phi' \rangle \Big),
\end{aligned} \tag{1.1.10}$$

making use of the bracket notation in the last equality. This average can then be added to the left hand side of eq. (1.1.9) when solving the nuclear TISE. Using an average such as above is often called adiabatic approximation.

1.2 Adiabatic and diabatic frameworks

In some cases of chemical and physical interest, the approximation used in eq. (1.1.5) cannot be justified. Typically these are systems that inherently contain some source of non-adiabaticity, for example systems with avoided crossings (AC) or conical intersections (CI). In those situations, the full expression for $\hat{T}_N\chi\phi$, as it is shown in eq. (1.1.4), must be taken into account. However, by treating those terms accordingly, one admits off-diagonal elements into the kinetic energy part of the Hamiltonian of the system.

In the simple case of two electronic states, the evolution of the nuclei that takes place on the two electronic states gets coupled by off-diagonal elements of kinetic energy terms. Since these are operators and contain derivatives, it is worth considering a unitary transformation that is capable of getting rid of these terms and makes the equations of motion easier to handle numerically. The corresponding transformation is called the adiabatic-to-diabatic transformation (ADT) [2–4, 19]. For two-state systems, this transformation U_{ADT} can be given by

$$U_{\mathrm{ADT}} = \begin{pmatrix} \cos\gamma(\vec{R}) & \sin\gamma(\vec{R}) \\ -\sin\gamma(\vec{R}) & \cos\gamma(\vec{R}) \end{pmatrix}, \tag{1.2.1}$$

where $\gamma(\vec{R})$ is the ADT angle and depends on the geometry $\{\vec{R}\}$ of all nuclei. With the aid of U_{ADT} the transformation $U_{\mathrm{ADT}}\hat{H}_{\mathrm{N,adi}}U_{\mathrm{ADT}}^{\dagger}$ is applied to the nuclear Hamiltonian $\hat{H}_{\mathrm{N,adi}}$

$$\hat{H}_{\mathrm{N,adi}} = \hat{T}_{\mathrm{N,adi}} + \hat{V}_{N,\mathrm{adi}}. \tag{1.2.2}$$

$\hat{H}_{\mathrm{N,adi}}$ is similar to the BO nuclear Hamiltonian given in eq. (1.1.9) but, in contrast to that, the $\hat{T}_{\mathrm{N,adi}}$ kinetic operator also contains terms in the form of $\sum_{\alpha=1}^{N_C} -\frac{1}{2M_\alpha} D_{R_\alpha}^{\phi\chi}$ and $\hat{V}_{\mathrm{N,adi}}$ denotes the diagonal matrix containing the adiabatic potential energy surfaces calculated within the Born-Oppenheimer-scheme.
U_{ADT} is specifically chosen such that it diagonalises $\hat{T}_{\mathrm{N,adi}}$. Although performing the above transformation removes the off-diagonal kinetic energy terms from $\hat{T}_{N,\mathrm{adi}}$, it is achieved at the expense of the appeareance of off-diagonal potential energy terms in the $\hat{V}_{N,\mathrm{dia}} = U_{\mathrm{ADT}}\hat{V}_{N,\mathrm{adi}}U_{\mathrm{ADT}}^{\dagger}$ transformed diabatic potential energy.

Although the diabatic framework derived with the ADT transformation cannot be done in every cases exactly, but an approximately diagonal form of $\hat{T}_{N,\mathrm{dia}}$ can be obtained with small enough off-diagonal terms so

that neglecting them is justifiable. Due to this, the diabatic framework is widely used in the field of non-adiabatic dynamics. However, since the transformation angle $\gamma(\vec{R})$ needs to be determined at every possible nuclear geometry, its calculation proves to be challenging in higher dimensions and it is one of the important tasks of computational non-adiabatic chemistry.

1.3 Electronic structure calculations

Working with molecular dynamics always requires one to prepare precise data characterising the potential energy surfaces and dipole moments of the system under investigation. These then can be used in subsequent simulations of molecular dynamics. In some cases there are analytical functions available that can be used, but more often than not, providing such data (commonly summed up as the electronic structure of the system) is a very challenging task computationally. This is even more pronounced in cases when the system possesses features that requires enhanced precision, as it may happen in close vicinity of avoided crossings or conical intersections, for example.

1.3.1 Hartree-Fock method

The Hartree-Fock (HF) method presents the simplest approach to electronic structure calculations as it only takes a single Slater-determinant into account to describe the wave function of the system. The resulting equations that can be derived using variational theory from the Brillouin theorem carry very expressive physical meaning; each of the electrons present in the system perceive an averaged potential due to the presence of all the other electrons. That is the reason why the HF method is also often called the independent electron approximation. Although, this is a rather crude way of treating the interaction between the electrons, nonetheless the HF method is still very useful and in most cases serves as the starting point for calculations that are more refined. This alone validates a brief description of the HF method in works that are related to electronic structure calculations.
At several points throughout the derivations I am leaning on [20] for the more crucial considerations leading up to the most important results.

The starting point is a Slater-determinant of the form

$$\psi(1,2,\ldots,N) = \frac{1}{\sqrt{N!}} \begin{vmatrix} \psi_1(1) & \psi_2(1) & \cdots & \psi_N(1) \\ \psi_1(2) & \psi_2(2) & \cdots & \psi_N(2) \\ \vdots & \vdots & \ddots & \vdots \\ \psi_1(N) & \psi_2(N) & \cdots & \psi_N(N) \end{vmatrix}. \tag{1.3.1}$$

The above is an N electron, single-determinant wave function. It is constructed from the one-electron functions ψ_i called the spin orbitals which themselves can be decomposed into two parts: a spatial-part $\varphi_i \equiv \varphi_i(\vec{r}_i)$, that only depends on the coordinates $\vec{r}_i$ of the ith electron, and

a spin-part depending only on the spin σ_i of the ith electron. According to these spatial and spin-dependence of the spin-orbitals, a shorthand i may be used in the argument of the spin-orbitals. i in the argument denotes the compound formed from the spatial coordinates and the spin of the electrons, $i \equiv \{\vec{r}_i, \sigma_i\}$. The spin function mirrors the fact that the projection of the spin of an electron along an axis – commonly chosen to be the z axis – is either $\frac{1}{2}\hbar$ or $-\frac{1}{2}\hbar$ or, when working with atomic units, $\pm\frac{1}{2}$. The "up" and "down" spins are associated with the spin-functions $\alpha(\sigma)$ and $\beta(\sigma)$, respectively, where σ is a discrete variable with values $\pm\frac{1}{2}$. The spin-functions as a function of σ are then

$$\alpha(\sigma) = \delta_{\sigma,\frac{1}{2}} \tag{1.3.2}$$

and

$$\beta(\sigma) = \delta_{\sigma,-\frac{1}{2}}. \tag{1.3.3}$$

A general spin orbital can be built up as

$$\psi_i(i) \equiv \psi_i(\vec{r}_i, \sigma_i) = \varphi_{i,1}(\vec{r}_i)\alpha(\sigma_i) + \varphi_{i,2}(\vec{r}_i)\beta(\sigma_i), \tag{1.3.4}$$

where $\varphi_{i,1}$ and $\varphi_{i,2}$ are some spatial functions in the combinations. For simplicity's sake, however, one often uses spin-orbitals whose spin-part corresponds to pure "up" or "down" spins, so spin orbitals in the form

$$\psi_i(i) = \varphi_i(\vec{r}_i)\alpha(\sigma_i) \tag{1.3.5}$$

or

$$\psi_i(i) = \varphi_i(\vec{r}_i)\beta(\sigma_i) \tag{1.3.6}$$

are commonly used.

Utilising determinant wave functions in the form of eq. (1.3.1) is advantageous for multiple reason. The biggest advantage is that ψ being a determinant, it possesses every properties a determinant has. Changing any two rows of a determinant causes it to change its sign; in ψ this is equivalent to interchanging two electrons. The electrons being fermions, the anti-symmetry with respect to interchanging any two electrons i and j is expected from the wave function. Moreover, a determinant also changes sign upon swapping two of its columns. If ψ contains two identical columns, then the determinant ψ_S that has those two columns swapped must satisfy the requirement $\psi_S = -\psi = \psi$ which results in $\psi \equiv 0$. It is prohibited for the electrons to occupy the same spin-orbital; this is the consequence of the Pauli principle and the determinant wave functions automatically satisfy this requirement.

To get the HF working equations, a determinant wave function ψ is variationally optimised so that its energy E is stationary. For a wave function ψ this means the optimisation of the energy

$$E = \frac{\langle\psi|\hat{H}|\psi\rangle}{\langle\psi|\psi\rangle}. \tag{1.3.7}$$

Requiring the first variation δE of E to vanish results in the equation

$$\begin{aligned}\delta E = 0 = \delta\frac{\langle\psi|\hat{H}|\psi\rangle}{\langle\psi|\psi\rangle} &= \frac{\langle\delta\psi|\hat{H}|\psi\rangle\langle\psi|\psi\rangle + \langle\psi|\hat{H}|\delta\psi\rangle\langle\psi|\psi\rangle}{\langle\psi|\psi\rangle^2} \\ &- \frac{\langle\psi|\hat{H}|\psi\rangle\langle\delta\psi|\psi\rangle - \langle\psi|\hat{H}|\psi\rangle\langle\psi|\delta\psi\rangle}{\langle\psi|\psi\rangle^2} \\ &= \frac{\langle\delta\psi|\hat{H}|\psi\rangle\langle\psi|\psi\rangle - \langle\psi|\hat{H}|\psi\rangle\langle\delta\psi|\psi\rangle}{\langle\psi|\psi\rangle^2} + c.c.\end{aligned} \tag{1.3.8}$$

where *c.c.*, as usual, stands for the complex conjugate of every terms appearing on the right-hand side. Due to the variations $\delta\psi$ on the right hand side are arbitrary, the requirement can also be expressed in a more compact form

$$\langle\delta\psi|\hat{H} - E|\psi\rangle = 0. \tag{1.3.9}$$

Eq. (1.3.9) is the most useful formulation of the variational principle required for the energy of a wave function ψ to be stationary. Applying this to the single-determinant wave function in eq. (1.3.1) means varying the spin-orbitals ψ_i and substituting them with

$$\psi_i \to \psi_i + \delta\psi_i. \tag{1.3.10}$$

The variation $\delta\psi_i$ is arbitrary and can be written as the sum of two variations,

$$\delta\psi_i = \delta\psi_{i_\parallel} + \delta\psi_{i_\perp} = \eta\psi'_{i_\parallel} + \eta\psi'_{i_\perp}, \tag{1.3.11}$$

where η is an arbitrary complex parameter and the indices $\parallel$ and $\perp$ denote variations lying in the subspace of the spin-orbitals ψ_i and perpendicular to it, respectively. Putting this back into the determinant wave function ψ yields

$$\begin{aligned}\psi + \delta\psi &= \frac{1}{\sqrt{N!}}\begin{vmatrix} \psi_1(1)+\delta\psi_1(1) & \psi_2(1)+\delta\psi_2(1) & \cdots & \psi_N(1)+\delta\psi_N(1) \\ \psi_1(2)+\delta\psi_1(2) & \psi_2(2)+\delta\psi_2(2) & \cdots & \psi_N(2)+\delta\psi_N(2) \\ \vdots & \vdots & \ddots & \vdots \\ \psi_1(N)+\delta\psi_1(N) & \psi_2(N)+\delta\psi_2(N) & \cdots & \psi_N(N)+\delta\psi_N(N) \end{vmatrix} \\ &= \frac{1}{\sqrt{N!}}\sum_{P\in S_N}(-1)^p\prod_{i=1}^{N}(\psi_{P_i}(i)+\delta\psi_{P_i}(i)),\end{aligned} \tag{1.3.12}$$

where P is a permutation of parity p that reorders the N electrons $\{1, 2, \ldots, N\}$ and the sum is to be performed over all possible permutations, resulting in $N!$ terms. The set of all possible such permutations is denoted by S_N, the symmetric group of N elements. After performing a permutation P that reorders the elements in the set $\{1, 2, \ldots, N\}$, the ith element of the reordered set is P_i. Keeping only terms up to first order of the variations $\delta\psi_i$, the expansion can be written as

$$\psi + \delta\psi = \psi + \sum_{i=1}^{N} \psi^{(1)}(\psi_i \to \delta\psi_i) \tag{1.3.13}$$

and

$$\delta\psi = \sum_{i=1}^{N} \psi^{(1)}(\psi_i \to \delta\psi_i). \tag{1.3.14}$$

$\psi^{(1)}(\psi_i \to \delta\psi_i)$ is a determinant wave function much similar to eq. (1.3.1), but it has the spin-orbital ψ_i swapped for $\delta\psi_i$. The condition for the energy to be stationary is then

$$\begin{aligned}
&\langle\delta\psi|\hat{H} - E|\psi\rangle = \langle\sum_{i=1}^{N} \psi^{(1)}(\psi_i \to \delta\psi_i)|\hat{H} - E|\psi\rangle = \\
&= \langle\sum_{i=1}^{N} \psi^{(1)}(\psi_i \to \eta\psi_{i_\parallel})|\hat{H} - E|\psi\rangle + \langle\sum_{i=1}^{N} \psi^{(1)}(\psi_i \to \eta\psi_{i_\perp})|\hat{H} - E|\psi\rangle = \\
&= \eta^* \sum_{i=1}^{N} \langle\psi^{(1)}(\psi_i \to \psi_{i_\parallel})|\hat{H} - E|\psi\rangle + \eta^* \sum_{i=1}^{N} \langle\psi^{(1)}(\psi_i \to \psi_{i_\perp})|\hat{H} - E|\psi\rangle \,.
\end{aligned} \tag{1.3.15}$$

Since $\psi_{i_\parallel}$ lies in the subspace of the occupied orbitals ψ_i, used to build ψ up, $\psi_{i_\parallel}$ can be written as

$$\psi_{i_\parallel} = \sum_{n=1}^{N} c_{in}\psi_n = c_{ii}\psi_i + \sum_{\substack{n=1 \\ n\neq i}}^{N} c_{in}\psi_n. \tag{1.3.16}$$

Expanding the determinant $\psi^{(1)}(\psi_i \to \psi_{i_\parallel})$ then gives

$$\psi^{(1)}(\psi_i \to \psi_{i_\parallel}) = \psi^{(1)}(\psi_i \to c_{ii}\psi_i) + \psi^{(1)}(\psi_i \to \sum_{\substack{n=1 \\ n\neq i}}^{N} c_{in}\psi_n). \tag{1.3.17}$$

The last term in eq. (1.3.17) is a determinant whose ith column is expanded as a linear combination of all the other columns $j \neq i$, thus, yields 0. The determinant

$$\psi^{(1)}(\psi_i \to c_{ii}\psi_i) \tag{1.3.18}$$

only differs from ψ in its normalisation and it is proportional to ψ, $\psi^{(1)}(\psi_i \to c_{ii}\psi_i) = \alpha\psi$. Due to this, the variation of the energy corresponding to $\delta\psi_{i_\parallel}$ vanishes

$$\langle\psi^{(1)}(\psi_i \to c_{ii}\psi_i)|\hat{H} - E|\psi\rangle = \langle\alpha\psi|\hat{H} - E|\psi\rangle = 0. \tag{1.3.19}$$

The requirement for E to be stationary is therefore

$$\langle\delta\psi|\hat{H} - E|\psi\rangle = \eta^* \sum_{i=1}^{N} \langle\psi^{(1)}(\psi_i \to \psi_{i_\perp})|\hat{H} - E|\psi\rangle = 0. \tag{1.3.20}$$

In order for this requirement to be fulfilled, the contributions corresponding to each i must be equal to zero. Moreover, since η is an arbitrary small, but non-zero complex variational parameter, one may divide both sides by it and acquire the condition

$$\langle\delta\psi|\hat{H} - E|\psi\rangle = \langle\psi^{(1)}(\psi_i \to \psi_{i_\perp})|\hat{H} - E|\psi\rangle = 0. \tag{1.3.21}$$

At this point one can make use of Slater's rules for the overlap of two determinant wave functions that differ in a single spin orbital that is orthogonal to all other spin orbitals. Such an overlap is zero, therefore

$$\langle\psi^{(1)}(\psi_i \to \psi_{i_\perp})|\psi\rangle = 0 \tag{1.3.22}$$

with which the condition for $\delta E = 0$ gives

$$\langle\psi^{(1)}(\psi_i \to \psi_{i_\perp})|\hat{H}|\psi\rangle = 0. \tag{1.3.23}$$

The above equation is Brillouin's theorem for single determinant wave functions.

In the simplest cases, the Hamiltonian does not act on the spins of the electrons and can be written as the sum of one-electron Hamiltonians $\hat{h}_i$ acting on functions depending on the coordinates of the ith electron and the sum of two-electron Hamiltonians corresponding to the interaction between any pair of electrons (i, j). Then such an expansion yields

$$\hat{H} = \sum_{i=1}^{N} \hat{h}_i + \sum_{\substack{i,j=1 \\ j<i}}^{N} \hat{g}_{ij}. \tag{1.3.24}$$

A simple example for $\hat{h}_i$ can be formed from the Hamiltonian in eq. (1.1.1) by including the terms containing the kinetic energy of the ith electron and the interaction between it and the nuclei. On the other hand,

$\hat{g}_{ij}$ could be taken as the Coulomb interaction $\frac{1}{r_{ij}}$ of any two electrons. Putting the above in order provides

$$\begin{aligned}\langle\psi^{(1)}(\psi_i \to \psi_{i_\perp})|\hat{H}|\psi\rangle = \langle\psi^{(1)}(\psi_i \to \psi_{i_\perp})|\sum_{i=1}^{N}\hat{h}_i|\psi\rangle + \\ + \langle\psi^{(1)}(\psi_i \to \psi_{i_\perp})|\sum_{\substack{i,j=1\\ j>i}}^{N}\hat{g}_{ij}|\psi\rangle\,.\end{aligned} \tag{1.3.25}$$

The Slater-rules for matrix elements between determinant wave functions allow for evaluating eq. (1.3.25). With their aid one can write

$$\begin{aligned}\langle\psi^{(1)}(\psi_i \to \psi_{i_\perp})|\sum_{i=1}^{N}\hat{h}_i|\psi\rangle = \langle\psi_{i_\perp}|\hat{h}_i|\psi_i\rangle = \langle\varphi_{i_\perp}\gamma_{i_\perp}|\hat{h}_i|\varphi_i\gamma_i\rangle = \\ = \sum_{\sigma}\gamma^*_{i_\perp}(\sigma)\gamma_i(\sigma)\,\langle\varphi_{i_\perp}|\hat{h}_i|\varphi_i\rangle = \delta_{\gamma_{i_\perp}\gamma_i}\,\langle\varphi_{i_\perp}|\hat{h}_i|\varphi_i\rangle\,.\end{aligned} \tag{1.3.26}$$

The summation over σ assumes discrete values $\sigma = \pm\frac{1}{2}$ and due to the spin functions $\gamma^*_{i_\perp}$ and γ_i being orthonormal, this yields $\delta_{\gamma_{i_\perp}\gamma_i}$. Choosing the spin orbital $\gamma_{i_\perp}$ to have different spin-part than γ_i automatically satisfies eq. (1.3.26) for every i in the condition eq. (1.3.25). The same can be shown for the case of the two-electron part of the requirement. Due to this, it is sufficient to require the condition in eq. (1.3.25) to be fulfilled for those spin-orbitals only that have the same spin-part in $\psi_{i_\perp}$ and ψ_i. Thus one may restrict the problem to those variations for which

$$\psi_i = \varphi_i\gamma_i \to \psi_{i_\perp} = \varphi_{i_\perp}\gamma_i \tag{1.3.27}$$

holds and then prescribing

$$\langle\psi_{i_\perp}|\psi_j\rangle = 0 \tag{1.3.28}$$

for all spin-orbitals ψ_i and ψ_j that have the same spin as $\psi_{i_\perp}$. Doing so yields

$$\langle\psi^{(1)}(\varphi_i\gamma_i \to \varphi_{i_\perp}\gamma_i)|\sum_{i=1}^{N}\hat{h}_i|\psi\rangle = \langle\varphi_{i_\perp}|\hat{h}_i|\varphi_i\rangle \tag{1.3.29}$$

for the one-electron part of the requirement and

$$\langle\psi^{(1)}(\varphi_i\gamma_i \to \varphi_{i_\perp}\gamma_i)|\sum_{\substack{i,j=1\\ j>i}}^{N}\hat{g}_{ij}|\psi\rangle = \sum_{\substack{j=1\\ j\neq i}}^{N}\Big([\varphi_{i_\perp}\varphi_j|\varphi_i\varphi_j] - [\varphi_{i_\perp}\varphi_j|\varphi_j\varphi_i]\cdot\delta_{\gamma_i\gamma_j}\Big), \tag{1.3.30}$$

where $[\varphi_i\varphi_j|\varphi_k\varphi_l]$ denotes the two-electron integral

$$[\varphi_i\varphi_j|\varphi_k\varphi_l] = \int\int \frac{\varphi_i^*(\vec{r}_1)\varphi_j^*(\vec{r}_2)\varphi_k(\vec{r}_1)\varphi_l(\vec{r}_2)}{r_{12}} dV_1 dV_2, \tag{1.3.31}$$

$dV_i = dx_i dy_i dz_i$. Commonly eq. (1.3.30) is the introductory point to the Coulomb operator $\hat{J}_j$

$$\hat{J}_j\varphi(\vec{r}_1) = \int \frac{\varphi_j^*(\vec{r}_2)\varphi_j(\vec{r_2})}{r_{12}} dV_2 \varphi(\vec{r}_1) \tag{1.3.32}$$

and the exchange operator $\hat{K}_j$

$$\hat{K}_j\varphi(\vec{r}_1) = \int \frac{\varphi_j^*(\vec{r}_2)\varphi(\vec{r_2})}{r_{12}} dV_2 \varphi_j(\vec{r}_1). \tag{1.3.33}$$

With their definition the condition for stationary energy is commonly written as

$$\int \varphi_{i_\perp}^*(\vec{r}_1)\Big(\Big[\hat{h} + \sum_{\substack{j=1\\ j\neq i}}^{N}(\hat{J}_j - \hat{K}_j\delta_{\gamma_i\gamma_j})\Big]\varphi_i(\vec{r}_1)\Big) dV_1 = 0. \tag{1.3.34}$$

As Mayer points out in [20], the requirements of (1.3.34) being zero and $\varphi_{i_\perp}^*$ being orthogonal to every ψ_j in ψ that has the same spin as ψ_i can only be satisfied at the same time if $\Big[\hat{h} + \sum_{\substack{j=1\\ j\neq i}}^{N}(\hat{J}_j - \hat{K}_j\delta_{\gamma_i\gamma_j})\Big]\varphi_i$ does not have contribution from the subspace orthogonal to the space formed by the occupied orbitals $\{\psi_j\}$ that have the same spin as ψ_i. Otherwise, $\psi_{i_\perp}$ would not be orthogonal to it and eq. (1.3.34) would be non-zero.
Thus a more general form of the HF equations may be written as

$$\Big[\hat{h} + \sum_{\substack{j=1\\ j\neq i}}^{N}(\hat{J}_j - \hat{K}_j\delta_{\gamma_i\gamma_j})\Big]\varphi_i = \sum_{j=1}^{N}\alpha_{ji}\varphi_j\ \delta_{\gamma_i\gamma_j}. \tag{1.3.35}$$

Although eq. (1.3.35) can be referred to as the condition for the energy of the single-determinant ψ to be stationary, in most cases it is too general. In order to get working equations that are more fitting for practical use cases, one may introduce the spin orbitals

$$\chi_i(\vec{r},\sigma) = u_i(\vec{r})\alpha(\sigma) \quad i = 1, 2, \ldots, n_\chi \tag{1.3.36}$$

$$\kappa_i(\vec{r},\sigma) = v_i(\vec{r})\beta(\sigma) \quad i = 1, 2, \ldots, n_\kappa \tag{1.3.37}$$

and use them to build up the N-electron determinant wave function ψ, $N = n_\chi + n_\kappa$. In the most straightforward case, for N electrons of even number and $n_\chi = n_\kappa$, ψ is simply

$$\psi(1,2,\ldots,N) = \frac{1}{\sqrt{N!}} \begin{vmatrix} u_1(\vec{r}_1)\alpha(\sigma_1) & v_1(\vec{r}_1)\beta(\sigma_1) & \cdots & v_{n_\kappa}(\vec{r}_1)\beta(\sigma_1) \\ u_1(\vec{r}_2)\alpha(\sigma_2) & v_1(\vec{r}_2)\beta(\sigma_2) & \cdots & v_{n_\kappa}(\vec{r}_2)\beta(\sigma_2) \\ \vdots & \vdots & \ddots & \vdots \\ u_1(\vec{r}_N)\alpha(\sigma_N) & v_1(\vec{r}_N)\beta(\sigma_N) & \cdots & v_{n_\kappa}(\vec{r}_N)\beta(\sigma_N) \end{vmatrix}. \tag{1.3.38}$$

For the case of the spatial part of the spin-orbitals, one can introduce the Coulomb and exchange operators in a similar way to eq. (1.3.32) and eq. (1.3.33), but this time they are expressed in terms of the respective functions u_i or v_i:

$$\hat{J}_{u_j}\varphi(\vec{r}_1) = \int \frac{u_j^*(\vec{r}_2)u_j(\vec{r}_2)}{r_{12}} dV_2 \varphi(\vec{r}_1), \tag{1.3.39}$$

$$\hat{K}_{u_j}\varphi(\vec{r}_1) = \int \frac{u_j^*(\vec{r}_2)\varphi(\vec{r}_2)}{r_{12}} dV_2 u_j(\vec{r}_1), \tag{1.3.40}$$

with φ being an arbitrary spatial function. Swapping u_j with v_j in $\hat{J}_{u_j}$ and $\hat{K}_{u_j}$ gives the appropriate operators with respect to the spatial functions v_j. Choosing $\varphi_i = u_i$ in eq. (1.3.35), the working equations for the spatial-functions $\{u_j\}$ are given by

$$\begin{aligned} &\Big[\hat{h} + \sum_{\substack{j=1 \\ j\neq i}}^{n_\chi}(\hat{J}_{u_j} - \hat{K}_{u_j}\delta_{\gamma_i\gamma_j}) + \sum_{j=1}^{n_\kappa}(\hat{J}_{v_j} - \hat{K}_{v_j}\delta_{\gamma_i\gamma_j})\Big]u_i = \\ &= \Big[\hat{h} + \sum_{\substack{j=1 \\ j\neq i}}^{n_\chi}(\hat{J}_{u_j} - \hat{K}_{u_j}) + \sum_{j=1}^{n_\kappa}\hat{J}_{v_j}\Big]u_i = \sum_{j=1}^{n_\chi}\varepsilon_{ji}^{(u)}u_j, \end{aligned} \tag{1.3.41}$$

because in the first sum $\delta_{\gamma_i\gamma_j} = 1$ since every spin-orbitals χ_i have the same α spin, while in the second sum $\delta_{\gamma_i\gamma_j} = 0$ because the κ_i spin-orbitals possess β spin. Interchanging u_j with v_j and n_χ with n_κ in the above results yields the working equations for the spatial-functions $\{v_j\}$. Due to the restriction $j \neq i$ in the first sum of eq. (1.3.41), the working equations assume slightly different form for every function u_i. This might be lifted by noting $(\hat{J}_{u_i} - \hat{K}_{u_j})u_i = 0$, thus allowing $j = i$ does not contribute to the expression in the bracket. The operator in the left hand side of eq. (1.3.41) is the Fockian; for the set of functions $\{u_j\}$

$$\hat{F}^{(u)} = \Big[\hat{h} + \sum_{j=1}^{n_\chi}(\hat{J}_{u_j} - \hat{K}_{u_j}) + \sum_{j=1}^{n_\kappa}\hat{J}_{v_j}\Big] \tag{1.3.42}$$

and it permits writing eq. (1.3.41) in the compact forms

$$\hat{F}^{(u)}u_i = \sum_{j=1}^{n_\chi} \varepsilon_{ji}^{(u)} u_j \tag{1.3.43}$$

$$\hat{F}^{(v)}v_i = \sum_{j=1}^{n_\kappa} \varepsilon_{ji}^{(v)} v_j. \tag{1.3.44}$$

The Fockians depend on the orbitals u_i and v_j and solving either eq. (1.3.43) or eq. (1.3.44) would require one to already know the solutions to the orbitals which should be otherwise determined by the very same equations. In order to get going, initial guesses $\{u_i^{(0)}\}$ and $\{v_j^{(0)}\}$ are input to a procedure whose first step is to calculate the Fockians and solve the equations (1.3.43)–(1.3.44) for a new set of functions $\{u_i^{(1)}\}$ and $\{v_j^{(1)}\}$. From these, the Fockians are re-calculated and the same steps get repeated until a convergence criteria is fulfilled, for example, when solving for a new set of functions with the new Fockians reproduces the same functions that were acquired in the previous step. These solutions are called the self-consistent field (SCF) solutions of the problem.

The HF method that was discussed here is called the Unrestricted Hartree-Fock (UHF) method, because no restrictions were imposed on electrons so that two electrons occupy the same spatial-orbital with different spins. When the requirement of double-occupancy is set, the corresponding HF method is called the Restricted Hartree-Fock (RHF) method. The RHF equations are a special case of the UHF ones; they can be derived by substituting the relevant quantities ($u_i, v_j, \varepsilon_{ji}^{(v)}$ and so on) for expressions obeying the restriction imposed by the double-occupancy.

Although the working equations of the RHF or UHF cases augmented with iterative approach give the recipe for finding the orbitals, in most practical use cases they are too complex to solve, almost impossible for even smaller molecules of quantum-chemical interest. For molecular systems, a common approach is to express the spatial-orbitals φ_i as a linear combinations of some basis functions. These functions oftentimes result from HF calculations done for free atoms and are called atomic orbitals (AO). Expanding φ_i in terms of a finite number of atomic orbitals serving as basis functions is thus called the linear combination of atomic orbitals, LCAO method. The resulting equations are the Hartee-Fock-Roothan (HFR) equations.
Nowadays, vast amount of basis functions are routinely used to describe

complex molecular systems. There also exist databases [21] that compile large number of basis functions, freely available.

1.3.2 Electron correlation methods

In order for theoretical quantum chemistry calculations to be of reliable precision that may lead to application in experiments or other practical uses, a more rigorous approach to the correct treatment of electron correlation is needed. Treating the interaction between the electrons in an averaged way like the HF method does leads to errors in electronic structure data that do not allow for accurate description of molecular processes.
Modern quantum chemistry depends greatly on using basis functions and making use of the HFR approach in which the spatial part of the spin-orbitals ψ_i, that build up the Slater-determinant, are expressed as a linear combination of said functions in the basis set. The simplest set is the minimal one; only one function is used per orbital – e.g. one for each of the orbitals $1s, 2s, 2p \ldots$ – that describe the electronic structure of the system. Assigning more basis functions to every orbital yield better results. In the Double-Zeta (DZ) and Triple-Zeta (TZ) sets there are two and three basis functions per orbitals, respectively. On the other hand, with a basis set called STO-NG, Slater-type orbitals [22] (STO) are expressed as a linear combination of n Gaussian-type orbitals [23] (GTO) and many more basis sets are widely used.

Expressing the spatial part of the spin orbitals ψ_i in a basis that consists of n functions yields n spatial-functions and $2n$ different spin-orbitals – corresponding to the different spins α and β – that can build the Slater-determinant up. For an N electron wave function a total of $\binom{2n}{N}$ possible Slater-determinants may be created and that one which possesses the lowest energy after the variational optimisation of the combinational coefficients is the ground-state ψ provided by the HFR method. The remaining $2n - N$ spin-orbitals that are left unused when ψ is built are called virtual orbitals. Any determinant-wave function other than ψ can be characterised with respect to the occupied spin-orbitals that are swapped with functions from the set of the virtual orbitals. In the case of a singly-excited determinant $\psi^{(1)}_{i\to a}$, one electron from the ith occupied spin orbital ψ_i of the ground-state ψ is admitted to the virtual orbital ϕ_a,

$$\psi^{(1)}_{i\to a} = \psi(\psi_i \to \phi_a); \quad i = 1, 2, \ldots, N, \quad a = 1, 2, \ldots, 2n - N. \quad (1.3.45)$$

Similarly, all possible double excitations may be given by

$$\psi^{(2)}_{\substack{i\to a \\ j\to b}} = \psi(\{\psi_i, \psi_j\} \to \{\phi_a, \phi_b\}); \quad i \neq j, \quad a \neq b. \quad (1.3.46)$$

The different $\psi^{(k)}$ k-times excited determinants are called Configuration State Functions (CSF). These are constructed so as to be an eigenstate of the operators commuting with the Hamiltonian of the system and they are characterised by the same quantum numbers as the wave function of the system. In Configuration Interaction (CI) methods the wave function Ψ is formed by a linear combination of independent CSF functions in the form of equations (1.3.45) – (1.3.46) and determinant wave functions corresponding to higher excitations are considered as well,

$$\Psi = \psi + \sum_{i=1}^{N} \sum_{a=1}^{2n-N} \alpha_{i,a} \psi_{i \to a}^{(1)} + \sum_{\substack{i,j=1 \\ i<j}}^{N} \sum_{\substack{a,b=1 \\ a<b}}^{2n-N} \alpha_{ij,ab} \psi_{\substack{i \to a \\ j \to b}}^{(2)} + \dots \tag{1.3.47}$$

It is important to note that in the CI scheme of eq. (1.3.47) only the independent CSFs are to be taken into account, hence the restriction to the indices $i < j$ and $a < b$ of the summations over the doubly-excited determinants is employed. Otherwise, such CSFs that only differ by swapping i and j or a and b would also be included. However, these are not unique since

$$\psi_{\substack{i \to a \\ j \to b}}^{(2)} = -\psi_{\substack{j \to a \\ i \to b}}^{(2)} \tag{1.3.48}$$

applies due to the properties of the determinants. Calculations that include all possible CSFs in the combination eq. (1.3.47) that can be built from the n basis functions is called Full CI (FCI).

Any state Ψ can be expanded according to eq. (1.3.47), but such an expression is too demanding to handle computationally, if not outright impossible. To alleviate the problems stemming from computational difficulties, only a finite number of $N \times N$ determinants Φ are considered. In practice linear combinations such as

$$\Psi = \psi + \sum_{m=1}^{M} \beta_m \Phi_m \tag{1.3.49}$$

are constructed. Here Φ_m can be either a singly, doubly or even higher excited Slater-determinant, but compared to eq. (1.3.47), only a number M of excited determinants are selected. Following the standard procedure of variational optimisation, the optimal coefficients β_i, so that $\delta E = \langle \delta\Psi | \hat{H} - E | \Psi \rangle = 0$ is satisfied, can be found. Assuming this to be done and β_m in eq. (1.3.49) to be the optimal ones, then multiplying the stationary Schrödinger equation $\hat{H}\Psi = E\Psi$ by ψ^* and integrating over

all space gives

$$\langle\psi|\hat{H}|\Psi\rangle = E\,\langle\psi|\Psi\rangle = \\ = \langle\psi|\hat{H}|\psi\rangle + \sum_{m=1}^{M}\beta_m\,\langle\psi|\hat{H}|\Phi_m\rangle = E\,\langle\psi|\psi\rangle + E\sum_{m=1}^{M}\beta_m\,\langle\psi|\Phi_m\rangle\,. \tag{1.3.50}$$

With $\langle\psi|\psi\rangle = 1$ and $\langle\psi|\Phi_m\rangle = 0$ eq. (1.3.50) yields

$$E = \langle\psi|\hat{H}|\psi\rangle + \sum_{me=1}^{M}\beta_m\,\langle\psi|\hat{H}|\Phi_m\rangle = E_{HF} + \sum_{m=1}^{M}\beta_m H_{HF,m} \tag{1.3.51}$$

and E_{HF} is the energy of the optimised Slater-determinant in the HF method and $H_{HF,m}$ is the matrix element of $\hat{H}$ between the HF wave function ψ and the excited determinants Φ_m of the CI expansion. The difference of the energies E and E_{HF} is called the correlation energy

$$E_{corr} = E - E_{HF} = \sum_{m=1}^{M}\beta_m H_{HF,m}, \tag{1.3.52}$$

that accounts for the fact that the electrons do not move independently from all other electrons but correlated; it is characteristic to the error introduced by the HF method by handling the problem in an averaged way. A first approach to simplify eq. (1.3.52) is by selecting those matrix elements $H_{HF,m}$ that do not vanish. For a spin-free Hamiltonian, the one-electron part $\hat{h}_i$ has zero matrix element between ψ and any determinant Φ_m that is doubly or higher excited. On the other hand, the two electron operator $\hat{g}_{ij}$ has zero matrix elements if Φ_m is triply excited. In addition, none of the singly excited determinants contribute to eq. (1.3.52) according to Brillouin's theorem. As a consequence, to calculate E_{corr}, one may start out with including only the doubly excited determinants Φ_m into the CI expansion. This is called the Double CI (DCI) variant of the CI method.

In SDCI calculations not only doubly excited determinants, but singly excited ones are included as well, despite Brillouin's theorem allowing for their exclusion. This is done because by including singly excitations into the expansion eq. (1.3.49) and then performing the variational optimisation to get the coefficients β_i, matrix elements between singly and doubly excited determinants are non-zero. This results in a slightly differing combination of doubly excited determinants and also different matrix elements $H_{HF,m}$ in eq. (1.3.52) between ψ and the doubly excited determinants. For this reason, single excitations can alter the correlation

energy and are almost always included in CI calculations. The possible number of such determinants is also much smaller than that of higher excitations, therefore, they do not amount to much more demanding calculations.

1.3.3 Multi-configuration and multi-reference methods

In order to get better results in a CI calculation one has to include more and more determinants Φ_m in eq. (1.3.49). These determinants are excited compared to the reference determinant and this latter one is built up from fixed spin-orbitals that were acquired in previous calculations as a linear combination of some basis functions (HFR method). Since the reference Slater-determinant is built up from these spin-orbitals, one may get better results if not only the CI expansion coefficients, but the combination coefficients of the spin-orbitals are optimised as well. Multi-configuration self-consistent field (MCSCF) calculations do exactly this; they optimise the two sets of coefficients simultaneously. For most applications of chemical interest, MC methods allow for the same quality of description with the inclusion of fewer CSF for the price of additional computational demand due to the optimisation of another set of coefficients.

Particularly important version of MCSCF is the Complete Active Space (CASSCF) method [24]. In CASSCF, the spin-orbitals get divided into different groups according to how they appear in the SCFs included in the CI expansion. Orbitals appearing as doubly filled orbitals in all the SCFs are called closed/frozen/inactive orbitals. On the other hand, orbitals always unoccupied constitute the virtual orbitals and orbitals corresponding to energies between the set of closed and virtual orbitals are the active orbitals. Considering a system with n active electrons, several different distributions of them over the active orbitals are possible. In CASSCF calculations all the possible distributions are taken into account, thus choosing the active space appropriately is the most important step of CASSCF. For calculations of excited electronic states, the expansion coefficients are optimised in such a way so that the weighted average of the energy of the electronic states is minimal (state-averaged CASSCF).

In CI calculations the reference Slater-determinant, from which excited configurations are generated, is kept fixed, the HF wave function often serving the reference state. Multi-Reference CI (MRCI) calculations lift this limitation and introduce several references instead of just using only one. As to what states should be included as additional references, a sensible choice can be made based upon performing preceding MCSCF (CASSCF) calculations by including those CSFs as references that had CI expansion coefficients in eq. (1.3.49) exceeding a certain value. Having selected the reference states one can proceed by constructing excited

determinants with respect to each of the references; in most applications quadruply or even higher excited determinants appear due to admitting excited SCFs to the reference set.

1.4 Nuclear dynamics propagation

In order to follow the time-evolution of the nuclei in any molecular dynamical simulation, the most challenging task is, once again, the adequate description of larger systems, where the dynamics involve many degrees of freedom. The simplest implementation of such simulations employ the time-dependent Hartree (TDH) method, first derived by Frenkel for electrons [25]. In this framework, every degree of freedom is characterised by a function, called single-particle function (SPF), and the wave function is approximated as the Hartree-product of the SPFs multiplied by an additional time-dependent coefficient. The TDH method, although being computationally the easiest and most affordable to implement, is a rather crude approximation, often not precise enough for most calculations of interest in physical chemistry.

At the other end of the spectrum there is the standard method, where the wave function is expanded in a basis formed by products of time-independent functions $\{\chi_j^{(\kappa)}\}$, with $\chi_j^{(\kappa)}$ being the jth function assigned to the description of the κth degree of freedom of the system and the expansion coefficients are taken to be time-dependent. Usually, both the number of functions included per degree of freedom to build the product basis set and the number of degrees of freedom present are significantly larger than one, thus the computational demands rise exponentially with the degrees of freedom, making the standard method suitable for rather small systems only.

As in general the standard method is inefficient for larger systems, an improvement of the TDH method is sought by taking more configurations into account and making use of more SPFs rather than just one for each degree of freedom. This modification leads to the multi-configuration methods, from which I discuss the MCTDH variant below.

1.4.1 Multi-configuration time-dependent Hartree method

A popular choice to conduct molecular dynamics simulations and track the evolution of the nuclei is the Multi-configuration time-dependent Hartree (MCTDH) method. Developed at the Institute of Physical Chemistry of University of Heidelberg since the 90s, a robust molecular dynamics package formed. The method is widely used in applications to scattering processes [26–28], photodissociation reactions [29–31] or calculations of absorption spectra [32, 33]. The method is very efficient for relatively small systems, containing up to 20-25 degrees of freedom [34, 35].

In this section the basic considerations, ultimately leading to the applied working equations of the MCTDH scheme are derived. Several publications have been written dealing with the theory of MCTDH [36–38]. The derivation here follows the review of the method published in [38] at the most crucial points, but it is augmented with several intermediate steps leading to the final forms of the equations.

The MCTDH trial wave function Ψ for a system with s degrees of freedom is constructed as a linear combination of s-dimensional Hartree-products,

$$\Psi(Q_1, Q_2, \ldots, Q_s, t) = \sum_{j_1=1}^{n_{Q_1}} \cdots \sum_{j_s=1}^{n_{Q_s}} A_{j_1 j_2 \ldots j_s}(t) \prod_{\kappa=1}^{s} \varphi_{j_\kappa}^{(\kappa)}(Q_\kappa, t), \qquad (1.4.1)$$

combining $N = \prod_{i=1}^{s} n_{Q_i}$ of such s-dimensional functions in total. The functions $\varphi_{j_\kappa}^{(\kappa)}$ building up the Hartree-products are called the single-particle functions (SPF). They are constructed as a combination of some functions as well; the latter called primitive basis functions (PBF) χ and they are independent of time:

$$\varphi_{j_\kappa}^{(\kappa)}(Q_\kappa, t) = \sum_{i_\kappa=1}^{N_\kappa} c_{j_\kappa, i_\kappa}^{(\kappa)}(t) \chi_{i_\kappa}^{(\kappa)}(Q_\kappa). \qquad (1.4.2)$$

Moreover, the SPFs are required to satisfy the following constraints:

$$\langle \varphi_i^{(\kappa)}(t=0) | \varphi_j^{(\kappa)}(t=0) \rangle = \delta_{ij}, \qquad (1.4.3)$$

$$\langle \varphi_i^{(\kappa)}(t) | \dot{\varphi}_j^{(\kappa)}(t) \rangle = -i \, \langle \varphi_i^{(\kappa)}(t) | g^{(\kappa)} | \varphi_j^{(\kappa)}(t) \rangle \, . \qquad (1.4.4)$$

$g^{(\kappa)}$ is a Hermitian operator that acts on the κth degree of freedom, its name is the constraint operator. $g^{(\kappa)}$ may be arbitrarily chosen and their explicit form do not make the precision of the MCTDH-scheme better or worse. However, a beneficial choice of constraints that exploit some underlying properties of the system may significantly reduce the computational work needed. For some examples of possible choices and their implications I refer to [38].

At this point the task is to determine the equations of motion that describe how the coefficients and the SPFs evolve. This is done by varying Ψ with respect to the single particle functions $\varphi_{j_\kappa}^{(\kappa)}$ and the expansion coefficients $A_{j_1 j_2 \ldots j_s}$.

Applying the variations $A_{j_1\ldots j_s} \to A_{j_1\ldots j_s} + \delta A_{j_1\ldots j_s}$ and $\varphi^{(\kappa)}_{j_\kappa} \to \varphi^{(\kappa)}_{j_\kappa} + \delta\varphi^{(\kappa)}_{j_\kappa}$ yields the varied wave function Ψ'

$$\begin{aligned}\Psi' &= \sum_{j_1}\ldots\sum_{j_s}(A_{j_1\ldots j_s} + \delta A_{j_1\ldots j_s})(\varphi^{(1)}_{j_1} + \delta\varphi^{(1)}_{j_1})\cdot\ \ldots\ \cdot(\varphi^{(s)}_{j_s} + \delta\varphi^{(s)}_{j_s}) = \\ &= \sum_{j_1}\ldots\sum_{j_s} A_{j_1\ldots j_s}\cdot(\varphi^{(1)}_{j_1} + \delta\varphi^{(1)}_{j_1})\cdot\ \ldots\ \cdot(\varphi^{(s)}_{j_s} + \delta\varphi^{(s)}_{j_s}) = \\ &+ \sum_{j_1}\ldots\sum_{j_s}\delta A_{j_1\ldots j_s}\cdot(\varphi^{(1)}_{j_1} + \delta\varphi^{(1)}_{j_1})\cdot\ \ldots\ \cdot(\varphi^{(s)}_{j_s} + \delta\varphi^{(s)}_{j_s}).\end{aligned} \tag{1.4.5}$$

Keeping only those terms in eq. (1.4.5) that contain only up to first order variations results in

$$\begin{aligned}\Psi' &= \sum_{j_1}\cdots\sum_{j_s} A_{j_1\ldots j_s}\prod_\kappa \varphi^{(\kappa)}_{j_\kappa} + \sum_{j_1}\cdots\sum_{j_s} A_{j_1\ldots j_s}\sum_\kappa \delta\varphi^{(\kappa)}_{j_\kappa}\prod_{\kappa'\neq\kappa}\varphi^{(\kappa')}_{j_{\kappa'}} + \\ &+ \sum_{j_1}\cdots\sum_{j_s}\delta A_{j_1\ldots j_s}\prod_\kappa\varphi^{(\kappa)}_{j_\kappa} = \\ &= \Psi + \sum_{j_1}\cdots\sum_{j_s} A_{j_1\ldots j_s}\sum_\kappa\delta\varphi^{(\kappa)}_{j_\kappa}\prod_{\kappa'\neq\kappa}\varphi^{(\kappa')}_{j_{\kappa'}} + \sum_{j_1}\cdots\sum_{j_s}\delta A_{j_1\ldots j_s}\prod_\kappa\varphi^{(\kappa)}_{j_\kappa}.\end{aligned} \tag{1.4.6}$$

The variation $\delta\Psi$ is then

$$\delta\Psi = \Psi' - \Psi = \sum_{j_1}\cdots\sum_{j_s} A_{j_1\ldots j_s}\sum_\kappa\delta\varphi^{(\kappa)}_{j_\kappa}\prod_{\kappa'\neq\kappa}\varphi^{(\kappa')}_{j_{\kappa'}} + \sum_{j_1}\cdots\sum_{j_s}\delta A_{j_1\ldots j_s}\prod_\kappa\varphi^{(\kappa)}_{j_\kappa}. \tag{1.4.7}$$

From eq. (1.4.7) results for $\delta\Psi/\delta A_{j_1\ldots j_s}$ and $\delta\Psi/\delta\varphi^{(\kappa)}_{j_\kappa} = \delta\Psi/\delta\varphi^{(\kappa)}_u$ ($u = 1, 2, \ldots, n_{Q_\kappa}$) can be read off as

$$\frac{\delta\Psi}{\delta A}_{j_1\ldots j_s} = \prod_\kappa \varphi^{(\kappa)}_{j_\kappa} \tag{1.4.8}$$

and

$$\frac{\delta\Psi}{\delta\varphi^{(\kappa)}_u} = \sum_{j_1}\cdots\sum_{j_{\kappa-1}}\sum_{j_{\kappa+1}}\cdots\sum_{j_s} A_{j_1\ldots j_{\kappa-1}uj_{\kappa+1}\ldots j_s}\prod_{\kappa'\neq\kappa}\varphi^{(\kappa')}_{j_{\kappa'}}. \tag{1.4.9}$$

The right hand side of eq. (1.4.9) is also called single-hole function $\Psi^{(\kappa)}_u$; the linear combination of all single-particle functions but those corresponding to the κth degree of freedom.

For $\dot{\Psi}$ one gets

$$\begin{aligned}\dot{\Psi} &= \sum_{j_1}\dots\sum_{j_s}\dot{A}_{j_1\dots j_s}\prod_{\kappa}\varphi^{(\kappa)}_{j_\kappa} + \sum_{j_1}\dots\sum_{j_s}A_{j_1\dots j_s}\dot{\varphi}^{(1)}_{j_1}\varphi^{(2)}_{j_2}\cdot\ldots\cdot\varphi^{(s)}_{j_s}+\dots \\ &\dots+\sum_{j_1}\dots\sum_{j_s}A_{j_1\dots j_s}\dot{\varphi}^{(s)}_{j_s}\varphi^{(1)}_{j_2}\cdot\ldots\cdot\varphi^{(s-1)}_{j_{s-1}} = \\ &= \sum_{j_1}\dots\sum_{j_s}\dot{A}_{j_1\dots j_s}\prod_{\kappa}\varphi^{(\kappa)}_{j_\kappa} + \sum_{\kappa}\sum_{j_1}\dots\sum_{j_s}A_{j_1\dots j_s}\dot{\varphi}^{(\kappa)}_{j_\kappa}\prod_{\kappa'\neq\kappa}\varphi^{(\kappa')}_{j_{\kappa'}}.\end{aligned} \tag{1.4.10}$$

By rewriting the index j_κ as u and then utilising the form of the single-hole function $\Psi^{(\kappa)}_u$ from eq. (1.4.9), eq. (1.4.10) may also be written more compactly as

$$\dot{\Psi} = \sum_{j_1}\dots\sum_{j_s}\dot{A}_{j_1\dots j_s}\prod_{\kappa}\varphi^{(\kappa)}_{j_\kappa} + \sum_{\kappa=1}^{s}\sum_{u=1}^{n_\kappa}\dot{\varphi}^{(\kappa)}_u\Psi^{(\kappa)}_u. \tag{1.4.11}$$

The coefficients $A_{j_1\dots j_s}$ and SPFs can be obtained by employing the Dirac-Frenkel variational principle [25, 39]

$$\langle\delta\Psi|\hat{H}\Psi - i\dot{\Psi}\rangle = 0. \tag{1.4.12}$$

$\delta\Psi$ is given by eq. (1.4.7) and it is the sum of $\delta\Psi_\varphi$ and $\delta\Psi_A$, the variations with respect to the coefficients and SPFs, respectively. Expanding $\delta\Psi$ accordingly yields

$$\langle\delta\Psi|\hat{H}\Psi - i\dot{\Psi}\rangle = \langle\delta\Psi_A|\hat{H}\Psi - i\dot{\Psi}\rangle + \langle\delta\Psi_\varphi|\hat{H}\Psi - i\dot{\Psi}\rangle = 0. \tag{1.4.13}$$

Since both $\delta A_{j_1\dots j_s}$ and $\delta\varphi^{(\kappa)}_{j_k}$ are arbitrary, their contributions to the right-hand side of eq. (1.4.13) need to vanish. As a consequence, all terms in $\delta\Psi_A$ contributing to eq. (1.4.13) shall vanish:

$$\begin{aligned}\langle\delta\Psi_A|\hat{H}\Psi - i\dot{\Psi}\rangle &= \langle\sum_{j_1}\dots\sum_{j_s}\delta A_{j_1\dots j_s}\prod_{\kappa}\varphi^{(\kappa)}_{j_\kappa}|\hat{H}\Psi - i\dot{\Psi}\rangle = \\ &= \sum_{j_1}\dots\sum_{j_s}\langle\delta A_{j_1\dots j_s}\prod_{\kappa}\varphi^{(\kappa)}_{j_\kappa}|\hat{H}\Psi - i\dot{\Psi}\rangle \\ &\Rightarrow \langle\delta A_J\Phi_J|\hat{H}\Psi - i\dot{\Psi}\rangle = 0,\end{aligned} \tag{1.4.14}$$

where J denotes an arbitrary, but fixed element from the set of all possible configurations $\{j_1\dots j_s\}$ and Φ_J is the product of SPFs with the indices $j_1\dots j_\kappa$ representing the same configuration J. Due to δA_J being an arbitrary variation, the above leads to

$$\langle\Phi_J|\hat{H}\Psi - i\dot{\Psi}\rangle = \langle\Phi_J|\hat{H}\Psi\rangle - i\,\langle\Phi_J|\dot{\Psi}\rangle = 0. \tag{1.4.15}$$

Upon substituting the expression of $\dot{\Psi}$ from eq. (1.4.11) one gets

$$\langle \Phi_J | \hat{H} \Psi \rangle = i \sum_{j_1} \dots \sum_{j_s} \langle \Phi_J | \dot{A}_{j_1 \dots j_s} \prod_{\kappa} \varphi_{j_\kappa}^{(\kappa)} \rangle + i \sum_{\kappa} \sum_{u=1}^{n_\kappa} \langle \Phi_J | \dot{\varphi}_u^{(\kappa)} \Psi_u^{(\kappa)} \rangle \,. \tag{1.4.16}$$

The first term can be split into two parts: one part is when the summation over the indices $j_1 \dots j_s$ reproduces the configuration J, and the other one where the summation takes over such configuration L that differ from the J one,

$$i \sum_{j_1} \dots \sum_{j_s} \langle \Phi_J | \dot{A}_{j_1 \dots j_s} \prod_{\kappa} \varphi_{j_\kappa}^{(\kappa)} \rangle = i \dot{A}_J + i \sum_{\substack{L \\ L \neq J}} \langle \Phi_J | \dot{A}_L \Phi_L \rangle = i \dot{A}_J, \tag{1.4.17}$$

because according to the constraints of the SPFs, the overlap $\langle \Phi_J | \dot{A}_L \Phi_L \rangle$ vanishes between different configurations. Turning to the second term on the right-hand side of eq. (1.4.16),

$$\begin{aligned} & i \sum_{\kappa} \sum_{u=1}^{n_{Q_\kappa}} \langle \Phi_J | \dot{\varphi}_u^{(\kappa)} \Psi_u^{(\kappa)} \rangle = \\ & = i \sum_{\kappa} \sum_{u=1}^{n_{Q_\kappa}} \sum_{j_1} \dots \sum_{j_{\kappa-1}} \sum_{j_{\kappa+1}} \dots \sum_{j_s} A_{j_1 \dots j_{\kappa-1} u j_{\kappa+1} \dots j_s} \langle \Phi_J | \dot{\varphi}_u^{(\kappa)} \prod_{\kappa' \neq \kappa} \varphi_{j_{\kappa'}}^{(\kappa')} \rangle = \\ & = i \sum_{\kappa} \sum_{u=1}^{n_{Q_\kappa}} A_{J|\kappa \to u} \langle \varphi_{u_\kappa}^{(\kappa)} | \dot{\varphi}_u^{(\kappa)} \rangle \,, \end{aligned} \tag{1.4.18}$$

owing to the orthogonality-condition of the SPFs. The shorthand $A_{J|\kappa \to u}$ denotes a coefficient that corresponds to the configuration obtained by swapping the κth index in configuration J for u and u_κ is the κth index in J. $\langle \varphi_{u_\kappa}^{(\kappa)} | \dot{\varphi}_u^{(\kappa)} \rangle$ can be expressed in terms of the second constraint with which

$$i \sum_{\kappa} \sum_{u=1}^{n_{Q_\kappa}} A_{J|\kappa \to u} (-i) \langle \varphi_{u_\kappa}^{(\kappa)} | g^{(\kappa)} | \varphi_u^{(\kappa)} \rangle = \sum_{\kappa} \sum_{u=1}^{n_{Q_\kappa}} A_{J|\kappa \to u} g_{u_\kappa u}^{(\kappa)}, \tag{1.4.19}$$

with $g_{u_\kappa u}^{(\kappa)} = \langle \varphi_{u_\kappa}^{(\kappa)} | g^{(\kappa)} | \varphi_u^{(\kappa)} \rangle$.

Combining the preceding results plus expanding Ψ as $\sum_I A_I \Phi_I$, I denoting all possible $\{j_1 \dots j_s\}$ that can be formed, gives

$$i \dot{A}_J = \sum_I \langle \Phi_J | \hat{H} | \Phi_I \rangle \, A_I - \sum_{\kappa=1}^{s} \sum_{u=1}^{n_{Q_\kappa}} g_{u_\kappa u}^{(\kappa)} A_{J|\kappa \to u}, \tag{1.4.20}$$

the equation of motion for A_J in the MCTDH scheme.

Following the same steps, this time for the $\delta\varphi_{j_\kappa}^{(\kappa)}$ variations of the SPFs gives the equation

$$\langle\Psi_u^{(\kappa)}|\hat{H}|\Psi\rangle = i\,\langle\Psi_u^{(\kappa)}|\dot{\Psi}\rangle = i\,\langle\Psi_u^{(\kappa)}|\sum_N \dot{A}_N\Phi_N\rangle + i\,\langle\Psi_u^{(\kappa)}|\sum_{\nu=1}^{s}\sum_{m=1}^{n_{Q_\nu}}\dot{\varphi}_m^{(\nu)}\Psi_m^{(\nu)}\rangle\,, \tag{1.4.21}$$

with N denoting all possible configurations $\{n_1\dots n_s\}$. The first term on the right of eq. (1.4.21) can be written as

$$\sum_N \langle\Psi_u^{(\kappa)}|\Phi_N\rangle\, i\dot{A}_N = \sum_N \langle\Psi_u^{(\kappa)}|\Phi_N\rangle\,\langle\Phi_N|\hat{H}|\Psi\rangle - \sum_{\nu=1}^{s}\sum_{i=1}^{n_{Q_\nu}}\sum_N \langle\Psi_u^{(\kappa)}|\Phi_N\rangle\, g_{n_\nu i}^{(\nu)} A_{N_{|_{\nu\to i}}} \tag{1.4.22}$$

where the expression for $i\dot{A}_N$ is substituted from eq. (1.4.20). For the sum over ν, when $\nu=\kappa$ we get

$$\nu=\kappa: \qquad \sum_{i=1}^{n_{Q_\kappa}}\sum_N \langle\Psi_u^{(\kappa)}|\Phi_N\rangle\, g_{n_\kappa i}^{(\kappa)} A_{N_{|_{\kappa\to i}}}. \tag{1.4.23}$$

The overlap between $\Psi_u^{(\kappa)}$ and Φ_N vanishes due to the constraints the SPFs need to satisfy whenever the configuration N does not constitute the same single-hole configuration as $\Psi_u^{(\kappa)}$ defined in eq. (1.4.9). Then

$$\begin{aligned}\nu=\kappa: \qquad & \sum_{i=1}^{n_{Q_\kappa}}\sum_N \langle\Psi_u^{(\kappa)}|\Phi_N\rangle\, g_{n_\kappa i}^{(\kappa)} A_{N_{|_{\kappa\to i}}} = \\ & = \sum_{i,n_\kappa}^{n_{Q_\kappa}}\sum_{j_1=1}^{n_{Q_1}}\cdots\sum_{j_{\kappa-1}}^{n_{Q_{\kappa-1}}}\sum_{j_{\kappa+1}}^{n_{Q_{\kappa+1}}}\cdots\sum_{j_s}^{n_{Q_s}} A^*_{j_1\dots j_{\kappa-1}uj_{\kappa+1}\dots j_s}\times \\ & \times A_{j_1\dots j_{\kappa-1}ij_{\kappa+1}\dots j_s} g_{n_\kappa i}^{(\kappa)}\varphi_{n_\kappa}^{(\kappa)} = \sum_{i,n_\kappa}^{n_{Q_\kappa}} \rho_{ui}^{(\kappa)} g_{n_\kappa i}^{(\kappa)}\varphi_{n_\kappa}^{(\kappa)}.\end{aligned} \tag{1.4.24}$$

Here the definition of the single-hole density matrices was introduced by

$$\rho_{ui}^{(\kappa)} = \sum_{j_1=1}^{n_{Q_1}}\cdots\sum_{j_{\kappa-1}}^{n_{Q_{\kappa-1}}}\sum_{j_{\kappa+1}}^{n_{Q_{\kappa+1}}}\cdots\sum_{j_s}^{n_{Q_s}} A^*_{j_1\dots j_{\kappa-1}uj_{\kappa+1}\dots j_s} A_{j_1\dots j_{\kappa-1}ij_{\kappa+1}\dots j_s}. \tag{1.4.25}$$

With this we have

$$\begin{aligned}\sum_N \langle\Psi_u^{(\kappa)}|\Phi_N\rangle\, i\dot{A}_N &= \sum_N \langle\Psi_u^{(\kappa)}|\Phi_N\rangle\,\langle\Phi_N|\hat{H}|\Psi\rangle - \sum_{i,n_\kappa}^{n_{Q_\kappa}} \rho_{ui}^{(\kappa)} g_{n_\kappa i}^{(\kappa)}\varphi_{n_\kappa}^{(\kappa)} + \\ &- \sum_{\nu\neq\kappa}\sum_{i}^{n_{Q_\nu}}\sum_N \langle\Psi_u^{(\kappa)}|\Phi_N\rangle\, g_{n_\nu i}^{(\nu)} A_{N_{|_{\nu\to i}}} = \\ &= \sum_N \langle\Psi_u^{(\kappa)}|\Phi_N\rangle\,\langle\Phi_N|\hat{H}|\Psi\rangle - \sum_{i,n_\kappa}^{n_{Q_\kappa}} \rho_{ui}^{(\kappa)} g_{n_\kappa i}^{(\kappa)}\varphi_{n_\kappa}^{(\kappa)} + \alpha_A.\end{aligned} \tag{1.4.26}$$

On the other hand,

$$i\sum_{\nu=1}^{s}\sum_{m=1}^{n_{Q_\nu}}\langle\Psi_u^{(\kappa)}|\dot{\varphi}_m^{(\nu)}\Psi_m^{(\nu)}\rangle = i\sum_{m=1}^{n_{Q_\kappa}}\langle\Psi_u^{(\kappa)}|\dot{\varphi}_m^{(\kappa)}\Psi_m^{(\kappa)}\rangle + i\sum_{\nu\neq\kappa}^{s}\sum_{m=1}^{n_{Q_\nu}}\langle\Psi_u^{(\kappa)}|\dot{\varphi}_m^{(\nu)}\Psi_m^{(\nu)}\rangle = \\ = i\sum_{m=1}^{n_{Q_\kappa}}\langle\Psi_u^{(\kappa)}|\dot{\varphi}_m^{(\kappa)}\Psi_m^{(\kappa)}\rangle + \alpha_\varphi = i\sum_{m=1}^{n_{Q_\kappa}}\rho_{um}^{(\kappa)}\dot{\varphi}_m^{(\kappa)} + \alpha_\varphi. \tag{1.4.27}$$

The last equality follows from the same argumentation presented to get to the final form in eq. (1.4.24), and a shorthand α_φ is introduced:

$$\alpha_\varphi = i\sum_{\nu\neq\kappa}^{s}\sum_{m=1}^{n_{Q_\nu}}\langle\Psi_u^{(\kappa)}|\dot{\varphi}_m^{(\nu)}\Psi_m^{(\nu)}\rangle\,. \tag{1.4.28}$$

Combining all the results so far shows the form

$$\langle\Psi_u^{(\kappa)}|\hat{H}|\Psi\rangle = \sum_N\langle\Psi_u^{(\kappa)}|\Phi_N\rangle\langle\Phi_N|\hat{H}|\Psi\rangle - \sum_{i,n_\kappa}^{n_{Q_\kappa}}\rho_{ui}^{(\kappa)}g_{n_\kappa i}^{(\kappa)}\varphi_{n_\kappa}^{(\kappa)} + \\ + i\sum_{m=1}^{n_{Q_\kappa}}\rho_{um}^{(\kappa)}\dot{\varphi}_m^{(\kappa)} + \alpha_\varphi + \alpha_A. \tag{1.4.29}$$

Considering $\alpha_\varphi + \alpha_A$, it is worth expressing α_A as

$$\alpha_A = -\sum_{\nu\neq\kappa}\sum_{i}^{n_{Q_\nu}}\sum_{n_1}^{n_{Q_1}}\cdots\sum_{n_s}^{n_{Q_s}}\langle\Psi_u^{(\kappa)}|A_{n_1\ldots n_{\nu-1}in_{\nu+1}\ldots n_s}\prod_{\mu=1}^{s}\varphi_{n_\mu}^{(\mu)}\rangle\, g_{n_\nu i}^{(\nu)} = \\ = -i\sum_{\nu\neq\kappa}\sum_{i}^{n_{Q_\nu}}\sum_{n_1}^{n_{Q_1}}\cdots\sum_{n_s}^{n_{Q_s}}\langle\Psi_u^{(\kappa)}|A_{N_{\nu\to i}}\varphi_{n_\nu}^{(\nu)}\prod_{\mu\neq\nu}^{s}\varphi_{n_\mu}^{(\mu)}\rangle\langle\varphi_{n_\nu}^{(\nu)}|\dot{\varphi}_i^{(\nu)}\rangle = \\ = -i\sum_{\nu\neq\kappa}\sum_{i}^{n_{Q_\nu}}\sum_{n_\nu}^{n_{Q_\nu}}\langle\Psi_u^{(\kappa)}|\varphi_{n_\nu}^{(\nu)}\Psi_i^{(\nu)}\rangle\langle\varphi_{n_\nu}^{(\nu)}|\dot{\varphi}_i^{(\nu)}\rangle = \\ = -i\sum_{\nu\neq\kappa}\sum_{i}^{n_{Q_\nu}}\sum_{n_\nu}^{n_{Q_\nu}}\sum_{j_1}\cdots\sum_{j_{\kappa-1}}\sum_{j_{\kappa+1}}\cdots\sum_{j_s}\langle A_{j_1\ldots j_{\kappa-1}uj_{\kappa+1}\ldots j_s}\prod_{\substack{\kappa'\neq\kappa\\ \kappa'\neq\nu}}^{s}\varphi_{j_{\kappa'}}^{(\kappa')}|\Psi_i^{(\nu)}\rangle\times \\ \times\langle\varphi_{j_\nu}^{(\nu)}|\varphi_{n_\nu}^{(\nu)}\rangle\langle\varphi_{n_\nu}^{(\nu)}|\dot{\varphi}_i^{(\nu)}\rangle = \\ = -i\sum_{\nu\neq\kappa}\sum_{i}^{n_{Q_\nu}}\sum_{j_1}\cdots\sum_{j_{\kappa-1}}\sum_{j_{\kappa+1}}\cdots\sum_{j_s}\langle A_{j_1\ldots j_{\kappa-1}uj_{\kappa+1}\ldots j_s}\varphi_{j_\nu}^{(\nu)}\prod_{\substack{\kappa'\neq\kappa\\ \kappa'\neq\nu}}^{s}\varphi_{j_{\kappa'}}^{(\kappa')}|\dot{\varphi}_i^{(\nu)}\Psi_i^{(\nu)}\rangle = \\ = -i\sum_{\nu\neq\kappa}\sum_{i}^{n_{Q_\nu}}\langle\Psi_u^{(\kappa)}|\dot{\varphi}_i^{(\nu)}\Psi_i^{(\nu)}\rangle\,. \tag{1.4.30}$$

Therefore,

$$\alpha_\varphi + \alpha_A = \alpha_\varphi = i \sum_{\nu \neq \kappa}^{s} \sum_{m=1}^{n_{Q_\nu}} \langle \Psi_u^{(\kappa)} | \dot{\varphi}_m^{(\nu)} \Psi_m^{(\nu)} \rangle - i \sum_{\nu \neq \kappa}^{s} \sum_{i=1}^{n_{Q_\nu}} \langle \Psi_u^{(\kappa)} | \dot{\varphi}_i^{(\nu)} \Psi_i^{(\nu)} \rangle = 0. \tag{1.4.31}$$

And then

$$i \sum_{m=1}^{n_{Q_\kappa}} \rho_{um}^{(\kappa)} \dot{\varphi}_m^{(\kappa)} = \langle \Psi_u^{(\kappa)} | \hat{H} | \Psi \rangle - \sum_N \langle \Psi_u^{(\kappa)} | \Phi_N \rangle \langle \Phi_N | \hat{H} | \Psi \rangle + \sum_{m,n_\kappa}^{n_{Q_\kappa}} \rho_{um}^{(\kappa)} g_{n_\kappa m}^{(\kappa)} \varphi_{n_\kappa}^{(\kappa)}. \tag{1.4.32}$$

With slight reformulation of the above we get

$$\langle \Psi_u^{(\kappa)} | \hat{H} | \Psi \rangle = \sum_{n_\kappa=1}^{n_{Q_\kappa}} \langle \Psi_u^{(\kappa)} | \hat{H} | \varphi_{n_\kappa}^{(\kappa)} \Psi_{n_\kappa}^{(\kappa)} \rangle = \sum_{n_\kappa=1}^{n_{Q_\kappa}} H_{un_\kappa}^{(\kappa)} \varphi_{n_\kappa}^{(\kappa)}, \tag{1.4.33}$$

where $H_{un_\kappa}^{(\kappa)}$ is called the MCTDH mean-field corresponding to configurations of the κth single-hole function,

$$H_{nm}^{(\kappa)} = \langle \Psi_n^{(\kappa)} | \hat{H} | \Psi_m^{(\kappa)} \rangle \qquad n, m = 1, 2, \ldots, n_{Q_\kappa}. \tag{1.4.34}$$

On the other hand,

$$\begin{aligned}
&\sum_N \langle \Psi_u^{(\kappa)} | \Phi_N \rangle \langle \Phi_N | \hat{H} | \Psi \rangle = \\
&= \sum_{j_1} \cdots \sum_{j_{\kappa-1}} \sum_{j_{\kappa+1}} \cdots \sum_{j_s} \sum_{n_1} \cdots \sum_{n_s} \langle A_{j_1 \ldots j_{\kappa-1} u j_{\kappa+1} \ldots j_s} \prod_{k' \neq \kappa} \varphi_{j_{\kappa'}}^{(\kappa')} | \varphi_{n_\kappa}^{(\kappa)} \prod_{\mu \neq \kappa}^{s} \varphi_{n_\mu}^{(\mu)} \rangle \\
&\qquad \times \langle \varphi_{n_\kappa}^{(\kappa)} \prod_{\mu \neq \kappa}^{s} \varphi_{n_\mu}^{(\mu)} | \hat{H} | \Psi \rangle = \\
&= \sum_{j_1} \cdots \sum_{j_{\kappa-1}} \sum_{j_{\kappa+1}} \cdots \sum_{j_s} \sum_{n_\kappa}^{n_{Q_\kappa}} | \varphi_{n_\kappa}^{(\kappa)} \rangle \langle \varphi_{n_\kappa}^{(\kappa)} | \langle A_{j_1 \ldots j_{\kappa-1} u j_{\kappa+1} \ldots j_s} \prod_{\mu \neq \kappa} \varphi_{j_\mu}^{(\mu)} | \hat{H} | \Psi \rangle = \\
&= \hat{P}^{(\kappa)} \langle \Psi_u^{(\kappa)} | \hat{H} | \Psi \rangle ,
\end{aligned} \tag{1.4.35}$$

where the operator of projection on the sub-space spanned by all the SPFs corresponding to the κth degree of freedom is defined as

$$\hat{P}^{(\kappa)} = \sum_{n_\kappa=1}^{n_{Q_\kappa}} | \varphi_{n_\kappa}^{(\kappa)} \rangle \langle \varphi_{n_\kappa}^{(\kappa)} | . \tag{1.4.36}$$

Putting back eq. (1.4.33) and eq. (1.4.36) into eq. (1.4.32) yields the working equations of motions for the single-particle functions,

$$i \sum_{m=1}^{n_{Q_\kappa}} \rho_{um}^{(\kappa)} \dot{\varphi}_m^{(\kappa)} = (1 - \hat{P}^{(\kappa)}) \sum_{n_\kappa=1}^{n_{Q_\kappa}} H_{un_\kappa}^{(\kappa)} \varphi_{n_\kappa}^{(\kappa)} + \sum_{m,n_\kappa}^{n_{Q_\kappa}} \rho_{um}^{(\kappa)} g_{n_\kappa m}^{(\kappa)} \varphi_{n_\kappa}^{(\kappa)}. \tag{1.4.37}$$

The above equation, along with eq. (1.4.20), form the cornerstone of the MCTDH-framework, the most general formulation of the problem at hand, independently of the system under study.

1.5 Floquet-method

The Floquet-picture is an often employed approximation because several molecular dynamical processes gain a picturesque explanation when the full Hamiltonian is transformed to the Floquet Hamiltonian. This framework can be derived by considering the time-dependent Schrödinger-equation (TDSE) whose Hamiltonian is periodic in time due to the interaction of the system with an external field of frequency ω. According to the Floquet-theorem [40], the solution $\Psi_\alpha(\vec{r},t)$ of the TDSE can be given as

$$\Psi_\alpha = e^{-i\varepsilon_\alpha t}\Phi, \tag{1.5.1}$$

with $\Phi \equiv \Phi(\vec{r},t)$ denoting a periodic function of time period T and ε_α is the characteristic exponent. By writing Φ utilising Fourier-expansion and expanding its Fourier-components $f_\alpha^{(n)}(\vec{r})$ in the basis $\left\{ |\beta(\vec{r})\rangle \right\}$ formed by the eigenstates of the field-free Hamiltonian $\hat{H}_{\text{field}-\text{free}}$

$$f_\alpha^{(n)} = \sum_\beta \Phi_{\alpha\beta}^{(n)} |\beta\rangle \tag{1.5.2}$$

Ψ_α takes the form

$$\Psi_\alpha = e^{-i\varepsilon_\alpha t} \sum_{n=-\infty}^{\infty} \sum_\beta \Phi_{\alpha\beta}^{(n)} e^{-in\omega t} |\beta\rangle \,. \tag{1.5.3}$$

Substituting this expansion into the TDSE and making use of some additional alterations yield [41]

$$\sum_{n=-\infty}^{\infty} \sum_\beta \Big\{ \langle\alpha|\hat{H}^{(m-n)}|\beta\rangle - (\varepsilon_\alpha + m\omega)\delta_{mn}\delta_{\alpha\beta} \Big\} \Phi_{\alpha\beta}^{(n)} = 0. \tag{1.5.4}$$

In the above expresson, $\hat{H}^{(n)}$ is given by

$$\hat{H}^{(n)} = \frac{1}{T}\int_0^T \hat{H} e^{in\omega t} dt. \tag{1.5.5}$$

With the help of the Floquet-state [42] notation $|\alpha n\rangle$, eq. (1.5.4) can be written as

$$\sum_{\gamma}\sum_{k}\langle\alpha n|\hat{H}_F|\gamma k\rangle\,\Phi^{(k)}_{\gamma\beta}=\varepsilon_{\beta}\Phi^{(n)}_{\alpha\beta}, \tag{1.5.6}$$

with

$$\langle\alpha n|\hat{H}_F|\beta m\rangle=\hat{H}_{F_{\alpha n,\beta m}}=\hat{H}^{(n-m)}_{\alpha\beta}+n\omega\delta_{\alpha\beta}\delta_{nm}. \tag{1.5.7}$$

$\hat{H}_F$ is the Floquet Hamiltonian, independent of time [41].
Although $\hat{H}_F$ is time-independent, it is an infinite matrix characterised with the two set of pair of indices, αn and βm. For two electronic states considered and the laser-molecule interaction handled within the dipole approximation, most of the matrix elements in the Floquet Hamiltonian might be neglected. In particular, if the intensity of the external field is not too high so that only single-photon processes take place, it is sufficient to consider a 2x2 block of the infinite matrix of $\hat{H}_F$ only. This [42, 43] is given by

$$\hat{H}_F=\begin{pmatrix}-\frac{1}{2M_r}\frac{\partial^2}{\partial R^2}+E_1(R) & \frac{1}{2}V_{12}\\ \frac{1}{2}V_{21} & -\frac{1}{2M_r}\frac{\partial^2}{\partial R^2}+E_2(R)-\hbar\omega\end{pmatrix}, \tag{1.5.8}$$

where M_r is the reduced mass, $E_1(R)$ and $E_2(R)$ are the potential energies corresponding to the electronic states and $\hbar\omega$ is the photonenergy. $V_{12}=V_{21}$ denotes the potential energy corresponding to the interaction of the transition dipole moment of the system with the static external electric field of magnitude E_0.

Having discussed the general theory, that in one way or other are connected to my work, in what follows I present the results that my dissertation is based on. Most of these deal with the study of dissociation dynamics by numerically calculating the relevant physical quantities in the MCTDH framework. I discuss my results in the framework of the intensively investigated field of light induced non-adiabatic phenomena, for example the effect of light-induced conical intersections (LICI), light-induced avoided crossings (LIAC), bond hardening/softening and vibrational trapping, or the effect of some other important properties of the system.

Chapter 2

Dissociation dynamics of D_2^+ and vibrational trapping

The field free Hamiltonian of a molecular system not too large in size can be calculated by employing standard methods of electronic structure calculations as described in previous chapters. Having done so, the next step involves the construction of the Hamiltonian by including the relevant quantities, such as the field-free potential energy curves and the dipole moments of the molecule. Upon subjecting the system to external electric field of sufficiently high intensities, significant changes can be observed in the dissociation dynamics. This is due to the fact that the resulting strong couplings between the electronic states alter the potential landscape, hence the underlying dynamics and the dissociation yield measured. This phenomenon called bond softening or bond hardening was also experimentally confirmed, first in [44, 45]. Related studies on the effects of the vibrational trapping, that predate [46, 47] the first experimental observations, are also available. The role of LIACs created with high intensity fields was shown to be significant in the dissociation process [48, 49] and they were found to be playing an important role in stabilisation of the molecule, leading to the suppression of the dissociation yield. It was also found that coincidence of the field-free (diabatic) and the laser-induced (adiabatic) vibrational eigenenergies can lead to decreasing dissociation probabilities, in itself a very remarkable explanation.

In the present section I discuss my results [50] acquired by putting the above mentioned qualitative explanation of the vibrational trapping to test, while keeping the applied laser intensity fixed and varying the photon energies of the field. This is in contrast to what has been done in

earlier studies (for example [48,49,51]), where the energy was kept fixed and the intensity varied. By carrying out these simulations my goal is to set up a more quantitative connection between basic physical quantities and the observed dissociation yield.

2.1 The D_2^+ system

The molecular deuterium ion, being the most simple molecular system along with the hydrogen molecule, has the significant advantage compared to the neutral counterpart in the aspect that it does not have electron correlation. This simplifies the description to a great extent. In particular, analytical potential energy curves and transition dipole moments are also available, moreover there exist several studies on D_2^+ (or H_2^+ for that matter) that do not make use of the usual molecular physical treatment [52,53].

Working in a two-level framework, the diabatic or field-free Hamiltonian (1D) can be given as a 2×2 matrix of the form

$$\hat{H}_{dia} = \begin{pmatrix} -\frac{1}{2M_r}\frac{\partial^2}{\partial R^2} + V_1(R) & 0 \\ 0 & -\frac{1}{2M_r}\frac{\partial^2}{\partial R^2} + V_2(R) \end{pmatrix} \tag{2.1.1}$$

where M_r is the reduced mass, R is the vibrational coordinate, $V_1(R)$ and $V_2(R)$ are the diabatic potentials corresponding to the $1s\sigma_g$ and $2p\sigma_u$ electronic states, borrowed from [43,54]. In the presence of an external field, the laser-matter interaction couples the two electronic states, yielding additional terms at the off-diagonals of eq. (2.1.1). The time-dependent Hamiltonian then reads

$$\hat{H}_t = \begin{pmatrix} -\frac{1}{2M_r}\frac{\partial^2}{\partial R^2} + V_1(R) & 0 \\ 0 & -\frac{1}{2M_r}\frac{\partial^2}{\partial R^2} + V_2(R) \end{pmatrix} + \\ + \begin{pmatrix} 0 & f(t)E_0\mu(R)\cos\theta\cos\omega t \\ f(t)E_0\mu(R)\cos\theta\cos\omega t & 0 \end{pmatrix}. \tag{2.1.2}$$

In eq. (2.1.2) $f(t)$, E_0 and ω are the envelope, electric field amplitude and the frequency of the laser pulse, respectively. $\mu(R)$ stands for the transition dipole moment coupling the two electronic states, taken from [43,54] as well, and θ denotes the angle between the polarization of the field and molecular axes. Although in the case of D_2^+ there are analytical forms of $\mu(R)$ available, in general this quantity needs to be calculated by determining the matrix elements of $\mu(R)$ between the electronic wave functions

Φ_i and Φ_j of the electronic states that are to be taken into account in the subsequent nuclear dynamics simulations; $\mu_{ij}(R) = -\langle\Phi_i|\sum_k r_k|\Phi_j\rangle$, with r_k indicating the electronic coordinate of the kth electron.
To get the form present at the off-diagonals, the dipole approximation is utilised which is widely used and in general appropriate whenever the molecule is sufficiently small compared to the wavelength of the applied field. This holds for the parameters I used throughout the study presented in this chapter.

2.2 Model adiabatic Hamiltonian

In case of calculating the adiabatic eigenenergies, an approximate form for the adiabatic Hamiltonian is constructed. For relatively low intensity fields, which is the case throughout this study, a model Hamiltonian for the upper adiabatic potential can be approximated as

$$\begin{aligned}\hat{H}_{adi,model} = -\frac{1}{2M_r}\frac{\partial^2}{\partial R^2} + V_{model} = -\frac{1}{2M_r}\frac{\partial^2}{\partial R^2} + \\ + (V_2(R) - \hbar\omega)\cdot\Theta(R_{CR}(\lambda) - R) + V_1(R)\cdot\Theta(R - R_{CR}(\lambda))\end{aligned} \tag{2.2.1}$$

where $\hbar\omega$ is the photonenergy of the laser field and λ its wavelength. Θ is the Heaviside step function and R_{CR} denotes the internuclear distance at which the photon-dressed state $V_2(R) - \hbar\omega$ crosses the lower diabatic potential $V_1(R)$,

$$V_2(R_{CR}) - \hbar\omega = V_1(R_{CR}). \tag{2.2.2}$$

Figure 2.1 features the potentials used throughout the simulations.

2.3 Numerical simulations

2.3.1 Wave function

The numerical calculations were carried out with the MCTDH package. As the vibrational coordinate R is the only dynamical variable included, the general MCTDH wave function given in eq. (1.4.1) simplifies and assumes the form

$$\Psi(R,t) = \sum_{i_R=1}^{N_R} C_{i_R}^{(R)}(t)\chi_{i_R}^{(R)}(R). \tag{2.3.1}$$

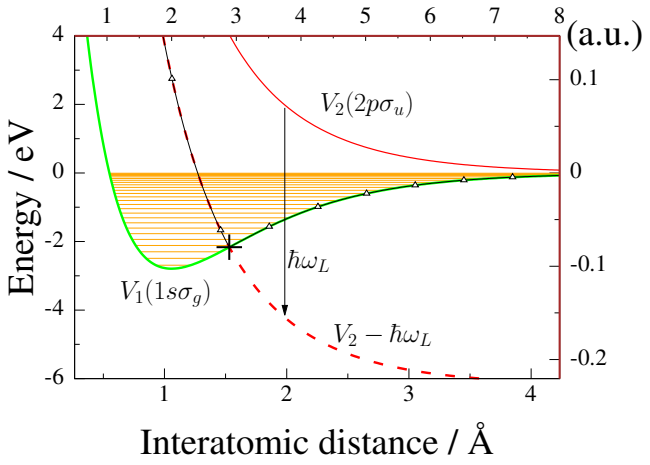

Figure 2.1: *Potential energies.*
The solid green and red curves show the diabatic potentials V_1 and V_2, while the red dashed one represents the photon dressed state $V_2 - \hbar\omega_L$ corresponding to $\hbar\omega_L = 6.199$ eV. The crossing of this latter curve and the V_1 state is marked with $+$. The black curve marked with $\vartriangle$ denotes the model potential in eq. (2.2.1) for the same photon energy $\hbar\omega_L$. In addition, several vibrational eigenenergies of V_1 are drawn as horizontal lines as well.

The vibrational coordinate itself is treated by using fast Fourier discrete-variable representation (FFT-DVR) [55, 56]. In the case of calculations focusing on the dissociation dynamics, the time-dependent Hamiltonian in eq. (2.1.2) is used and $N_R = 2048$ basis elements are employed covering the range of internuclear separation from 0.1 au to 80 au. In these cases I choose the initial wave function to be either an eigenstate ψ_ν of the diabatic Hamiltonian eq. (2.1.1) or superposition of said eigenstates. In the former case of initial conditions, $\nu = 0, 1, 2, \ldots, 9$ are chosen throughout the simulations. As for the latter case of initial conditions, since not only one, but several vibrational eigenstates are present, the dissociation probability observed does not correspond to a single vibrational state. In this situation, I calculated the kinetic energy release (KER) spectra of the fragments and then the differential dissociation rate, that corresponds to the photon energy shifted vibrational eigenenergy, $E_\nu + \hbar\omega$, is determined.

However, regardless of the initial wave function, the initial orientation of the molecule is always assumed to be parallel to the laser field ($\theta = 0$) in my actual calculations.

I also needed to determine the eigenstates and eigenenergies (ψ_ν ; E_ν) of the diabatic Hamiltonian eq. (2.1.1), and the eigenstates and

eigenenergies (φ_ν ; ε_ν) of the model adiabatic Hamiltonian eq. (2.2.1). For solving the corresponding time-independent Schrödinger-equations that provides the quantities sought for, a lower value of N_R is sufficient covering shorter internuclear distances. In particular, $N_R = 256$ covering the internuclear distances 0.1 au – 10.05 au are used.

2.3.2 Complex absorbing potentials and the laser parameters. Static quantities

During the propagation time $t_f = 350.0$ fs, some parts of the wavepacket inevitably reach the end of the simulation "box" located at 80 au. These parts of the wavepacket dissociate and they need to be absorbed in order to be measured and contribute to the dissociation yield. Moreover, if they are not absorbed, they might be reflected at the end of the "box" causing non-physical interferences and impair the results of the simulation.

In the MCTDH scheme, the most effective tool of absorbing the dissociating parts is by means of complex absorbing potentials (CAP) [57,58]. They are given by

$$-iW(R) = -i\eta(R - R_0)^b \cdot \Theta(R - R_0) \tag{2.3.2}$$

with η, R_0 and b representing the strength, starting point and order of the CAP, respectively and Θ denotes the Heaviside-function. This complex potential is then added to the Hamiltonian eq. (2.1.2). The MCTDH package provides tools that are able to determine the optimal parameters [59] for which the reflection probability (or transmission probability for that matter) are minimal. With the aid of them, the parameters that I used are

$$\eta = 5 \cdot 10^{-5} \text{ au} \qquad R_0 = 70 \text{ au} \qquad b = 3 \tag{2.3.3}$$

for the ground electronic state V_1 and

$$\eta = 2.36 \cdot 10^{-3} \text{ au} \qquad R_0 = 75 \text{ au} \qquad b = 3 \tag{2.3.4}$$

for the V_2 excited state. With the CAP in place the dissociation probability P_d and the KER spectra $P_{KER}(E)$ can then be calculated [38] by evaluating the integrals

$$P_d = \int_0^\infty \langle \Psi(t)|W|\Psi(t)\rangle \, dt \tag{2.3.5}$$

and

$$P_{KER}(E) = \int_0^\infty dt \int_0^\infty \langle \psi(R,\theta,t)|W|\psi(R,\theta,t')\rangle \, e^{-iE(t-t')} dt'. \tag{2.3.6}$$

As for the KER spectra, its calculation is only needed for the simulations starting from the Franck-Condon distribution and the results corresponding to $E_\nu + \hbar\omega$ are sought due to the reasons detailed in the previous section.
In the calculations I treat the wavelength λ of the laser as a parameter and it falls in the interval $[50\text{ nm}; 400\text{ nm}]$, with a step size of $\Delta\lambda = 1$ nm. This range proved to be wide enough to contain all dissociation minima for all of the studied cases.

In the time-dependent calculations, the intensity is kept fixed at $I_0 = 10^{11}$ W/cm^2, the shape of the pulse is a linearly polarised Gaussian with pulse duration in FWHM chosen to be $t_p = 30$ fs and centered around $t_c = 0$ fs (starting from individual vibrational states) or $t_c = 34$ fs (starting from Franck-Condon distribution).

In addition to the P_d dissociation probabilities, static quantities based on the diabatic and adiabatic eigenenergies, and the adiabatic and diabatic eigenstates were also calculated. These are the difference of the adiabatic and diabatic eigenenergies,

$$\Delta E_{\nu,\nu'}(\lambda) = \varepsilon_{\nu'}(\lambda) - E_\nu \tag{2.3.7}$$

and the overlap

$$S_{\nu,\nu'}(\lambda) = \langle \varphi_{\nu'}(\lambda, R) | \psi_\nu(R) \rangle = \int_{-\infty}^{\infty} \varphi^*_{\nu'}(\lambda, R) \psi_\nu(R) dR \tag{2.3.8}$$

of the diabatic and adiabatic eigenstates.

2.4 Dissociation probability

In order to be able to relate any of the static quantities based on the diabatic/adiabatic eigenenergies and eigenstates to the observed dissociation minima I wanted to have as many of the latter determined in the present framework as possible. Doing so I found the $\lambda \in [50; 400]$ to be sufficient even for those simulations that started out from the highest excited vibrational state $\psi_{\nu=9}$ considered. By doing so I also expanded on the previous results presented for a comparatively limited range of photon energies in [60].

Figure 2.2 shows an example of the dissociation probability for the case when the propagation starts out from the $\psi_{\nu=4}$ diabatic vibrational eigenstate. In addition, the calculations were repeated for initial conditions when the wave function is prepared as superposition of eigenstates.

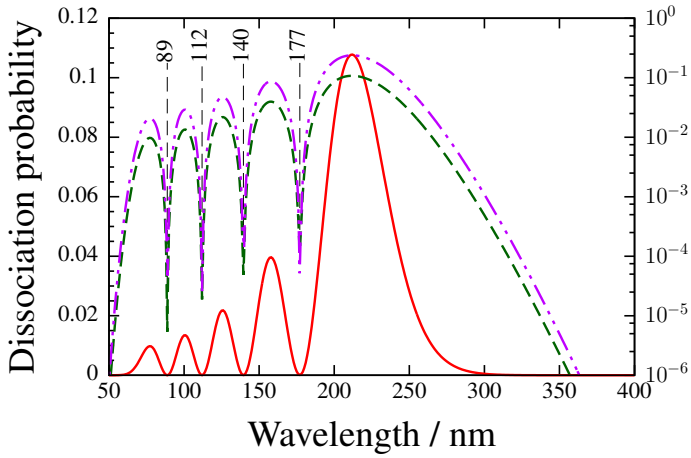

Figure 2.2: *Dissociation probability as a function of the laser wavelength.* The solid red curve corresponds to the linear scale on the left and presents the probabilities obtained in the simulations starting from the $\psi_{\nu=4}$ diabatic eigenstate. The same quantity is also shown by the green dashed curve on a logarithmic scale on the right. Finally, the magenta dashed-dotted curve denotes the differential dissociation rate on the same logarithmic scale and corresponds to the calculations that are initialised from the Franck-Condon distribution.

Four sharp minima of the dissociation probability can be observed at the wavelengths

$$\{\lambda_D(4,0),\ \lambda_D(4,1),\ \lambda_D(4,2),\ \lambda_D(4,3)\} = \{177\text{ nm}, 140\text{ nm}, 112\text{ nm}, 89\text{ nm}\}. \tag{2.4.1}$$

Moreover, there is a remarkable agreement between the results extracted from the simulations starting out from the superposition of the eigenstates (obtained from the KER spectra corresponding to the $E_{\nu=4} + \hbar\omega$ energy; dashed-dotted curve) and those results obtained by initiating the dynamics in the $\psi_{\nu=4}$ vibrational eigenstate. They follow each other closely, suggesting that there is practically no significant difference between the two cases as far as the shapes of the curves and the minima positions are concerned, and the latter is what I focus on here. Other results obtained for the cases $\nu \neq 4$ confirm this suggestion as well, they produce very similar results for both cases of initial conditions.

Due to this finding and for the sake of simplified discussion and presentation, further sections will be restricted to the discussion of results obtained when the dynamics is initiated from individual ψ_ν states and I set out to test the original explanation of vibrational trapping based on the coincidence of the diabatic and adiabatic energy levels while also trying to provide more quantitative relations between the calculated dissociation minima λ_D and the basic static quantities introduced previously. Table 2.1 lists the dissociation minima obtained when initiating the dynamics from the first six ($\nu = 0, 1, 2, \ldots, 5$) ψ_ν diabatic eigenstates.

ν, ν'	$\lambda_D(\nu, \nu')$ [nm]	ν, ν'	$\lambda_D(\nu, \nu')$ [nm]
1,0	111	4,0	177
		4,1	140
2,0	133	4,2	112
2,1	100	4,3	89
3,0	155	5,0	201
3,1	120	5,1	160
3,2	94	5,2	130
		5,3	106
		5,4	85

Table 2.1: λ_D dissociation minima acquired by starting the propagation in the ψ_ν vibrational eigenstate. Employing external electric fields with wavelengths λ_D practically results in no dissociation, similarly to what is shown in Figure 2.2.

2.5 Energy differences and overlap of vibrational eigenstates

The $\Delta E_{\nu,\nu'}(\lambda)$ difference of the adiabatic and diabatic eigenenergies is considered as well as the overlaps $S_{\nu,\nu'}(\lambda)$ of the eigenstates. These quantities correspond to the solutions of the time independent Schrödinger equation with the Hamiltonians eq. (2.1.1) (diabatic situation) and eq. (2.2.1) (adiabatic situation). The smaller the difference $\Delta E_{\nu,\nu'}$ is the more enhanced the vibrational trapping effect gets; the initial diabatic wave function can be more effectively trapped in the upper adiabatic potential. This should also have a fingerprint in the value of the overlap $S_{\nu,\nu'}$; the closer it is to unity the more similar the diabatic and adiabatic eigenstates are thus making the trapping easier to occur.

However, considering the form of the adiabatic model Hamiltonian, due to the form of the model potential V_{model} the adiabatic eigenenergies $\varepsilon_{\nu'}$ are expected to exceed the E_ν diabatic ones whenever $\nu' \geq \nu$ holds. This observation allows for determining $\Delta E_{\nu,\nu'}$ and $S_{\nu,\nu'}$ in the cases $\nu' \leq \nu$ only. Figure 2.3 elaborates on these results keeping the $\nu = 4$ case as an example.

Recalling the explanation for the vibrational trapping or bond hardening phenomenon, the special λ_D wavelengths are expected to be closely related to the wavelengths λ_E and λ_O. The ratios λ_O/λ_D and λ_E/λ_D can account for how well these values agree. If no other circumstances beside the coincidence of the eigenenergies and eigenstates play important role in the vibrational trapping, then the above ratios should lie very close to unity. However, as Table 2.2 clearly demonstrates, this is not the case. In fact, these ratios deviate from 1 within a range of $5 - 15$ % in all studied cases. Although deviations of this magnitude are still acceptable for such a simple model as described by the model Hamiltonian eq. (2.2.1), there might be other processes or circumstances that play part in the molecular stabilisation beside the conditions discussed so far.

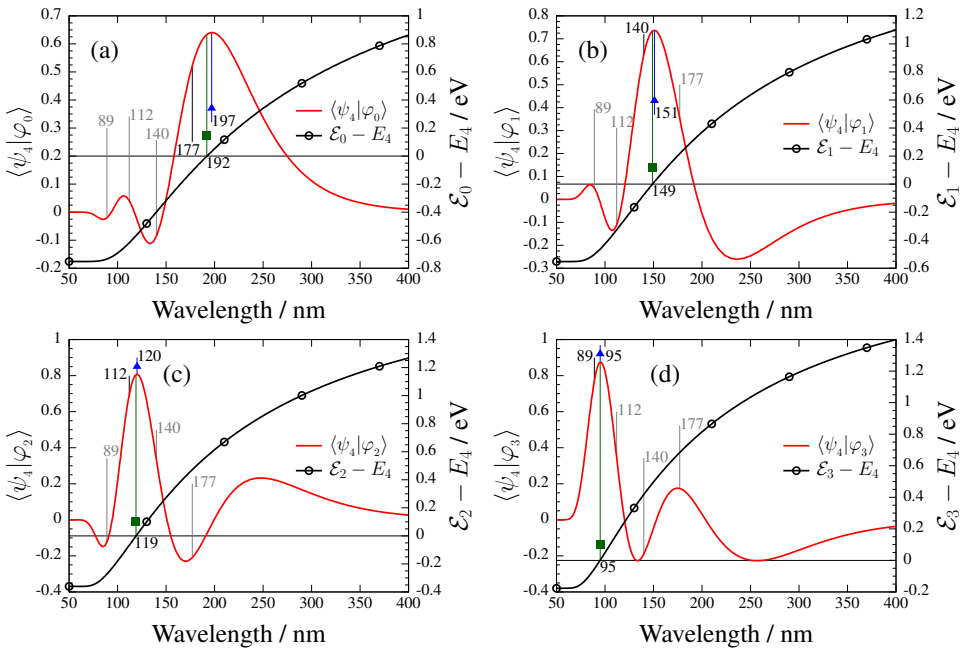

Figure 2.3: The overlaps of the diabatic eigenstate $\psi_{\nu=4}$ and the adiabatic states $\varphi_{\nu'}$ $(\nu' < \nu)$ shown on the left axis and the difference of the eigenenergies $\Delta E_{\nu',\nu}$ on the right axis as a function of the wavelength.
The vertical bars without markers represent the $\lambda_D(\nu,\nu')$ dissociation minima. The bars with ■ denote $\lambda_E(\nu,\nu')$ for which the difference of the eigenenergy is minimal while bars with ▲ represent $\lambda_O(\nu,\nu')$ corresponding to the position of maximal overlap.

2.6 The role of the nodal structure

Careful considerations reveal a special relationship between the maximum of the overlap of the eigenstates $S_{\nu,\nu'}$ and the positions of the nodes R_n of the diabatic eigenstate ψ_ν. R_n is also displayed in Table 2.2.

Sufficiently large overlaps can be acquired when the nodes of the diabatic eigenstates are located close to those of the adiabatic eigenstates. In addition, the adiabatic function fades to zero where the adiabatic potential exceeds the adiabatic energy level. Applying a photon energy corresponding to the wavelength λ_D now leads to negligible dissociation rates and thus the diabatic and adiabatic vibrational energies should be similar. In these circumstances a simple estimation gives that the adiabatic wave function approaches zero where the adiabatic potential gets close to the energy of the diabatic eigenstate. Ultimately, a large overlap can be expected when the coincidence of the adiabatic potential and the diabatic eigenenergy occurs around one of the nodes of the diabatic eigenstate.

$\lambda_{E_\nu}(\nu,\nu')$ denotes the wavelength for which the adiabatic potential matches the energy of the diabatic eigenstate at the $(\nu-\nu')$th node of the diabatic wave function, the latter being denoted by $R_n(\nu,\nu')$. $\lambda_{E_\nu}(\nu,\nu')$ can be calculated according to the expression

$$V_2(R_n(\nu,\nu')) - \hbar\omega_{E_\nu} = E_\nu \quad \Rightarrow \quad \hbar\omega_{E_\nu} = V_2(R_n(\nu,\nu')) - E_\nu. \quad (2.6.1)$$

Another approach from the point of view of the diabatic node structure takes into consideration the light induced picture of dissociation. In this case, the nonadiabatic coupling is the largest in the vicinity of the crossing of the diabatic ground state and the dressed excited state potentials $(V_2 - \hbar\omega)$. If the applied photonenergy results in the crossing getting close to one of the R_n nodes of the diabatic eigenstate then the dissociation yield can be expected to decrease. $\lambda_\times(\nu,\nu')$ denotes the wavelength that produces the above circumstance,

$$V_2(R_n(\nu,\nu'))-\hbar\omega_\times = V_1(R_n(\nu,\nu')) \;\Rightarrow\; \hbar\omega_\times = V_2(R_n(\nu,\nu'))-V_1(R_n(\nu,\nu')). \quad (2.6.2)$$

In one way or another, both λ_{E_ν} and $\lambda_\times$ are based on the positions of the nodes of diabatic eigenstates ψ_ν. Table 2.2 also includes their values and Figure 2.4 serves as a visual representation of their meaning.

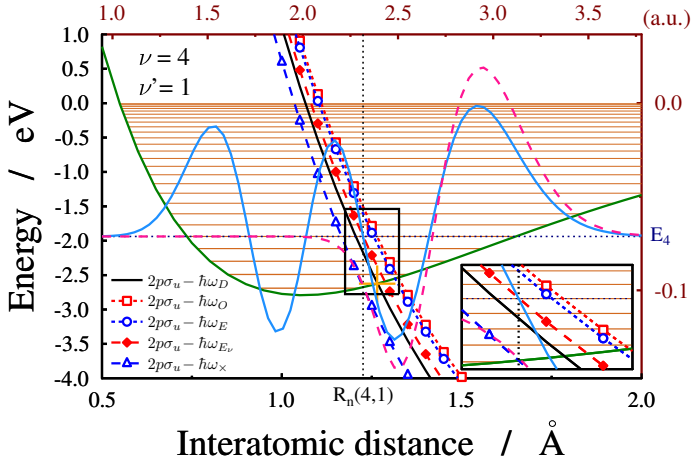

Figure 2.4: *The $V_1(1s\sigma_g)$ ground state potential (green curve) along with five different dressed excited states.*
Each of the dressed states are formed via shifting the excited state $V_2(2p\sigma_u)$ by a photon energy corresponding to the wavelengths λ_D (solid black curve) and λ_O, λ_E, λ_{E_ν} and $\lambda_\times$ denoted by the dashed curves marked with □, ○, ◆ and △, respectively. Additionally, the adiabatic φ_1 state for the case of maximal overlap (wavelength $\lambda_O(4,1)$) and the diabatic ψ_4 eigenstate are also plotted with their zero line placed at the E_4 diabatic vibrational energy level.
A zoom of the central area is also shown in the lower right corner.

The result of comparing the newly introduced wavelengths by calculating the ratios $\lambda_{E_\nu}/\lambda_D$ and $\lambda_\times/\lambda_D$ are summarised in Figure 2.5a.

Among λ_{E_ν} and $\lambda_\times$, λ_{E_ν} is the best performing one and particularly for the first seven lowest lying vibrational eigenstates studied, it provides a better prognosis for λ_D than either λ_E or λ_O.

At this point an additional improvement is possible by noticing that λ_{E_ν} and $\lambda_\times$ are off in the opposite directions with respect to the dissociation minima. Moreover, $\lambda_\times$ underestimates λ_D approximately twice as much as λ_{E_ν} overestimates it. Using this, semi-empirical formulas based on different kinds of means can be formulated that exploit the above

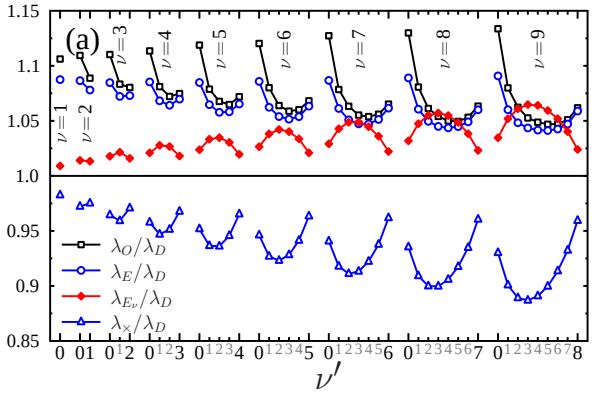

Figure 2.5a: Ratios of the characteristic wavelengths, including the node-based ones, λ_{E_ν} and $\lambda_\times$ defined by eq. (2.6.1) and eq. (2.6.2).

observations. These are

$$\overline{\lambda}_a = \frac{\lambda_\times + 2\lambda_{E_\nu}}{3} \quad \leftrightarrow \quad \overline{\omega}_a = \frac{3}{\frac{1}{\omega_\times} + \frac{2}{\omega_{E_\nu}}},$$

$$\overline{\lambda}_g = \sqrt[3]{\lambda_\times \cdot \lambda_{E_\nu}^2} \quad \leftrightarrow \quad \overline{\omega}_g = \sqrt[3]{\omega_\times \cdot \omega_{E_\nu}^2}, \tag{2.6.3}$$

$$\overline{\lambda}_h = \frac{3}{\frac{1}{\lambda_\times} + \frac{2}{\lambda_{E_\nu}}} \quad \leftrightarrow \quad \overline{\omega}_h = \frac{\omega_\times + 2\omega_{E_\nu}}{3},$$

the weighted arithmetic, geometric and harmonic means, respectively. How well these forms forecast the dissociation minima is shown in Figure 2.5b. Except for a few cases for $\nu' = 8, 9$ of $\overline{\lambda}_a$, all of the three means provide very similar results, deviating less than half a percent from λ_D.

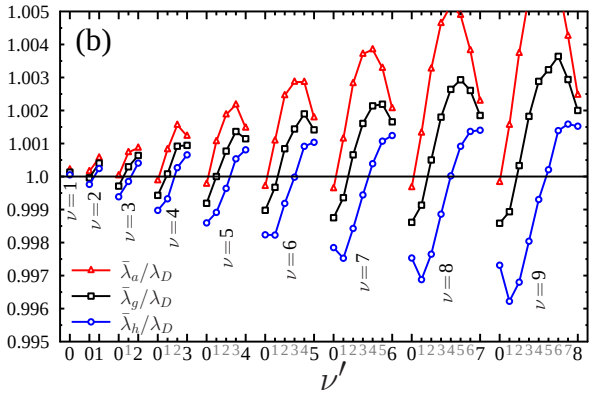

Figure 2.5b: The semi-empirical wavelengths, $\overline{\lambda}_a$, $\overline{\lambda}_g$ and $\overline{\lambda}_h$ measured up against the dissociation minima λ_D. All three of them are in good agreement with the dissociation minima, providing significantly better results than all preceding characteristic wavelengths.

2.7 Conclusions

In this section I discussed my results on testing the vibrational trapping/bond hardening phenomenon and the available explanation for it. In the framework of a model adiabatic Hamiltonian constructed for the low-intensity regime, I determined the diabatic and adiabatic eigenfunctions, the corresponding eigenenergies, the overlaps of said eigenstates and the difference of their eigenenergies. With these static quantities, reproduction of the observed dissociation minima is possible with an error of $5 - 15\%$ which is a fair result considering the simplistic nature of the model Hamiltonian used.

In addition, the nodal structure of the diabatic eigenfunctions were found to play a part in the process of molecular stabilisation due to the fact that the characteristic wavelengths based on the node positions are in very good agreement with the observed dissociation minima.

Making use of them, even more refined, although semi-empirical expressions can be constructed that are capable of forecasting the sought wavelengths with less than half a percent error, a very precise reproduction of λ_D.

However, despite the precision achieved, it is not clear yet why the employed weights such as those used in the formulas are the correct ones from the point of view of physics. There must be a physically valid reason for the $1 : 2$ ratio of $\lambda_\times$ and λ_{E_ν} in their combinations, as well as for the fact why the harmonic mean of the node-based quantities present the best predictions of λ_D for the largest ν' values. On the other hand, $\overline{\lambda}_g$ provides the best agreement with λ_D in the lower regime of ν' values, except for the smallest ones. The physical reasoning behind the above could serve as the topic of a future study.

My discussion of vibrational trapping here used D_2^+ as the example to carry out the calculations. The considerations leading to the node-based quantities seem to be general enough to assume the validity of the present findings in the case of other systems as well.

ν,ν'	λ_D	λ_O	λ_E	λ_{E_ν}	$\lambda_\times$	R_n	ν,ν'	λ_D	λ_O	λ_E	λ_{E_ν}	$\lambda_\times$	R_n
1,0	111.21	123.02	120.94	112.21	109.27	2.05	7,0	258.66	291.60	281.10	266.19	243.32	3.16
							7,1	206.70	222.93	219.37	215.55	189.71	2.82
2,0	133.27	147.85	144.81	135.15	129.57	2.29	7,2	170.00	180.76	178.66	178.28	154.89	2.54
2,1	100.21	109.11	108.03	101.54	97.72	1.90	7,3	141.47	149.29	148.16	148.39	129.20	2.29
							7,4	118.09	124.45	123.67	123.37	108.91	2.05
3,0	154.67	171.72	167.78	157.42	149.17	2.48	7,5	98.08	103.57	103.11	101.62	91.97	1.81
3,1	120.08	130.09	128.75	122.67	115.18	2.13	7,6	79.78	84.98	84.69	81.55	76.74	1.56
3,2	93.54	101.06	100.36	95.03	90.80	1.80							
							8,0	293.15	331.23	319.24	302.48	274.19	3.33
4,0	177.09	197.19	192.21	180.79	169.62	2.66	8,1	234.31	253.22	248.51	245.42	213.03	2.98
4,1	139.53	150.84	149.05	143.41	132.12	2.32	8,2	193.05	204.87	202.61	203.66	173.72	2.70
4,2	111.96	120.04	119.15	114.94	106.51	2.02	8,3	161.23	169.95	168.48	170.44	145.06	2.45
4,3	88.78	95.42	94.97	90.38	85.91	1.72	8,4	135.49	142.27	141.41	142.92	122.74	2.21
							8,5	113.90	119.54	119.00	119.44	104.50	1.99
5,0	201.42	225.35	218.50	206.20	191.71	2.83	8,6	95.12	100.18	99.79	98.76	88.92	1.77
5,1	159.95	172.56	170.31	165.29	149.80	2.49	8,7	77.74	82.67	82.41	79.55	74.67	1.52
5,2	130.10	138.91	137.62	134.62	121.78	2.20							
5,3	106.14	113.02	112.32	109.37	100.37	1.93	9,0	332.84	377.34	363.08	344.38	309.60	3.50
5,4	85.13	91.25	90.69	86.79	82.17	1.66	9,1	265.72	286.96	281.69	279.52	239.35	3.14
							9,2	218.95	232.59	229.52	232.31	194.68	2.85
6,0	228.36	255.84	247.97	234.41	216.07	3.00	9,3	183.16	192.80	191.14	195.02	162.45	2.60
6,1	182.13	196.72	193.49	189.09	168.81	2.66	9,4	154.46	162.00	160.89	164.36	137.60	2.37
6,2	149.22	158.75	157.26	155.50	137.74	2.37	9,5	130.69	136.82	136.08	138.46	117.57	2.15
6,3	123.32	130.57	129.67	128.27	114.47	2.12	9,6	110.45	115.65	115.15	116.18	100.90	1.94
6,4	101.67	107.78	107.14	105.09	95.71	1.87	9,7	92.64	97.36	97.00	96.36	86.37	1.73
6,5	82.20	87.80	87.40	83.92	79.19	1.61	9,8	76.00	80.70	80.47	77.82	72.91	1.49

Table 2.2: Characteristic λ wavelengths corresponding to the ν, ν' ($\nu' < \nu$) different vibrational diabatic and adiabatic levels. R_n denotes the positions of the nodes of ψ_ν diabatic wave functions.

Chapter 3

Berry's phase of light induced conical intersections

Conical intersections (CI) are very important structures in physical chemistry and molecular physics for the reasons outlined in the introduction earlier. Not surprisingly, it is of interest to lay out not only the appropriate conditions that lead to their formation but the correct approaches of probing the presence of a CI, as well.

These important theoretical works have been undertaken and it was argued and proved by several authors ([6, 7] and others) that a crossing between two electronic states of a diatomic system may only exist if they differ in some of their property like their symmetry or multiplicity. Even then, formation of a CI always needs at least two independently variable dynamical parameters. Thus, in diatomic systems where the working Hamiltonian contains a single dynamical variable only, no conical intersections may form. It was also shown by Teller [6] upon linearly approximating the Hamiltonian matrix elements in the vicinity of the degeneracy, that the crossing forms a double cone whose vertex is located at the point of degeneracy.

In polyatomic systems, the dynamical variables that need to be considered are so numerous that appropriately treating all of the relevant ones poses significant computational challenge; in general there are more than enough variables that can be varied and due to this CIs are very abundant in larger molecular systems. These systems also include biologically critical molecules such as DNA. In fact, the abundance of CIs in DNA is what makes it stable against incident radiations (such as cosmic rays) which is a critical attribute needed by the formation of life as we know it.

The requirement corresponding to the needed differences between

the electronic states is lifted when polyatomic systems are considered, though. In these systems electronic states may cross despite not differing in some essential attribute. This is proved and presented with examples in [61, 62]. A very important result of the previous publications is the proof concerning the electronic eigenstates. The proof shows that by requiring the electronic eigenstate to be real valued, it must change sign upon being adiabatically transported along a closed loop of the configuration space encircling the point of degeneracy (CI). This observation may then be seen as a fingerprint of a degeneracy; if the adiabatically slow transportation along the closed curve leads to a sign change in the wave function then at one point along the loop the wave function became degenerate. This very important result of Herzberg and Longuet-Higgins is, in theory, capable of opening ways to probe the molecular configuration space for origins of degeneracies.

Later studies have shown considerable interest in the sign change of the adiabatic electronic eigenfunctions outlined above, particularly in the consequence that it ceases to be single valued under such circumstances. Detailed study of the consequences imposed on the Born-Oppenheimer approximation and how it is applied to simulations of scattering processes was given by Mead and Truhlar [63]. The corresponding theory was later generalised by Berry [64] and the accompanying phase is called Berry's phase. As it was pointed out, this phase is geometrical in the sense that given the system and its parameter space, it is uniquely determined by the closed path along which the eigenstates are transported. Later on an extension to the usual BO coupled-surface equations was derived [65] whose solution appropriately treats difficulties arising due to the degeneracy by construction.

Since the most interest of physical chemistry concentrates on the study of large molecular systems, several works have dealt with the study and interpretation of the geometrical phase associated with natural CIs appearing in small molecules or model systems [66–68], such as the Jahn-Teller model [69, 70].

However, as laser induced CIs have several advantages in allowing one to fine tune the position of the degeneracy and the strength of the non-adiabatic coupling by varying the inducing field, it is of interest to study the topological features of them as well. There are a few works available [10, 11] for the case of the Na_2 molecule, where the line-integral technique was applied to calculate the geometric phase in Floquet picture.

My intent was to go beyond the time independent treatment of [10,11] and apply Berry's original time-dependent adiabatic approach to calculate the geometric phase of a LICI. The example system is the D_2^+

molecule and the details as well as the results of my work are lined out in the following sections.

3.1 Floquet Hamiltonian

In contrast to the full time-dependent Hamiltonian of D_2^+ used for the dissociation dynamics previously described (eq. (2.1.2)), by using the Floquet picture [41,43] one only considers the leading term in the Fourier expansion of the wave function acquired by solving the time-dependent Schrödinger equation. Moreover, following Berry's method of calculating the geometrical phase, the dynamical parameters the Hamiltonian depends on are parameterised so that the corresponding Floquet Hamiltonian depends on time only implicitly. Then the working Hamiltonian contains the electronic states $V_1(R)$, $V_2(R)$ and the laser-matter coupling. Its form is given by

$$\begin{pmatrix} V_1(R) & \frac{E_0\mu(R)\cos\theta}{2} \\ \frac{E_0\mu(R)\cos\theta}{2} & V_2(R) - \hbar\omega \end{pmatrix} \tag{3.1.1}$$

with the appearing quantities having the same meaning as discussed previously in Section 2.1. Figure 3.1 shows the potentials V_1 and V_2 as well as the adiabatic potential energy curves acquired by diagonalising eq. (3.1.1). In order for a crossing to be formed between the adiabatic potentials (in addition to the required two degrees of freedom, now provided by R and θ) it is required that

$$\begin{aligned} &V_1(R) = V_2(R) - \hbar\omega \\ &\frac{E_0\mu(R)\cos\theta}{2} = 0 \quad \Rightarrow \quad \theta = \pi/2 \end{aligned} \tag{3.1.2}$$

Therefore, in the configuration space of D_2^+ the crossing takes place at the points satisfying eq. (3.1.2). In the actual calculations the photon energy used is $\hbar\omega = 1.359$ eV, coupling the states at $R_{CI} = 5$ au and $\theta = \pi/2$. The task is to calculate the geometric phase for closed loops that encircle this point and for other loops that do not.

3.2 Adiabatic transportation along a closed path

The adiabatic theorem states that in case a system is prepared in an eigenstate $\phi(t = 0)$ of its Hamiltonian $\hat{H}(t = 0)$, then slowly varying

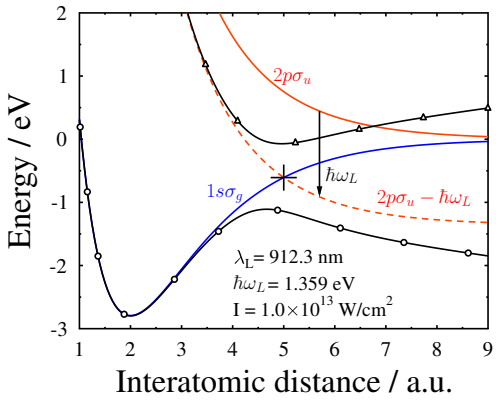

Figure 3.1: Diabatic potential energies $V_1(1s\sigma_g)$ – solid blue – and $V_2(2p\sigma_u)$ – solid red – of the D_2^+ molecule. The dressed state $V_2(2p\sigma_u) - \hbar\omega_L$ (dashed red) forms a LICI with the diabatic ground state at $R = 5$ au, denoted by $+$.
A cut through the adiabatic surfaces obtained at $\theta = 0$ is also shown by solid black lines marked with ∘ (lower adiabatic potential, V_{lower}) and ∆ (upper adiabatic potential, V_{upper}) for field intensity $I_0 = 10^{13}\text{W/cm}^2$ and photon energy $\hbar\omega_L = 1.359$ eV.

$\hat{H}(t)$, the system has enough time to always assume a state that coincides with one of the eigenstates $\phi(t)$ of the instantaneous Hamiltonian $\hat{H}(t)$. This kind of evolution of the initial state $\phi(0)$ can be followed by introducing time dependence into the dynamical variables on which $\hat{H}$ depends, for eq. (3.1.1) $R \equiv R(t)$ and $\theta \equiv \theta(t)$. Subjecting the system to a cyclic adiabatic evolution of period T so that $\hat{H}(t = T) = \hat{H}(t = 0)$ the eigenstate $\phi(R(t = 0), \theta(t = 0))$ from which the evolution is initiated transforms into, as Berry showed,

$$\phi(R(T), \theta(T)) = \left\{ e^{i\gamma(T) - \frac{i}{\hbar}\int_0^T E(R(t),\theta(t))dt} \right\} \cdot \phi(R(t = 0), \theta(t = 0)), \quad (3.2.1)$$

where $E(R(t), \theta(t))$ is the eigenenergy and the expression in the bracket $\{\}$ is the total phase factor of the adiabatic evolution. The two terms it is made of are the dynamical phase factor

$$e^{i\delta(T)} = e^{-\frac{i}{\hbar}\int_0^T E(R(t),\theta(t))dt} \quad (3.2.2)$$

and geometric phase factor

$$e^{i\gamma(T)}. \quad (3.2.3)$$

The total phase $\chi(T)$ accumulated during the evolution is thus given as

$$\chi(T) = \gamma(T) + \delta(T), \quad (3.2.4)$$

the sum of the geometric phase γ and dynamical phase δ. The starting and final states differing by a non-trivial Berry's phase $\gamma(T)$ implies a

degeneracy encircled by the parameterised loop $\{R(t), \theta(t)\}$ and leads to a change of sign of the initial state at $t = T$. In such a case,

$$\gamma(T) = \chi(T) - \delta(T) = \chi(T) + \frac{1}{\hbar}\int_0^T E(R(t), \theta(t))dt = \pm(2n+1)\pi. \quad (n \in \mathbb{Z}) \tag{3.2.5}$$

Otherwise a trivial Berry's phase results and $\gamma(T) = 0$.

For the working expressions of χ and γ I followed [71] in which it is presented that the total phase χ can be calculated by evaluating the autocorrelation function $C(t)$ and from there

$$\chi(t) = \arg\Big\{C(t)\Big\} = \arg\Big\{\ \langle\phi(R(0), \theta(0))|\phi(R(t), \theta(t))\rangle\ \Big\}. \tag{3.2.6}$$

Moreover, an expression for the dynamical phase is given as

$$\delta(t) = \mathrm{Im}\Big\{\int_0^t \langle\phi(R(t'), \theta(t')|\dot{\phi}(R(t'), \theta(t')\rangle\, dt'\Big\}. \tag{3.2.7}$$

When the evolution of $\phi(R(t), \theta(t))$ is governed by the Schrödinger-equation,

$$i \cdot |\dot{\phi}(R(t), \theta(t)\rangle = \hat{H}(R(t), \theta(t))\, |\phi(R(t), \theta(t)\rangle\,, \tag{3.2.8}$$

$\delta(t)$ may be cast into a more convenient form

$$\delta(t) = -\int_0^t \langle\phi(R(t'), \theta(t'))|\hat{H}(R(t'), \theta(t'))|\phi(R(t'), \theta(t'))\rangle\, dt'. \tag{3.2.9}$$

Eq. (3.2.5) is only correct in a strict sense if the cyclic evolution is guaranteed to be an adiabatic one which is essentially taking $T \to \infty$. The parameters actually used decide how long a period T might be considered adiabatic, but the appropriate period, that is adiabatically slow enough, is not known in advance. To work around this, several values of T were taken – as it is described in the section about the parameters I used – and in this sense the results also allows one to deduce what parameters can be considered adiabatic in the given circumstances.

3.3 Methodology

The geometric phase is calculated as $\chi(T) - \delta(T)$ based on eq. (3.2.6) and eq. (3.2.9) at the end of the cyclic evolution. The dynamical variables

R and θ are parameterised so as to form a closed loop (ellipses) in the molecular configuration space. In my case they are taken as

$$R(t) = R_c + \rho_R \cos\beta(t) \tag{3.3.1}$$

$$\theta(t) = \theta_c - \rho_\theta \sin\beta(t). \tag{3.3.2}$$

The centre of the ellipse is defined by (R_c, θ_c) and the lengths of its half-axes are (ρ_R, ρ_θ). The angle $\beta(t)$ then describes how the ellipse is traveled and this is chosen to be

$$\beta(t) = \frac{2\pi}{T} \cdot t + \beta_0. \tag{3.3.3}$$

A natural choice for time period is provided by the period of the laser field $\frac{2\pi}{\omega_L}$ and thus $T = n\frac{2\pi}{\omega_L}$ $(n \in \mathbb{Z})$ transportation periods were used in the calculations. As n increases the transportation is expected to become more and more adiabatic which in turn justifies the application of the adiabatic theorem and the expressions leading to the geometric phase γ.

Table 3.1 details the parameters used throughout the calculations and Figure 3.2 depicts the paths taken displaying the starting points on each loops as well.

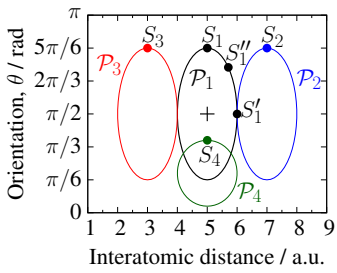

Figure 3.2: The paths taken during the calculations [72]. Dots denote the starting points and the position of the CI is denoted by +.

Path	R_c [$a.u.$]	θ_c [rad]	ρ_R [$a.u.$]	ρ_θ [rad]	β_0 [rad]
$\mathcal{P}_1$	5	$\pi/2$	1	$\pi/3$	$-\pi/2$ (S_1) 0 (S_1') $-\pi/4$ (S_1'')
$\mathcal{P}_2$	7	$\pi/2$	1	$\pi/3$	$-\pi/2$ (S_2)
$\mathcal{P}_3$	3	$\pi/2$	1	$\pi/3$	$-\pi/2$ (S_3)
$\mathcal{P}_4$	5	$\pi/5$	1	$\pi/6$	$-\pi/2$ (S_4)

Table 3.1: Parameters used in $R(t)$, $\theta(t)$ and $\beta(t)$ to describe the paths in the configuration space. For the case of $\mathcal{P}_1$ several different starting points along the curve – determined by β_0 – are considered as well.

I solved the time-dependent Schrödinger equation numerically. This side of the implementation was carried out in C language utilising the implicit fourth order Runge-Kutta integrator with Gaussian points [73] implemented in the GNU Scientific Library [17] (GSL).

The initial state is chosen to be the eigenfunction of the Hamiltonian eq. (3.1.1) with its dependencies R and θ parameterised as given in

eq. (3.3.1) and eq. (3.3.2). The calculations use a fixed photon energy $\hbar\omega_L = 1.359$ eV giving rise to a crossing between the ground $V_1(1s\sigma_g)$ and dressed $V_2(2p\sigma_u) - \hbar\omega_L$ states at $R_{CI} = 5$ a.u. The intensity of the applied field varies between $I = 10^{10}$ W/cm^2 and $I = 10^{15}$ W/cm^2.

3.4 Geometric phase

The first batch of results correspond to while following path $\mathcal{P}_1$ which is the only one that surrounds the CI located at $R = 5$ a.u. The starting point is S_1. Several different intensities and transportation times are probed. The rather lengthy results [72] are most conveniently summarised in Table 3.2.

Intensity	T $[2\pi/\omega_L]$						
$[\mathrm{W/cm^2}]$	50	200	500	2000	5000	20000	50000
field free	$<1{\cdot}10^{-6}$	$<1{\cdot}10^{-6}$	$<1{\cdot}10^{-6}$	$2{\cdot}10^{-6}$	$4{\cdot}10^{-6}$	$15{\cdot}10^{-6}$	$24{\cdot}10^{-6}$
$1 \cdot 10^{10}$	0.0682	-75.0925	32.9789	-82.5002	-192.7763	-29.1699	-10.6957
$3 \cdot 10^{10}$	-3.7613	-29.9996	-29.6432	-49.4776	-12.8597	-2.2615	-0.3007
$5 \cdot 10^{10}$	-5.1357	-24.4448	-96.5521	-13.1177	-3.8062	-0.1775	0.5295
$1 \cdot 10^{11}$	-3.5758	-51.2940	-17.0145	-2.0801	-0.1961	0.7023	0.8809
$3 \cdot 10^{11}$	-9.2701	-4.4822	-0.4876	0.6534	0.8618	0.9655	0.9862
$5 \cdot 10^{11}$	-0.6340	-0.4275	0.4730	0.8705	0.9483	0.9870	0.9948
$1 \cdot 10^{12}$	-1.3928	0.6346	0.8578	0.9646	0.9859	0.9964	0.9986
$3 \cdot 10^{12}$	0.7764	0.9463	0.9785	0.9946	0.9978	0.9994	0.9998
$5 \cdot 10^{12}$	0.8962	0.9741	0.9896	0.9974	0.9990	0.9997	0.9999
$1 \cdot 10^{13}$	0.9481	0.9871	0.9948	0.9987	0.9995	0.9999	0.9999
$3 \cdot 10^{13}$	0.9582	0.9898	0.9959	0.9990	0.9996	0.9999	1.0000
$5 \cdot 10^{13}$	2.9448	0.9883	0.9953	0.9988	0.9995	0.9999	1.0000
$1 \cdot 10^{14}$	14.7622	0.9846	0.9939	0.9985	0.9994	0.9998	1.0000
$3 \cdot 10^{14}$	104.6614	2.9740	0.9897	0.9974	0.9990	0.9997	1.0000
$5 \cdot 10^{14}$	146.1297	20.9600	0.9868	0.9967	0.9987	0.9997	1.0001
$1 \cdot 10^{15}$	190.5541	252.6389	0.9814	0.9954	0.9981	0.9995	1.0003

Table 3.2: An excerpt of Table 2 from [72] showing the difference of the total and dynamical phases given in units of π calculated at the end point of the path ($t = T$) $\mathcal{P}_1$ encircling the CI. The starting point of the surrounding is S_1 (Figure 3.2) and the initial wave function corresponds to the lower adiabatic surface.

In the field free case, one expects 0 for the geometric phase. The results are convincing as can be seen in Table 3.2, although they are not exactly 0. In the case of the relatively low intensity regime ($1 \cdot 10^{10} - 5 \cdot 10^{10}\mathrm{W/cm^2}$) very slow loop times T are needed to consider the evolution as adiabatic. In these situations, even the largest transportation time, $T = 50000$ seems to be not slow enough to assure adiabatic behaviour.

However, as soon as the intensity is being raised, the region of the parameter set (I_0, T) satisfying the requirements of the adiabatic theorem

significantly expands. In fact, with $I \geq 10^{12}\mathrm{W/cm^2}$ choosing $T \geq 500$ round trip times is sufficient and the calculated values of γ lie very close to π as one expects.

An even further raise of intensity to about 10^{14} W/cm^2 leads to the problem and its numerical solutions getting more challenging and longer transportation times are required as well. The beginning of the adiabatic region is also slowly shifted to longer times T. This is due to the effect that the derivatives of the adiabatic potentials with respect to the position along the path – defined by $\beta(t)$ – start to significantly exceed those of the diabatic potentials. This demands slower changes in the cyclic evolution, ultimately longer transportation times to allow for adiabatic evolution to happen.

How the geometric phase $\gamma(t)$ evolves is also displayed in Figure 3.3. The shown curves were acquired with path $\mathcal{P}_1$ and $I = 1 \cdot 10^{13}$ W/cm^2. Although the displayed curves behave differently and have differing final values at $t = T$ depending on T, all of them exhibit rather sudden jumps at around $t/T = 0.5$, e.g. when half of the path has already been traveled. These jumps also take place when the autocorrelation function approaches zero. It should be noted, however, that the position of the jump at $t/T = 0.5$ also reflects the symmetry of the path taken since the four end points of the small and large axes of the ellipse all present natural choices for the starting points. Using any of these, the jumps always happen at half the transportation time T. Using an initial position that lies anywhere between the four symmetrical end points of the axes shifts the positions of the jumps relative to $t/T = 0.5$. This is also the case for point S_1'' along path $\mathcal{P}_1$, where it takes place at around $\approx 0.44 \cdot T$.

Table 3.3 compiles results with several paths and starting points used. Results for the paths that do not surround the CI prove to be in good agreement with the expectations as all of them are very close to zero. In addition, the table also shows those results when the initial wave function is prepared to be on the upper adiabatic surface. They provide values very similar to those starting on the lower surface, they only differ in the sign of the geometric phase. In any case, as all of them are in close vicinity of 0, $\pm\pi, \pm 3\pi$ or $\pm 5\pi$ they provide the correct results expected from their arrangement in the configuration space shown in Figure 3.2. The uncertainty related to the exact value of n in $\gamma = \pm(2n+1)\pi$ is related to the fact that at some point – depending on the actual path and starting point used – during the cyclic evolution along the path, the autocorrelation function gets very close to zero; during these periods it becomes rather difficult to track its argument very precisely.

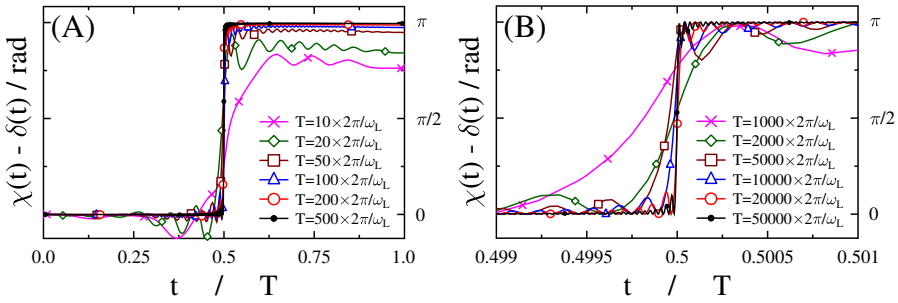

Figure 3.3: The evolution of the difference of the total and dynamical phases for several different cycle times T [72]. The results presented correspond to the starting point S_1 along the ellipse $\mathcal{P}_1$ encircling the LICI. The intensity is $I_0 = 10^{13}\mathrm{W/cm}^2$.
Part **(A)** shows the full time interval $t \in [0, T]$ while **(B)** focuses on emphasizing the sudden jump occurring at $t/T = 0.5$ by restricting the interval to $t/T \in [0.499, 0.501]$.

Path/ Surface	T $[2\pi/\omega_L]$ 500	1000	2000	5000	10000	20000	50000
$\mathcal{P}_1$-S_1/ lower	+0.99483	+0.99741	+0.99871	+0.99948	+0.99973	+0.99985	+0.99993
$\mathcal{P}_1$-S_1/ upper	-0.99483	-0.99742	-0.99871	-0.99948	-0.99974	-0.99987	-0.99995
$\mathcal{P}_1$-S_1'/ lower	+4.98611	+2.99305	+2.99652	+4.99859	+4.99926	+2.99957	+4.99965
$\mathcal{P}_1$-S_1'/ upper	-4.98611	-2.99306	-2.99653	-4.99861	-4.99931	-2.99966	-4.99987
$\mathcal{P}_1$-S_1''/ lower	+0.99483	+0.99741	+0.99871	+0.99948	+0.99973	+0.99985	+0.99993
$\mathcal{P}_1$-S_1''/ upper	-0.99483	-0.99742	-0.99871	-0.99948	-0.99974	-0.99987	-0.99995
$\mathcal{P}_2$-S_2/ lower	-0.00185	-0.00093	-0.00047	-0.00019	-0.00011	-0.00007	-0.00002
$\mathcal{P}_2$-S_2/ upper	+0.00185	+0.00092	+0.00046	+0.00019	+0.00009	+0.00005	+0.00002
$\mathcal{P}_3$-S_3/ lower	-0.00009	-0.00005	-0.00003	-0.00002	-0.00002	-0.00003	-0.00006
$\mathcal{P}_3$-S_3/ upper	+0.00009	+0.00005	+0.00003	+0.00003	+0.00003	+0.00001	+0.00026
$\mathcal{P}_4$-S_4/ lower	-0.04279	-0.02138	-0.01069	-0.00428	-0.00215	-0.00109	-0.00044
$\mathcal{P}_4$-S_4/ upper	+0.04279	+0.02138	+0.01069	+0.00428	+0.00214	+0.00107	+0.00043

Table 3.3: γ in units of π at the end of the paths. Different paths, starting points and initial wave functions are considered. The applied intensity is $I = 1 \cdot 10^{13} \frac{\mathrm{W}}{\mathrm{cm}^2}$ in all cases listed. The data are also available in [72].

3.5 Conclusions

In this section I presented my results for the geometric phase calculations in the case of D_2^+ system when a light induced conical intersection is present in the molecular configuration space.

Expanding on the few available results where a LICI was considered, I calculated the geometric phase with implicit time-dependent adiabatic approach. I used a sufficient parametrisation of the dynamical variables on which the Hamiltonian depends and implemented a code in C language to numerically solve the time-dependent Schrödinger equation. I also used the freely available GSL library for the integrator.

I considered several closed paths in the configuration space and also chose several different starting points along the paths with the initial wave function prepared either on the lower adiabatic or the upper adiabatic surface.

The obtained geometric phase γ is in good agreement with the results that can be expected in the presence of natural CIs. This way the results acquired prove that a geometric phase effect similar to those of natural CIs can be ascribed to LICIs as well, even in the case of following Berry's original method of calculating the geometric phase. The importance of these results lies in the advantages of LICIs when compared to their natural counterparts; namely the ability to fine tune some of their most important properties such as the position of the degeneracy or the strength of the non-adiabatic couplings they give rise to.

A step forward would be to consider the full time-dependent Hamiltonian where the laser-molecule coupling introduces explicit time dependence. In this case the dependence also appears in the adiabatic surfaces and through them in the molecular configuration space as well. This makes the generalisation of Berry's approach so that it can account for this situation rather difficult and requires thorough considerations as to how the adiabatic transportation along a closed path should be realized.

Chapter 4

Orientation of the transition dipole and its impact on dissociation

The very first direct and unambiguous trace of a LICI and its substantial impact on molecular dynamics was acquired upon investigating the angular distribution of the photofragments in dissociation processes of the D_2^+ molecule [74] and other direct indicators of a LICI's presence can be obtained by investigating the field-dressed spectra of a molecule as well, as it was shown with the Na_2 recently [75].

In [74] the authors carefully prepared 2D calculations in which both the vibrational coordinate and the angle between the polarisation direction of the laser field and the molecular axis are treated as independent dynamical variables. Comparing these results to those of 1D calculations when the θ variable is kept fixed and considered as a parameter of the Hamiltonian showed significant differences. The angular distribution of the photofragments revealed striking discrepancies close to the origin of the LICI at $\theta = \pi/2$ where the induced nonadiabatic effects are the strongest. The observed results could be tracked in the evolution of the nuclear density as well, giving clear explanations for the effects of a LICI on the dynamics. Obviously, in the interpretations given in the above work the position of the LICI plays an essential role and the necessary conditions leading to its formation are given by eq. (3.1.2) when the transition dipole moment is parallel to the molecular axis. An interesting task is to consider how these conditions and the effect of a LICI on the dynamics are altered by taking a system whose TDM is perpendicular to the molecular axis. This circumstance is what sparked my interest to study the MgH^+ molecule which has been extensively researched by

several works of experimental focus [76–83]. Another interesting feature of MgH^+ is the fact that it possesses permanent dipole moments which is a significant difference compared to the systems I have considered up to this point.

My aim is to reveal the effects of the laser induced nonadiabatic dynamics from the point of view of the direction of the TDM relative to the molecular axis. This is expected to be trackable in the angular distributions of the photofragments first and foremost.

In what follows I present the most important aspects from the point of view of the numerical simulations – carried out in MCTDH – and then I discuss my results.

4.1 Hamiltonian of MgH^+

In the calculations two electronic states, $^1\Sigma^+$ and $^1\Pi$ are considered. The TDM coupling these two states is perpendicular to the permanent dipoles of the system. The Hamiltonian reads

$$\begin{aligned}\hat{H}_{2D} &= \hat{T} + \hat{V} + \hat{V}_{\text{int}} = \\ &= \begin{pmatrix} -\frac{1}{2M_r}\frac{\partial^2}{\partial R^2} + \frac{1}{2M_r R^2}L_\theta^2 & 0 \\ 0 & -\frac{1}{2M_r}\frac{\partial^2}{\partial R^2} + \frac{1}{2M_r R^2}L_\theta^2 \end{pmatrix} + \begin{pmatrix} V_{\Sigma_1} & 0 \\ 0 & V_{\Pi_1} \end{pmatrix} + \\ &- E_0 \cos(\omega_L t) \cdot \sin^2\left(\pi\frac{t}{T}\right) \cdot \Theta(T-t) \begin{pmatrix} \mu_{\Sigma_1}\cos\theta & \mu_{\Sigma_1\Pi_1}\sin\theta \\ \mu_{\Sigma_1\Pi_1}\sin\theta & \mu_{\Pi_1}\cos\theta \end{pmatrix}.\end{aligned} \tag{4.1.1}$$

The Hamiltonian takes into account both the vibrational degree of freedom R and the rotational degree of freedom θ, hence the $2D$ suffix in $\hat{H}_{2D}$.
The first term corresponds to the vibrational and rotational kinetic energy operators in which M_r and R denote the reduced mass and the internuclear distance, respectively. L_θ is the angular momentum operator, θ is the angle between the polarisation of the laser field and the molecular axis.
The second term, $\hat{V}$ includes the potential energies, V_{Σ_1} in conjunction with the Σ_1 electronic state, and similarly, V_{Π_1} corresponds to the Π_1 state.
The final term $\hat{V}_{\text{int}}$ accounts for the interaction between the molecule and the external field. Here, E_0 is the amplitude of the electric field and ω_L is its frequency. The $\sin^2$ factor is the envelope of the field where the parameter T controls the duration of the pulse and the Heaviside-function $\Theta(T-t)$ switches off the field for times $t > T$, while for times $-\infty < t < 0$ the field is assumed to be switched off. In the diagonal elements, μ_{Σ_1} and μ_{Π_1} stand for the permanent dipoles of the two electronic states. The off-diagonal terms couple the dynamics on the two states via the transition dipole moment denoted by $\mu_{\Sigma_1\Pi_1}$. Figure 4.1 depicts these quantities. Note that in order to allow for the clear assessment of the role of the direction of the $\mu_{\Sigma_1\Pi_1}$ TDM, only the electronic properties relevant to the included Σ_1 and Π_1 states are built into the simulations.

The quantities shown in Figure 4.1 were acquired with the aid of the MOLPRO package. In order to get them, MRCI calculations were based on preceding CASSCF computations averaged over the four lowest

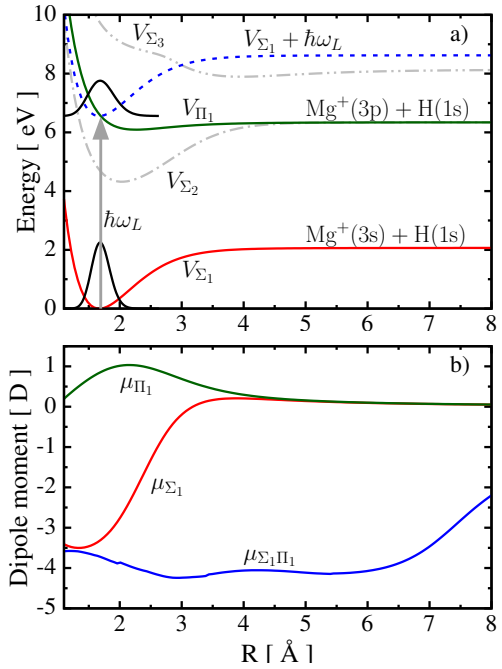

Figure 4.1: *Potential energies and dipole moments of the* MgH^+ *molecule.*
a) The V_{Σ_1} and V_{Π_1} states included in the actual dynamical simulations described by the Hamiltonian in eq. (4.1.1). Additionally, two other states, V_{Σ_2} and V_{Σ_3} were also calculated, but left out from the dynamics. These are represented with the dashed-dotted grey lines. A laser with frequency ω_L initiates population transfer from the ground state to the excited state, schematically portrayed by a vertical arrow.
b) A plot of the permanent dipole moments of the two states (μ_{Σ_1} and μ_{Π_1}) and the transition dipole moment $\mu_{\Sigma_1\Pi_1}$ that couples them.

lying states. During both of these computational steps aug-cc-pVQZ basis was used. In the individual irreducible representations of the relevant $C_{2\nu}$ point group $(A_1, B_1, B_2, A_2) = (3, 1, 1, 0)$ closed-shell orbitals and $(A_1, B_1, B_2, A_2) = (10, 4, 1, 0)$ occupied orbitals were utilised throughout the electronic structure calculations. By using the above parameters, the electronic properties showed good agreement with previous studies of the MgH^+ molecule [79].
The TDM between the Σ_1 and Π_1 states is perpendicular to the permanent dipole of the system. In what follows, the notations "*real system*" or "*perpendicular TDM*" correspond to this situation.
In order to study the impact of the direction of the TDM relative to the direction of the permanent dipole, I prepared a "model system" as well. In the model case, I rotated the TDM artificially such that it became parallel to the permanent dipole. For this system, the first two terms $\hat{T}$ and $\hat{V}$ remain the same in the Hamiltonian. In the third term $\hat{V}_{\text{int}}$, the $\sin\theta$ terms are replaced with $\cos\theta$ in the off-diagonals. I refer to the results of these simulations as "*model system*" or "*parallel TDM*".

In addition, I also carried out comparisons to 1D calculations in which the rotational kinetic energy operator is left out from the Hamiltonian

$\hat{H}_{2\mathrm{D}}$. In this case the angle θ only plays the role of a parameter in the Hamiltonian and averaging over several different values of it are performed. How differently the system behaves in the absence of dynamical rotation with respect to the dissociation dynamics, in particular when it comes to the angular distribution of the photofragments, is discussed later on.

Although all the results were obtained by utilising the full time-dependent Hamiltonian, considering the form the Hamiltonian assumes in Floquet picture is useful for the interpretations of the results. For even more simplicity, the effect of the permanent dipoles may be neglected as they average to zero [84] if the frequency of the employed field is high enough – as it is in my case. This applies to my simulations, thus the permanent dipoles may be neglected in $\hat{H}_{1\mathrm{D}/2\mathrm{D}}$. Following the RWA approximation [85] yields the adiabatic Floquet Hamiltonian

$$\hat{H}^F_{2\mathrm{D}} = \begin{pmatrix} -\frac{1}{2M_r}\frac{\partial^2}{\partial R^2} + \frac{1}{2M_r R^2}L^2_\theta & 0 \\ 0 & -\frac{1}{2M_r}\frac{\partial^2}{\partial R^2} + \frac{1}{2M_r R^2}L^2_\theta \end{pmatrix} + \\ + \begin{pmatrix} V_{\Sigma_1} + \hbar\omega_L & 0 \\ 0 & V_{\Pi_1} \end{pmatrix} - E_0 \sin^2\left(\pi\frac{t}{T}\right) \cdot \begin{pmatrix} 0 & \frac{\mu_{\Sigma_1\Pi_1}\sin\theta}{2} \\ \frac{\mu_{\Sigma_1\Pi_1}\sin\theta}{2} & 0 \end{pmatrix}. \tag{4.1.2}$$

For a crossing to be formed between the adiabatic upper and lower surfaces – determined upon diagonalisation of $\hat{H}^F_{2\mathrm{D}}$ –, similar considerations follow as discussed in Section 3.1. In both the real and model systems, the condition for the internuclear distance remains the same determined by the equation,

$$\hbar\omega_L = V_{\Pi_1}(R) - V_{\Sigma_1}(R) \tag{4.1.3}$$

but the angular requirement differs

$$\sin\theta = 0 \quad \Rightarrow \quad \theta = 0, \pi \quad \text{for perpendicular TDM;} \tag{4.1.4}$$

$$\cos\theta = 0 \quad \Rightarrow \quad \theta = \pi/2 \quad \text{for parallel TDM.} \tag{4.1.5}$$

Due to this, the LICI emerges at different positions of the configuration space depending on the direction of the TDM. The adiabatic surfaces of the real system are shown in Figure 4.2. Since LICIs are important sources of strong nonadiabatic effects, the differing positions at which they are formed are expected to leave their trace on observables susceptible to the molecular orientation θ. As a candidate for such a quantity I chose the angular distribution of the photofragments.

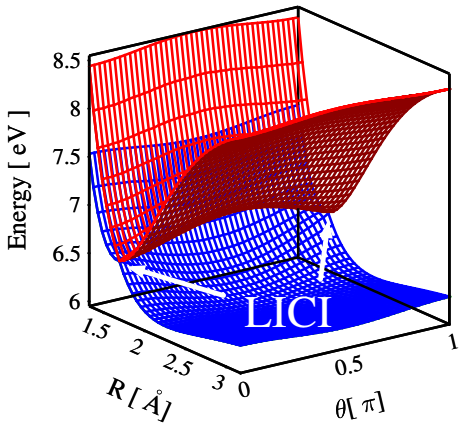

Figure 4.2: The adiabatic surfaces obtained for the perpendicular TDM situation. The crossing of the lower and upper surfaces takes places at $\theta = 0$ and $\theta = \pi$ angular orientations as required by the condition eq. (4.1.4).

Additionally, since the LICI condition requires two independent dynamical variables to be present, the 1D and 2D calculations are expected to show significant differences not only in the angular distributions, but in the case of simpler physical quantities as well. The simplest of those might be the population transferred to the excited state which can be significantly enhanced by the strong nonadiabaticity near the LICI.

4.2 Parameters

The time-dependent Schrödinger equation was solved with MCTDH. The vibrational degree of freedom is defined on a sin-DVR grid and N_R basis elements were utilised and distributed along the grid of internuclear separation from 2 au to 40 au.
The rotational degree of freedom θ is characterised by the Legendre polynomials $P_l^m(\cos\theta)$ with $m = 0$ the magnetic quantum number and $l = 0, 1, \ldots, N_\theta - 1$, where N_θ is the number of basis functions used in the representation.
Following the usual representation of MCTDH wave functions given in eq. (1.4.1) for two degrees of freedom, the single particle functions $\varphi_{j_Q}^{(Q)}$ are formed as

$$\varphi_{j_Q}^{(Q)}(Q,t) = \sum_{i_Q=1}^{N_Q} c_{j_Q,i_Q}^{(Q)}(t)\chi_{i_Q}^{(Q)}(Q) \quad \text{with} \quad Q = R,\ \theta \tag{4.2.1}$$

and the total nuclear wavepacket is given by

$$\Psi(R,\theta,t) = \sum_{j_R=1}^{n_R} \sum_{j_\theta=1}^{n_\theta} A_{j_R j_\theta}(t) \varphi_{j_R}^{(R)}(R,t) \varphi_{j_\theta}^{(\theta)}(\theta,t). \tag{4.2.2}$$

In the systematic calculations $N_R = 1024$ basis functions for the vibrational degree of freedom proved to be sufficient for all peak intensities studied in the range of $I_0 = 10^{12}$ – 10^{13}W/cm^2. As for the number of basis functions N_θ, different values were needed depending on the intensity I_0. At the lowest intensity $N_\theta = 61$, while at the highest $N_\theta = 301$ functions were used. Regarding the number of SPFs, it had to be varied depending on both the intensity and electronic state. For $I_0 = 10^{11}$W/cm^2 $n_R = n_\theta = 10$ SPFs were employed for both Σ_1 and Π_1, while at 10^{13}W/cm^2 the adequate description of the dynamics in Π_1 required $n_R = n_\theta = 13$ SPFs with the number of functions for Σ_1 unchanged.
Pulse duration of $T = 80$ fs and photon energy $\hbar\omega_L = 6.56$ eV were chosen in the simulations.

CAPs – eq. (2.3.2) – have been placed at the last 10 atomic units of the grids. The defining parameters are given by

$$\eta = 3.81 \cdot 10^{-5} \text{ au} \quad R_0 = 30 \text{ au} \quad b = 3. \tag{4.2.3}$$

4.3 Angular distribution

The initial wave function is taken as the lowest vibrational and rotational eigenstate of the Σ_1 state from which the laser pulse excites population to the initially unpopulated Π_1 state. During the propagation, the nuclear wavepacket reaching the end of the grid associated to the vibrational degree of freedom R gets absorbed by the respective CAPs $-iW$ employed for each state. To get the angular distribution, the integral

$$P(\theta_j) = \frac{1}{w_j} \int_0^\infty \langle \psi(R,\theta,t) | W_{\theta_j} | \psi(R,\theta,t) \rangle \, dt, \tag{4.3.1}$$

is determined. In the expression of $P(\theta_j)$ w_j is a weight factor corresponding to the relevant grid point in the applied sin-DVR and $-iW_{\theta_j}$ corresponds to the projection of W to a specific grid point associated with the rotational degree of freedom θ.
There are results available for the case of parallel TDM in the literature (see [74] for example). My intent is to discuss the situation of a perpendicular TDM while also comparing it to the results of simulations with parallel TDM. These are shown in Figure 4.3, providing extensive comparisons of the 1D-2D and perpendicular-parallel TDM cases.

At the lowest intensity the parallel TDM case does not show significant differences between the 1D and 2D calculations, they are essentially the same. The same does not hold for the real system, however. For orientations $\theta > \pi/8$ the 1D and 2D curves possess similar behaviour. As the molecule is being rotated closer and closer towards the orientation parallel to the field, the 2D results have a non-vanishing part in the dissociation yield, practically reaching a constant value. This observation is in strong contrast with the 1D results, where there is a monotonous decrease with $\theta \leq \pi/8$ and the yield finally vanishes at the $\theta = 0$ parallel orientation. Increasing the intensity to 10^{13} W/cm^2 now reveals drastic changes in the character of the 2D results. Firstly, a bumpy structure with local maxima and minima appear, the most significant of the latter ones occurring at around $\theta \approx \pi/8$. Still, the most striking difference is the monotonous decrease between $0 \leq \theta < \pi/8$ with the global maximum taking place at $\theta = 0$. This is especially interesting in the light of the fact that the coupling between the Σ_1 and Π_1 states vanishes for this particular orientation. The results of the 1D case are unable to account for this behaviour and still give no dissociation at $\theta = 0$. Albeit the 1D calculations do give increased dissociation yields upon increasing the intensity, the qualitative character of the two 1D curves are rather similar.

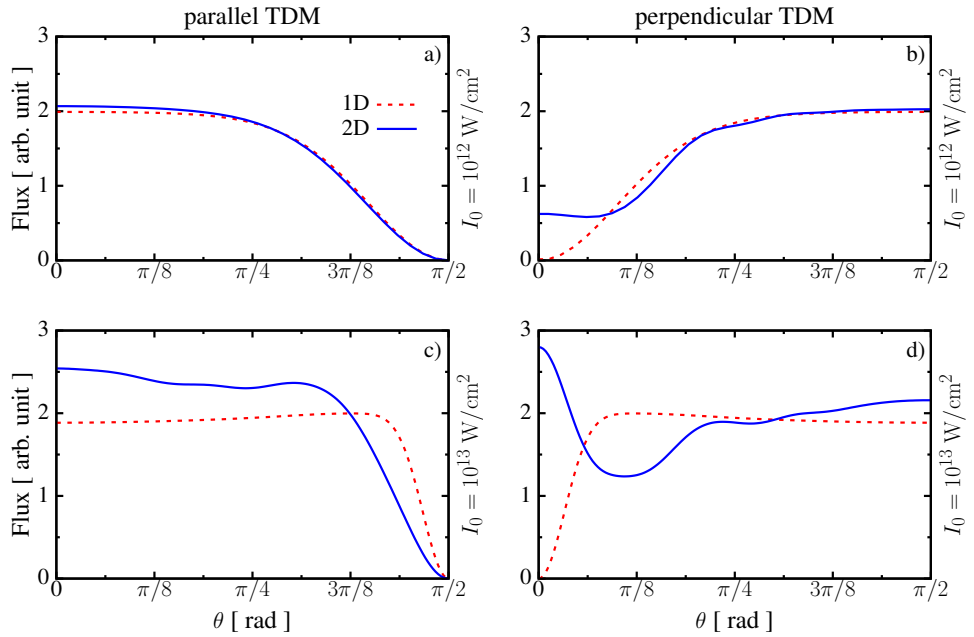

Figure 4.3: *Photofragment distributions resulting from dissociation on the* Π_1 *state.* [86]
The curves show the angular distributions compared for different simulation frameworks: 1D and 2D calculations (dashed red and solid blue lines, respectively); model – panels **a)**, **c)** – and real systems – panels **b)**, **d)** – for two different intensities (marked at the right axis of each subfigure).

As for the parallel TDM case at $I_0 = 10^{13}$ W/cm^2, the 1D result is practically the same as for the real system, the two being almost flawless mirror images of one other taken along $\theta = \pi/4$. As for the 2D curve, it displays a bumpy structure just as its counterpart in the real system, but it differs from the latter in the sense that it still agrees with the 1D result at $\theta = \pi/2$, predicting no dissociation for this orientation.

Additional information on how the dissociation process goes can be gained by taking snapshots of the nuclear density. The total density can be calculated as the sum of the densities on the Σ_1 and Π_1 states, $|\Psi(R,\theta,t)|^2 = |\Psi_{\Sigma_1}(R,\theta,t)|^2 + |\Psi_{\Pi_1}(R,\theta,t)|^2$. This is plotted in Figure 4.4 for the highest intensity applied, $I_0 = 10^{13}$ W/cm^2, and several time instances.

The snapshots of the evolution of density makes it possible to track how the dissociation develops as it provides supplementary information to those shown in Figure 4.3. The initially uniform density is significantly distorted by $t = 20$ fs and as the laser pulse gradually gets stronger – controlled by its envelope function $f(t)$ – the effect of the LICI gets

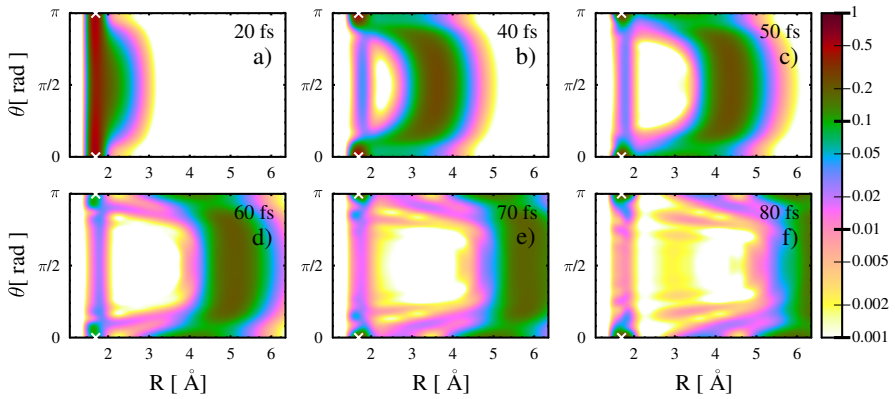

Figure 4.4: *Total nuclear density for the real system (perpendicular TDM) obtained from 2D calculations* [86].
For easier visualisation of the effect of the LICI, results with the highest instantaneous intensity, 10^{13} W/cm^2 are taken. The white crosses denote the positions of the LICI. Note the formation of peaks in the density in the vicinity of the crosses as the driving field gets stronger.

more emphasised. Local peaks start to develop in the configuration space at $R \sim 1.69$ Å and angular orientations $\theta = 0$ and $\theta = \pi$ in accordance with the LICI condition. The non-adiabatic couplings are the strongest in these regions of the configuration space. Moreover, the upper adiabatic surface possesses local minima at these positions, as it is shown in Figure 4.2. The molecule is gradually rotated towards the polarisation direction of the laser field, thus the peaks in the density appear at these locations. However, due to the crossings between the lower and upper adiabatic surfaces, parts of the wavepacket can travel through these crossings and reach the lower adiabatic surface. On this surface they can dissociate much easier than on the upper surface. This explanation is also in agreement with panel **d)** of Figure 4.3 that clearly shows the significantly increased dissociation yield from these angular orientations compared to the 1D results.

4.4 Conclusions

In this section I presented my results for the MgH^+ molecule. My study was tailored for revealing differences in the angular distribution of photofragments in two systems where the direction of the transition dipole moment is either perpendicular (real system) or parallel (model system) to the molecular axis of the system. Besides being susceptible to the angular orientation, this quantity is also of interest in experimental

setups and practical applications.
In addition to the above, I also carried out simulations in 1D and 2D and compared them.

I found significant differences between the 1D and 2D calculations that got more pronounced as the intensity of the laser field increased. The results can be explained by employing the light-induced picture and then considering the LICI that gets formed between the two light-induced/adiabatic surfaces.

The change in the character of the angular distribution is clearly driven by the strong non-adiabatic phenomena attributed to the LICI and it also leaves its mark on how the nuclear density evolves. These observations support the impact of the LICI on the dissociation dynamics.

Chapter 5

Two- and three-state simulations of the LiF molecule

Alkali halide molecules have a segment of remarkable size in the scientific literature, interest in the study of their physical properties have always motivated researches. Several works have dealt with photodissociation dynamics of these systems [87–91] and in other cases applications to track ionic-covalent transitions of alkali metals have seen widespread adaptation as well. There are also comprehensive reviews of metal halides with their most important properties of physical interest available [92].

In addition to being unique in several of its molecular properties with respect to other alkali metals, LiF has practical applications, too, such as in LiF based films that have been used as high resolution electron beam resists [93] or LiF-based imaging detectors [94].

For means of basic research, researchers dealing with electronic structure calculations have carefully studied the avoided crossing (AC) between the two lowest lying Σ states of LiF [95]. This AC gives rise to rich nonadiabatic phenomena, enhanced energy transfer between the electrons and nuclei, allowing for very fast decay of the excited states and dissociation taking place in the ground Σ state of LiF. Accordingly, as the proper tools became available and made the calculations of electronic properties approachable, the first dynamical simulations of LiF were carried out as well [96, 97].

The presence of the avoided crossing and the induced nonadiabatic dynamics it is responsible for makes LiF especially interesting because it is inherent to its electronic structure, unlike the previous systems I studied: neither D_2^+ nor MgH^+ possess such built-in source of nonadi-

abaticity. This is especially intriguing in the 2D calculations where, in addition to the AC, LICI can be formed as well, making the nonadiabatic dynamics more rich. In fact, the competition between LICIs, ACs and even LIACs have already inspired detailed discussions for NaI in [98].

Recently, successful confinement of the nuclear wavepacket with the help of external permanent field has been reported in the theoretical work [99]. In this study, the field-free potentials are modified by the external field that is taken to be the superposition of a purely sinusoidal driving field and a pump field, the latter initiating the dynamics by exchanging population between the ground and excited states. Due to this, the net potential oscillates in time as well and so does the crossing between the light induced potentials. In this setup, the authors described a formation of surprisingly long lived states in the upper light induced potential leading to drastically longer dissociation process. How effective this confinement of parts of the excited wavepacket is depends on the frequency and intensity of the applied driving field. It is interesting to note that the authors of [98] also found similar confinement effect to that of [99] in 1D and they also observed enhanced dissociation rates in the 2D simulations, making their results first among those discussing similar phenomena from the point of view of the competition between inherent and induced sources of non-adiabaticity.

Although large numbers of studies are available with LiF, several works have consistently disregarded the $1^1\Pi$ electronic state despite accounting for several Σ states lying even higher than the mentioned Π state. With my contribution to the dynamical simulations of LiF, my ambition was to shine light on influence of this electronic state.

On the other hand, as it was pointed out in the article [99], their findings presented on the confinement only apply to the results of 1D simulations where the polarisation direction of the field was always assumed to be parallel to the molecular axis, therefore no rotation was included in the simulations. How effective the confinement proves to be with vibrating-rotating LiF is an interesting question and partly this is what motivated the dynamical simulations with LiF in [100].

My main contribution to the LiF simulations resided in the electronic structure calculations that supplied the quantities needed to construct the Hamiltonian of LiF accounting for three electronic states. In what follows I present the results of these calculations and also include a selected portion of the dynamical studies of LiF with emphasise on what I personally found the most interesting out of these results.

5.1 Three-state electronic structure of LiF

In the proper dynamical simulations either two or three electronic states are included. In the case of three states, $1^1\Sigma^+$, $2^1\Sigma^+$ and $1^1\Pi$ are considered. For two state-calculations, following [99], only $1^1\Sigma^+$ and $2^1\Sigma^+$ are taken into account. In the following discussion they are referred to as Σ_1, Σ_2 and Π_1 in similar vein to the notation used for MgH^+.
The 2D and three-state Hamiltonian reads

$$\begin{aligned}\hat{H} &= \hat{T} + \hat{V} + \hat{V}_{\text{int}} = \\ &= \left(-\frac{1}{2M_r}\frac{\partial^2}{\partial R^2} + \frac{1}{2M_r R^2}L_\theta^2\right)\cdot \mathbf{1} + \begin{pmatrix} V_{\Sigma_1} & 0 & K \\ 0 & V_{\Pi_1} & 0 \\ -K & 0 & V_{\Sigma_2} \end{pmatrix} + \\ &- E(t)\cdot \begin{pmatrix} \mu_{\Sigma_1} & \mu_{\Sigma_1\Pi_1} & \mu_{\Sigma_1\Sigma_2} \\ \mu_{\Sigma_1\Pi_1} & \mu_{\Pi_1} & \mu_{\Pi_1\Sigma_2} \\ \mu_{\Sigma_1\Sigma_2} & \mu_{\Pi_1\Sigma_2} & \mu_{\Sigma_2} \end{pmatrix}.\end{aligned} \tag{5.1.1}$$

The first term of eq. (5.1.1) follows the same notations and has the same meaning as the first term of the Hamiltonian eq. (4.1.1) for MgH^+, $\mathbf{1}$ is the 3×3 unit matrix. The second one contains the potential energies and an additional term K as well, not needed in my previous dynamical simulations. $K(R)$ is called the non-adiabatic coupling. Its presence in the Hamiltonian accounts for the avoided crossing between the Σ_1 and Σ_2 states. K is defined as

$$K(R) = \frac{1}{2M_r}\Big(2\tau(R)\frac{\partial}{\partial R} + \tau^{(2)}(R)\Big), \tag{5.1.2}$$

with τ and $\tau^{(2)}$ denoting the NACT and second order NACT, respectively. The above analytical form is taken from [2] and τ is determined by evaluating the overlap integral

$$\tau(R) = \langle \varphi_{\Sigma_1} | \frac{\partial}{\partial R} \varphi_{\Sigma_2} \rangle \,, \tag{5.1.3}$$

where φ_{Σ_1} and φ_{Σ_2} are the respective electronic wave functions. However, instead of using the exact form eq. (5.1.2), a simpler and approximated expression is employed borrowed from [101] and it reads

$$K(R) \approx \frac{1}{2M_r}\Big(2\tau(R)\frac{\partial}{\partial R} + \frac{\partial}{\partial R}\tau(R)\Big). \tag{5.1.4}$$

This is the expression built into the Hamiltonian eq. (5.1.1).
The interaction between the external field $E(t)$ and the dipoles is accounted for in $\hat{V}_{\text{int}}$. Here, the electric field is taken in the form of

$$\begin{aligned} E(t) = E_0 \cos^2(1.14372 \cdot (t - t_0)/\tau_L) \cdot \cos(\omega_L(t - t_0)) + \\ + E_d f_d(t) \cos(\omega_d t) \end{aligned} \tag{5.1.5}$$

with the choice $t_0 = 0$ and τ_L controlling the width of the intensity profile of the pump pulse, taken as $\tau_L = 20$ fs. The envelope $f_d(t)$ of the driving field is 1 at all times, except for a time period of 500 fs before the pumping laser pulse. During this window, $f_d(t)$ linearly increases to its final value of 1. In the article [100] several different pump and driving intensities – denoted by I_0 and I_d, respectively – are considered coupled with different photon energies $\hbar\omega_L$ and $\hbar\omega_d$.

Figure 5.1 presents the electronic properties calculated with MOLPRO. Regarding the determination of these quantities, MRCI method was utilised that made use of previous CASSCF calculations. In both the CASSCF and MRCI steps, aug-cc-pVQZ bases were applied. As for the number of active molecular orbitals in the A_1, B_1, B_2 and A_2 irreducible representations of the $C_{2\nu}$ group, these are taken as $(A_1, B_1, B_2, A_2) = (5, 3, 3, 1)$. The number of active electrons in these representations are $(n_{A_1}, n_{B_1}, n_{B_2}, n_{A_2}) = (2, 2, 2, 0)$. Setting up the MOLPRO calculations with the above choice of parameters granted good agreement with previous results available in [102, 103].

The energy of the Π_1 excited state lies very close to that of the Σ_2 state (subfigure **A**). Thus, energies allowing excitation from Σ_1 to Σ_2 are also capable of transferring some of the population to the Π_1 state. This path of excitation is even more possible when the initialisation of the nuclear dynamics and the subsequent excitation takes place in the Franck-Condon region. In this domain the $\mu_{\Sigma_1\Pi_1}$ TDM exceeds both $\mu_{\Sigma_1\Sigma_2}$ and $\mu_{\Pi_1\Sigma_2}$ (subfigure **C**). Following these arguments, upon the inclusion of the Π_1 state a smaller amount of population is expected to be excited to Σ_2 compared to setups in which Π_1 is left out and only the two lowest lying Σ states are considered.

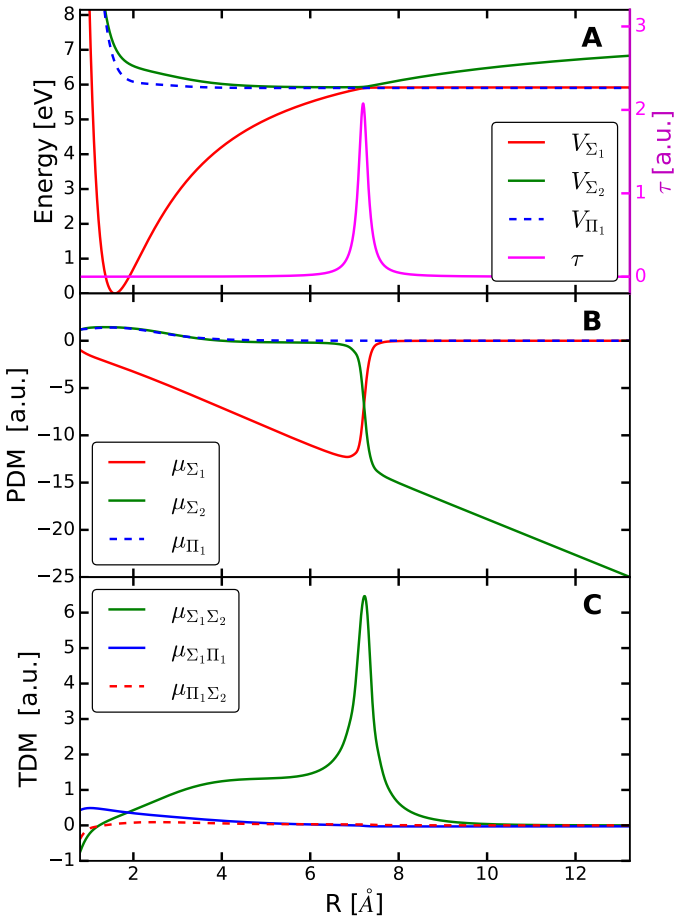

Figure 5.1: *Electronic properties of LiF with three electronic states accounted for.* Subfigure **A** shows the potential energies of the three states (values displayed on the left-hand axis). The nonadiabatic coupling term is also presented and scaled on the right-hand axis colored in magenta. This latter curve, as expected, possesses a rather steep increase in the vicinity of the AC region with its maximum at the AC, located at around ≈ 7.2 Å. The dipole moments are plotted in subfigures **B** and **C**, showing the permanent and transition dipoles, respectively. Especially interesting is the behaviour of the TDMs in the Franck-Condon region where $\mu_{\Sigma_1\Pi_1}$ surpasses the $\mu_{\Sigma_1\Sigma_2}$ TDM significantly.

5.2 Electronic state populations and confinement

To track the confinement of the nuclear wavepacket the electronic populations $P_i(t)$ are determined. This is given by the integrals

$$P_i(t) = \langle \Psi_i(R,\theta,t) | \Psi_i(R,\theta,t) \rangle = \int_0^{\pi} \sin\theta \cdot d\theta \int_0^{\infty} \Psi_i^*(R,\theta,t) \Psi_i(R,\theta,t) \cdot dR \tag{5.2.1}$$

with $i = \Sigma_1, \Sigma_2$ or Π_1 and the dissociation can be calculated in the same vein as described before for the previous systems. In the corresponding calculations, a CAP with parameters $\eta = 3.97 \cdot 10^{-4}$, $b = 3$ and 10 au in length was used.

Upon starting the propagation from the lowest vibrational-rotational state of Σ_1, the population is transferred either to Σ_2 exclusively or to both Σ_2 and Π_1 (second and first columns of Figure 5.2, respectively).

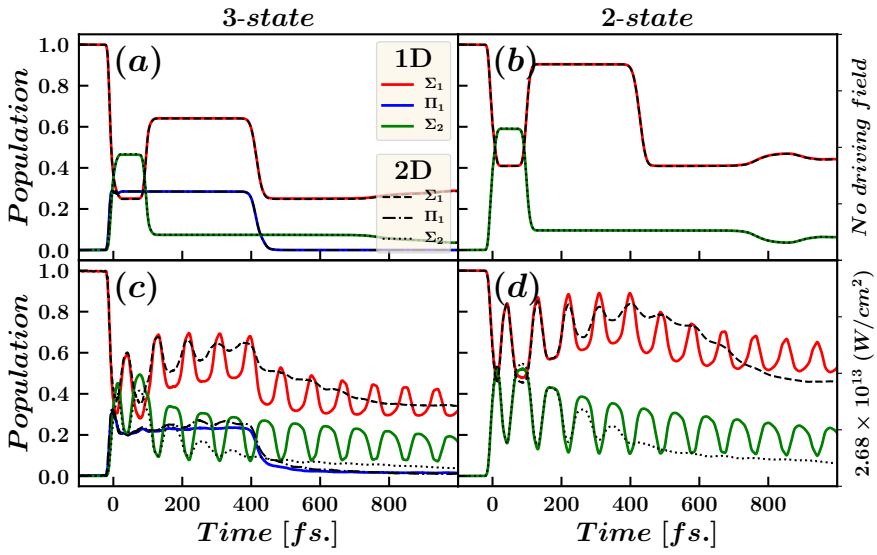

Figure 5.2: *Two- and three-state populations in the absence or presence of a driving field.*
A pump field of intensity $I_0 = 4.8 \times 10^{13}$ W/cm^2 and of energy $\hbar\omega_L = 6.94$ eV is employed to initiate the population dynamics. Then the effect of a driving field of intensity $I_d = 2.68 \times 10^{13}$ W/cm^2 – subplots **(c)-(d)** – is compared to the case when there is no driving field at all ($I_d = 0$, subplots **(a)-(b)**). The photon energy of the driving is kept constant, chosen to be $\hbar\omega_d = 3.995$ eV .
In addition to the 2- and 3-state comparisons, the 1D – solid lines – and 2D – broken/dotted lines – results are contrasted, as well. Interpretation of these findings can be found in the text below.

The simplest case of the dissociation dynamics occurs when there is no driving field present, so $I_d = 0$. In such a situation with three states included, the excited population can access two channels for dissociation; a direct one which means dissociation in the Π_1 state and an indirect one that happens in Σ_1 (note the flat character of Σ_1 beyond the AC region). However, for this latter channel to be activated the wavepacket needs to be taken first to Σ_2 and then it has to travel through the avoided crossing at ≈ 7.2 Å. In the vicinity of the AC, both the $\mu_{\Sigma_1\Sigma_2}$ TDM and the NACT between Σ_1 and Σ_2 increase steeply as seen in subplot **C** of Figure 5.1. Thus, even with short pumping pulses used and in the absence of a driving field, due to the NACT, population can be transferred back to the Σ_1 state as the wavepacket reaches the region of the AC, leading to

subsequent dissociation in Σ_1. However, this conversion of the excited population in Σ_2 back to Σ_1 through the AC happens in several steps. Only some parts of the wavepacket that reach the AC region is transferred back to Σ_1, while other parts are reflected and get trapped in Σ_2 for at least another cycle of oscillation; the cycle it takes the wavepacket to get back to the Franck-Condon region and then back to the AC region again. This cycle can take up to several hundred femtoseconds. Obviously, taking this pathway is expected to be slower than the direct path on Π_1. Therefore, the inclusion of the Π_1 state can enhance the rate of dissociation and results in a faster decay of the excited population.

On the other hand, the direct channel is not available in the 2-state calculations because only Σ_1 and Σ_2 are taken into account. Due to this, one can expect longer dissociation times in the 2-state case.

The above arguments are confirmed in panels **(a)** and **(b)** of Figure 5.2 which show significantly larger occupation of the Σ_1 and Σ_2 states still present at the end of the time window (1000 fs) when only the two Σ states are considered. In this case, population amounting to about half the initial population remains in the system. On the other hand, in the same time window less than half the initial population is retained in the system when all three states are considered. This is clearly due to the effect of the Π_1 state as described above. During the initial population transfer this state obtains a large amount of the total excited population and provides a more efficient pathway to dissociation. As for the comparison of the 1D and 2D results, no differences can be observed at the applied intensity $I_0 = 4.8 \times 10^{13}$ W/cm^2 of the pumping field.

Keeping the pumping parameters fixed and moving on to the calculations with driving field present, results corresponding to intensity $I_d = 2.68 \times 10^{13}$ W/cm^2 are showcased in the second row of Figure 5.2.

The two-state results of subfigure **(d)** show a similar oscillatory behaviour in 1D and 2D right until $t \approx 200$ fs . Propagating beyond this time instant yields gradually suppressed oscillations in 2D and a smooth decrease in the populations sets in later on. However, the oscillations, meaning population transfer back and forth between Σ_1 and Σ_2, are always persistent in 1D. The relatively shallow decrease of the envelope, that could be fitted on top of these oscillations in 1D, tells of a rather slow leak through the avoided crossing into the CAP region of Σ_1 where the population is annihilated finally. Therefore, even without the inclusion of the Π_1 state, which is proven to be a faster decay channel, accounting for the rotation of the molecule and including it in the dynamical description leads to hindered confinement efficiency on its own.

When all states are regarded (panel **(c)**), the state occupations show

significant changes. By $t = 1000$ fs, about half the population is conserved in 1D and only ≈ 0.35 in 2D. This is in stark contrast with the 2-state results for which populations amounting to ≈ 0.8 (1D) and ≈ 0.55 (2D) are retained.

The findings of Figure 5.2 can be presented in a more sufficient format that is able to capture more clearly how efficient the containment is. To this end, a ratio of the total population left unexcited to the total population present in the system can be introduced. Following [99], this is given by

$$r(t) = \frac{P(t) - (1 - P_{\text{ex}})}{P_{\text{ex}}}, \tag{5.2.2}$$

with $P(t)$ the total population remaining in the system. According to eq. (5.2.1), this is the sum of the individual electronic state populations, $P(t) = P_{\Sigma_1}(t) + P_{\Sigma_2}(t) \equiv P_{\Sigma}(t)$ for two-states and $P_{\Sigma}(t) + P_{\Pi_1}(t)$ for three-states. P_{ex} denotes the maximum of the instantaneous population that gets excited by the pumping field during the propagation. Then the difference $1 - P_{\text{ex}}$ accounts for the amount of population left unexcited. Thus, the numerator tracks the population still excited at time t and the ratio $r(t)$ keeps an account of that relative to the maximum amount converted to the excited states. At $t = 0$ $P(t)$ starts off at 1, so $r(t) = 1$. As the electronic states trade population it is up to the confinement to keep the population in the excited states.

However, if the containment breaks down and looses efficiency then more of the excited population may pass into the CAP region where they are absorbed subsequently. This causes $P(t)$ to decrease and $r(t)$ follows suit. How $r(t)$ evolves is shown in Figure 5.3. The displayed ratios are determined from the data presented in Figure 5.2.
As for the results in the absence of a driving field, the 1D and 2D cases (displayed in red in Figure 5.3) yield practically the same containment regardless of whether 2 or 3 electronic states are taken into account. However, by comparing the 2- and 3-state ratios, a faster decay of the excited population can be observed with 3 states included and it also gives lower asymptotic values at around ≈ 0.1, while the 2-state $r(t)$ is slightly below 0.2 by $t = 1000$ fs. Switching a driving field of intensity $I_d = 2.68 \times 10^{13}$ W/cm^2 on, the 1D simulations predict a significantly slower depletion of the excited population for 2-states than for 3-states. An interesting find presents itself in the 2D results of panels **(a)** and **(b)**, showing the 3- and 2-state yields, respectively. Here, the 2-state confinement seems to be of somewhat worse efficiency than with the Π_1 state included.

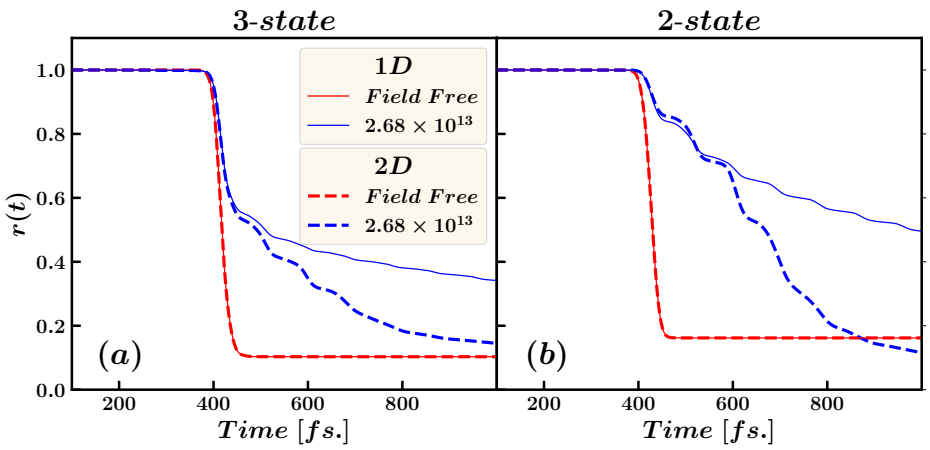

Figure 5.3: *Confinement ratio* $r(t)$.
$r(t)$ is based on the ratio of the instantaneous excited population to the all-time maximum of the excited population. It is an expressive quantity to describe how sustainable the excited population is in the long run.

5.3 Conclusions

The 2- and 3-state dynamical simulations on LiF reveal the important effect of the Π_1 electronic state on the dissociation dynamics, or equivalently, the efficiency of the confinement effect driven by a persistent electric field E_d. Its capability to significantly alter the dissociation directly ties in with the energetical position of this state relative to the Σ_2 state that is always included in the simulation.

Moreover, the comparatively large TDM corresponding to the $\Sigma_1 \rightarrow \Pi_1$ transition also allows for a non-negligible population transfer to this state. Thus the presence of Π_1 alters how the decay of the initially excited population proceeds, leaving its mark on the behaviour of the confinement ratio $r(t)$ as well.

Chapter 6

Summary

In this PhD dissertation I presented my studies of small molecular systems containing two atoms and discussed their non-adiabatic nuclear dynamics in presence of an external laser field that is responsible for initialisation of the dynamics.

The problem of tracking the nuclear dynamics always needed numerical solution of the time-dependent Schrödinger equation. To this end, I made use of the highly successful numerical package of MCTDH and prepared the appropriate calculations or wrote my own implementation to solve the problem at hand – as it was my approach in the case with the calculation of Berry's phase where I also made use of the freely available GSL package. On the other hand, no numerical simulation of the nuclear dynamics may be done without the proper description of the electronic structure of the molecule. In my case these quantities are the potential energies, the permanent and transition dipole moments and the non-adiabatic coupling between the electronic states. In some systems not all these are relevant or there are widely used and accepted forms available, such as it is the case for D_2^+. For those systems where these quantities are not readily available, I carried out the needed electronic structure calculations with the MOLPRO package.

My work has focused on laser induced nonadiabatic effects and I have studied several different phenomena that they can be responsible for. These included the following – given in the order they appear detailed in the main text –

- vibrational trapping effect studied in the D_2^+ system. This effect is interesting, because it can lead to significant suppression in the dissociation yield and thus effective molecular stabilisation can occur under appropriate conditions;

- the calculation of a non-trivial Berry's phase that ties in with the sign change of the adiabatic electronic eigenfunctions upon transportation along a closed path in the configuration space encompassing a degeneration;

- detailed discussion of how the direction of the transition dipole moment (TDM) relative to the molecular axis can affect the dissociation dynamics, focusing on experimental observables first and foremost

- electronic structure calculations of the LiF molecule that served as input to subsequent nuclear dynamical simulations. I also discussed a small portion of these latter results.

Vibrational trapping in D_2^+

I have carried out calculations in MCTDH and tracked the total amount populations that remained in the system by the end of the propagation. By doing so, I was able to determine the dissociation probability. Upon utilising laser fields of different wavelengths, several sharp minima appear in the dissociation probability. According to earlier publications and theory, the occurrence of such minima at particular wavelengths can be conveniently explained by considering the light-induced picture and that the upper light-induced adiabatic potential may possess states with vibrational energies lying very close to those of the diabatic vibrational eigenstate. Thus, the starting diabatic vibrational states can be trapped into upper adiabatic states effectively.

I studied the above explanation by employing a model potential to approximate the light-induced upper adiabatic potential that is reasonable for laser fields of relatively low intensity. Studying the differences of the diabatic and adiabatic eigenenergies, I observed discrepancies ranging from about 5% to about 15%.

When taking into account another relevant measure, namely the overlap of the diabatic and adiabatic eigenfunctions, the maxima of the overlaps as a function of the applied wavelengths is an adequate measure of how similar the eigenstates are. However, this quantity showed similar errors in predicting the correct wavelengths as the measure built on the energy differences did. Although the mentioned discrepancies are present, they still are in acceptable agreement with the original explanation, especially when the approximated form of the model potential is taken into account.

Motivated by the above errors in the prediction of the dissociation minima, a careful consideration of how the maxima of the overlaps and very close coincidence of the eigenenergies can occur revealed the importance of the nodal structure of the diabatic eigenstates. I calculated several different auxiliary quantities to put the node-based theory to the test and they proved to be more precise by a fair amount than the prediction based on the overlaps and energy differences. This is especially true for the first seven lower lying diabatic eigenstates. From the two node based quantities, further empirical expressions can be formed that are capable to forecast the dissociation minima with smaller than half a percent error in several cases.

Although how the particular form of the node-based expression can be explained from the physical point of view remains a task that still needs to be tackled, it also supplies motivation to me to pursue this study further in the future.

Berry's phase

There are several publications available on the adiabatic transportation of electronic eigenfunctions along a closed path in the molecular configuration space. If the closed path encircles a degeneracy upon adiabatically slow transportation, when the system has enough time to assume its eigenfunction, the wave function must change sign if it is required to be real valued. The acquired phase factor corresponding to this sign change is known as Berry's phase in the literature. It has been proven to be of purely geometrical nature as it is shown to depend only on the closed path taken in the configuration space. Whenever the path encircles a degeneracy such as a light-induced conical intersection (LICI) the phase is equal to π (or odd multiple of it), otherwise it is 0.

My intent was to calculate this phase by employing the original method of Berry, a time-dependent adiabatic approach. My choice of system was the D_2^+ molecule, chosen for its simplicity. Utilising the Floquet-picture and parameterising the dynamical variable R and θ the Hamiltonian depends on, I propagated the system adiabatically along closed ellipses of the (R, θ) configuration space. To do this, I implemented a C code, made with the help of the GNU Scientific Library (GSL), to numerically integrate the Schrödinger-equation.

Laser fields encompassing a wide range of intensity were used. How quickly the system is transported along the closed loop determined to what extent the adiabatic theorem is applicable and thus how adiabatic the propagation process is. At higher intensities slower and slower trans-

portation times T are required to warrant adiabaticity which, as expected, introduces growing numerical difficulties and longer computation times.

The acquired data are in very good agreement with the expectation, yielding values of the geometric phase close to π whenever the path enclosed the light-induced degeneration and close 0 in every other cases. This also held with several different paths prepared and traveled in the configuration space.

Direction of the transition dipole moment and its effect on the dynamics in MgH^+

The D_2^+ molecule differs from MgH^+ in several ways. While D_2^+ is simple enough from the point of view that it does not possess permanent dipole moment and its transition dipole moment is parallel to the molecular axis, MgH^+ differs from it in both of the above aspects: it does have permanent dipole moment that is parallel to the axis and transition dipole which is perpendicular to it.

The very first results corresponding to the direct effect of a LICI on the nuclear dynamics was obtained by careful analysis of the angular distributions of the photofragments when both the internuclear coordinate – R – and the rotation of the molecule – θ – are considered as individual dynamical variables of the molecule and included in the working Hamiltonian. How the conditions regarding the formation of a LICI are altered in a system with perpendicular TDM is interesting and it is expected to leave its mark on physical observable carrying information about the orientation of the molecule.

My aim with the dynamical study of MgH^+ was to go beyond previously available results and discuss the effect of direction of the TDM on the dynamics. In order to do so, I also studied an artificial system that has the very same properties as MgH^+, except for its TDM that is rotated parallel to the molecular axis.

I carried out both 1D and 2D simulations with both the real and model (artificial) systems and the results I got showed striking differences in the obtained angular distribution of the photofragments as it could be expected. These differences get more significant as the intensity of the external laser field is increased and it is attributed to the presence of LICI formed between the light-induced adiabatic surfaces.

By tracking how the total nuclear density evolves in time, regions in the configuration space of high nuclear density formed at exactly those

positions that the LICI conditions require.

According to my results, the impact of the direction of the TDM on the dissociation process is significant.

Electronic structure calculations with LiF and nuclear wavepacket confinement

The apropo of the dynamical studies on LiF is the findings of a recent article, where the authors observed effective confinement of the excited population when an external permanent electric field was applied to the environment of the molecule. According to the publication, a pump laser initiates population transfer between the ground state of LiF and its Σ_2 excited state and a continuous driving field alters the potential energy curves so that effective confinement in the excited states can occur.

However, the findings of such effective confinement was only discussed without the rotation of the molecule included in the dynamical description which circumstance was also pointed out by the authors themselves. Moreover, although the Σ_2 excited state is accounted for, an energetically lower lying state, the Π_1 state is left out from their simulations and this state may also play a role in the dissociation dynamics.

In order to study whether the confinement of the excited population is enhanced or hindered for vibrating-rotating LiF, I carried out preemptive electronic structure calculations of LiF, yielding the necessary data of the potential energies of three electronic states, their permanent dipole moments and the transition dipole moments between the three electronic states, subsequently serving as input to the nuclear dynamical simulations. These results are in good agreement with the results of previous publications.

Among the electronic properties of LiF, the most interesting is an avoided crossing (AC) between the Σ_1 and Σ_2 states and the nonadiabatic coupling it gives rise to. Due to its presence, LiF has the inherent possibility of interesting non-adiabatic phenomena occurring, naturally built into its electronic structure. How this interacts with the LICI formed in 2D is also an intriguing question that the nuclear dynamical calculations are to answer.

The findings of the simulations undoubtedly showed that the containment looses efficiency as the rotation of the molecule is considered regardless of whether the Π_1 state is included or not. On the other hand, by comparing 2-state results, when Π_1 is left out, and 3-state results where it is present, gave significant differences showing the importance

of this electronic state.

7. fejezet

Összefoglalás

Az alábbi Phd értekezésben ismertetem azon eredményeimet, melyeket kétatomos molekulákra végzett számításokból kaptam és tárgyalom az azokban megfigyelt, külső lézertér hatására bekövetkező nem-adiabatikus magdinamikai folyamatokat.

A magdinamikai folyamatok nyomonkövetéséhez minden esetben szükség volt arra, hogy az időfüggő Schrödinger-egyenletet numerikusan megoldjam. Ehhez jól bevált és magdinamika számolásokban széles körben sikeresen alkalmazott módszerként az MCTDH programot használtam.

Más esetben, mint ahogy az a Berry-fázis meghatározására vonatkozó szimulációkban is történt, saját implementációt is készítettem, amiben hasznosítottam a GNU Scientific Library (GSL) könyvtárban elérhető integrátorokat.

Habár ezek a megoldások alkalmasak a magdinamika propagálására, bizonyos esetekben megelőző számolásokra is szükség volt, amelyek a megfelelő rendszerhez szolgáltatták az elektronszerkezeti adatokat. Esetemben ezek a mennyiségek a potenciális energia görbék, a rendszer permanens és átmeneti dipólusmomentumai, illetve a nemadiabatikus csatolások az elektronállapotok között. Bizonyos rendszerekre, mint ahogy az a D_2^+ esetében is van, elérhetőek széles körben alkalmazott és elfogadott analitikus formulák ezekre a mennyiségekre, míg más rendszerekre nem. Ezen rendszerekre minden esetben megelőző elektronszerkezeti számolásokat végeztem el a MOLPRO programcsomag segítségével. A kapott eredményeim más publikációkban fellelhető eredményekkel jó egyezést mutattak és a továbbiakban ezek beépítésre kerültek a magdinamikai szimulációkba.

Munkám lézer indukálta nemadiabatikus folyamatok vizsgálatára fókuszált és több idetartozó jelenséget érintett. Ezek az alábbiak:

- vibrációs csapdázódás vizsgálata D_2^+ rendszerben. Az effektus ér-

dekessége abban rejlik, hogy a disszociációs folyamatot jelentősen elnyomhatja megfelelő körülmények között, így a molekula stabilitását növelni képes;

- Berry-fázis számolása, ami az adiabatikus elektron sajátállapotok előjelváltásával kapcsolatos, amint a rendszer időfejlődése a molekula konfigurációs terének egy olyan zárt görbéjét követi le, amely valamilyen degenerációt tartalmaz az elektronállapotok között, mint amilyen például a kónikus kereszteződés (természetes avagy indukált eredetű);

- annak vizsgálata miképpen befolyásolja az átmeneti dipólus momentum (TDM) molekulatengelyhez képesti iránya a disszociációs dinamikát, elsősorban olyan mennyiségekre koncentrálva, amelyek potenciálisan kísérletileg is mérhetőek;

- a LiF molekula elektronszerkezeti tulajdonságainak számolása, amelyek az ezt követő magdinamikai számolások bemeneteként szolgáltak a Hamilton operátor megkonstruálásához. Egy kis részét a kapott magdinamikai eredményeknek a teljesség kedvéért ismertetem.

Vibrációs csapdázódás D_2^+ rendszerben

Szimulációkat végeztem MCTDH segítségével és nyomon követtem az elekronállapotok populációinak változását. Meghatároztam a rendszerben a disszociáció befejeztével megmaradt populációt, ilyen módon disszociációs valószínűséget számítottam.

Rögzített intenzitású, de különböző hullámhosszú lézerterek alkalmazásakor számos éles minimum figyelhető meg a meghatározott disszociációs valószínűségben a hullámhossz függvényeként. Korábbi publikációkra alapozva, ezen éles minimumok a lézer-indukálta adiabatikus potenciálok segítségével értelmezhetők: amennyiben a tér által indukált fölső adiabatikus potenciálhoz tartozó vibrációs sajátállapotok valamelyike a térmentes, avagy diabatikus potenciál vibrációs sajátenergiájához közel eső energiával bír, akkor a kezdeti diabatikus sajátállapot, amelyből a dinamika indul, jobb hatásfokkal csapdázódhat be a fölső adiabatikus potenciálon.

A fent adott értelmezést volt célom vizsgálni a fölső adiabatikus potenciál viszonylag kis intenzitású lézertér (esetemben 10^{11} W/cm^2) alkalmazott közelítésével, amely a D_2^+ $2p\sigma_u$ állapotának fotonnal öltöztetett

alakjára és ennek az állapotnak az $1s\sigma_g$ állapottal való kereszteződési pozíciójára építkezett. Meghatározva a fenti modell potenciálhoz és az $1s\sigma_g$ alapállapothoz tartozó vibrációs sajátenergiákat, a disszociációs minimumpozíciók sajátenergiák különbségére alapozott becsült és valódi értéke között kb. 5%-tól 15%-ig terjedő eltéréseket tapasztaltam.

További releváns mennyiség, amit tekintettem, az adiabatikus és diabatikus sajátállapotok átfedési integrálja. Ezek maximuma a lézertér hullámhosszának függvényében szintén alkalmas lehet a disszociációs minimumpozíciók előrejelzésére, hiszen éppen az átfedési maximumoknál a legnagyobb a hasonlóság az adiabatikus és diabatikus vibrációs sajátfüggvények között. Az erre alapozott értékek a disszociációs minimum tekintetében a sajátenergiák alapján kapott eredményekhez hasonló pontatlanságot mutattak. Habár a fent említett pontatlanságok vitathatatlanul jelen vannak, az alkalmazott modellpotenciál alakjára tett közelítések fényében a kapott értékek nem túl rosszak.

Pontosabb előrejelzést tett lehetővé annak vizsgálata, hogy miképpen alakulhat ki jelentős átfedés a sajátállapotok között, illetve ennek kapcsolata a vibrációs sajátenergiákkal. Ez a megfontolás a diabatikus sajátfüggvények nóduspozícióinak szerepére világít rá. Ennek teszteléséhez további kiegészítő mennyiségeket számoltam, amelyek mindegyike a nódusszerkezetre alapoz. Ezen mennyiségek sokkal pontosabban képesek reprodukálni a disszociációs számolásokban kapott éles minimumok pozícióit, a hét legmélyebben fekvő diabatikus vibrációs állapot esetében pedig különösen nagy javulást hoznak a korábbiakhoz képest.

A meghatározott nódus alapú mennyiségekből további empirikus formulák segítségével kapott előrejelzések kevesebb, mint fél százalék eltéréssel képesek reprodukálni a megfigyelt minimumpozíciókat, ami újabb jelentős javulást jelent.

Habár a pontos fizikai magyarázata annak, miképpen adódik, hogy éppen a nódus alapú mennyiségek ezen empirikus kombinációi képesek a legnagyobb pontossággal visszaadni a disszociációs minimumokat egyelőre megoldatlan, azonban egyúttal motivációt is nyújt számomra, hogy ennek pontos magyarázatát a jövőben kidolgozzam.

Berry-fázis

Számos publikáció foglalkozik az irodalomban azzal, miképpen változnak meg az adiabatikus elektron sajátfüggvények, miközben a molekula konfigurációs terének egy zárt görbéjét követi le az időfejlődésük. Megmutatták, hogy amennyiben a zárt görbe közrefog egy degeneranciát a molekula konfigurációs terében, akkor adiabatikusan lassú, a zárt görbe

mentén történő ciklikus körbejárás folyamán a sajátfüggvény előjelet kell váltson, ha megköveteljük, hogy valós értékű legyen. Az ehhez kapcsolódó fázis faktor Berry-fázis néven ismert az irodalomban.

Bebizonyították azt is, hogy a Berry-fázis egy tisztán geometriai jellegű fázisfaktor, ami kizárólag a konfigurációs térben lekövetett zárt görbétől függ. Amennyiben a görbe degeneranciát fog közre, mint amilyen a lézerrel indukált kónikus kereszteződés (LICI) vagy a sokatomos, nagyméretű rendszerekben nagyszámban természetes körülmények között is jelenlévő kónikus kereszteződés (CI), akkor a Berry-fázis értéke π, illetve annak páratlan számú többszöröse, egyébként 0.

Célom az volt, hogy kiszámítsam a Berry-fázist Berry eredeti, időfüggő adiabatikus módszerét alkalmazva. A rendszer tekintetében a D_2^+-ra esett a választásom az egyszerűsége és az elektronszerkezeti tulajdonságaira elérhető analitikus kifejezések miatt.

A számolásaimban a Floquet-képet alkalmaztam a rendszer Hamilton-operátorában és a vibrációs koordináta (R) és a forgást jellemző dinamikai változó (θ) parametrizációjával a Hamilton operátor nem függ explicit módon az időtől. Az (R, θ) konfigurációs térben zárt ellipszisek mentén végeztem a propagációt. A Schrödinger-egyenlet numerikus megoldásához C nyelven kódot írtam, amelyben a GSL könyvtárban elérhető integrátorokat alkalmaztam.

Rögzített fotonenergiával, széles tartományban változtatott intenzitású lézer tereket alkalmaztam a szimulációkban. Azt, hogy mennyire tekinthető adiabatikusnak a zárt görbéket lekövető propagáció, elsősorban az alkalmazott intenzitás és a görbék mentén végzett adiabatikus transzport gyorsasága határozta meg. Magasabb intenzitások mellett lassab T körbejárási időre volt szükség, ahhoz hogy biztosított legyen az adiabatikusság, ezek viszont numerikus nehézségeket is okoznak bizonyos esetekben és sokkal hosszabb futási időket.

A szimulációs programmal nyert eredmények nagyon jó egyezésben vannak a várakozásokkal, közel π-t szolgáltatva azokban az esetekben, amikor a zárt görbe közrefogja a LICI pozícióját és közel 0-t minden más esetben. Ezek az eredmények konzisztensnek bizonyultak a különböző tesztelt zárt görbék mentén választott eltérő kezdőfeltételekkel is.

Az átmeneti dipól irányának hatása az MgH^+ rendszer dinamikájára

Az előzőekben vizsgált D_2^+ rendszertől az MgH^+ több szempontból is különbözik. Míg a D_2^+ kellően egyszerű rendszer, már csak abból a szem-

pontból is, hogy nem rendelkezik permanens dipólusmomentummal, továbbá az átmeneti dipólja párhuzamos a molekula tengelyével, az MgH^+ ezen szempontok mindegyikében különbözik: rendelkezik a molekulatengellyel párhuzamos permanens dipóllal és olyan átmeneti dipóllal is, amely viszont merőleges a tengelyre.

A LICI-k magdinamikára gyakorolt hatásának első közvetlen bizonyítékát a disszociációs fragmentumok szög szerinti eloszlásának tanulmányozása szolgáltatta azon vizsgálatokban, amikor mind a vibrációs koordináta (R), mind a molekula orientációját, forgását jellemző szög (θ) dinamikai változóként voltak beépítve a Hamilton operátorba. Az, hogy a LICI létrejöttére vonatkozó feltételek miképpen módosulnak PDM és merőleges TDM esetében érdekes kérdések és várható, hogy a megváltozott feltételek fizikai mérhető mennyiségekben is megmutatkoznak, elsősorban olyanokban, amelyek információt hordoznak a molekula orientációjáról.

Célom az MgH^+ magdinamikai szimulációjával az volt, hogy túllépve a korábbról elérhető eredményeken, a TDM irányának dinamikára gyakorolt hatását tárgyaljam. Ennek érdekében egy mesterséges (modell) rendszert is szimuláltam, ami minden elektronszerkezeti tulajdonságában megegyezik a valós MgH^+-szal, kivéve a TDM-et, amelyet a molekulatengellyel párhuzamosként kezeltem.

1D és 2D számolásokat végeztem MCTDH használatával, mind a valós, mind a model rendszer esetében. A kapott eredményeim jelentős eltéréseket mutattak a disszociációs fragmentumok szögeloszlásában, ahogy az várható volt. Ezek az eltérések a külső lézertér intenzitásának növelésével nagyobbá válnak és a megfigyelés magyarázata a disszociációs dinamika LICI-képben való értelmezésével, a tér által indukált adiabatikus felületek között létrejövő LICI hatásával szemléletesen magyarázható.

Nyomon követve, hogy időben miképpen változik a magsűrűségfüggvény, a molekula konfigurációs terében nagysűrűségű tartományok formálódása figyelhető meg éppen azon pozíciók közelében, ahol a LICI kialakulásának feltételei a kereszteződés létrejöttét jósolják. Ezek aztán az általuk a rendszerbe bevitt erős nemadiabatikus hatások, ill. az adiabatikus felületek között a LICI közelében megnövekvő csatolás révén a konfigurációs tér ezen tartományában rendkívül hatékony csatornaként viselkednek a két felület közötti populációtranszfer szempontjából. Mindez jelentősen befolyásolja, hogyan zajlik a disszociáció, ami a szögeloszlásra kapott 1D és 2D eredményeim összevetéséből meggyőzően látszik.

A valós és model rendszerek eredményei szintén jelentős különbségekről tanúskodnak, ami a TDM molekulatengelyhez képesti irányának disszociációra gyakorolt hatását bizonyítja. A két rendszerben más és más molekulaorientációk mellett megjelenő disszociációs csúcsok, az azok-

ban megfigyelhető strukúrák mind számot tarthatnak kísérleti érdeklődésre.

A LiF molekula elektronszerkezetének számolása és a maghullámfüggvény bezárása

A LiF molekulával történő számolások motivációját egy nemrégiben megjelent elméleti munka szolgáltatta, amelyben a szerzők külső, permanensen jelen lévő elektromos térrel (gerjesztő avagy *driving field*) a pumpa lézer által magasabb energiállapotba gerjesztett populáció hatékony bezárását figyelték meg a gerjesztett állapotokban. Vizsgálataikban a pumpa lézer által beindított dinamika során a LiF vibrációs alapállapotából történik a gerjesztés a Σ_2 gerjesztett állapotba, ahol az alkalmasan választott gerjesztő tér által deformált potenciálok lehetővé teszik viszonylag hosszú élettartammal populáció fenntartását a gerjesztett állapotban. A szerzők munkájukban különböző energiájú és intenzitású gerjesztést is alkalmaztak és megvizsgálták ezen paraméterek hatását a bezárás hatékonyságára nézve.

Fontos azonban megjegyezni, amire a szerzők is felhívták a figyelmet, hogy eredményeik 1D számolásokra támaszkodnak, azaz a molekula forgását, orientációját nem kezelik szabad dinamikai változóként a szimulációkban. Izgalmas kérdés, hogy a disszociációs dinamika, illetve az ehhez szorosan kapcsolódó bezárási hatékonyság, hogyan változik 2D számolások esetében. Másrészről, a szimulációkban minden esetben figyelembe vett Σ_2 állapot mellett a LiF rendelkezik egy, a Σ_2-höz energetikailag közel eső Π_1 elektronállapottal is. Annak során, hogy a megfelelő energiájú pumpa tér gerjeszti a rendszert a Σ_2 állapotba, a Π_1 állapot is jelentős mértékben gerjesztődik. Ez méginkább megalapozott feltételezés, ha a Π_1 hozzávételekor a $\Sigma_1 \rightarrow \Pi_1$ átmenethez tartozó $\mu_{\Sigma_1\Pi_1}$ TDM-et vizsgáljuk, az ugyanis abban a tartományban, ahol a gerjesztés történik, összemérhető vagy meg is haladja a többi átmenetért felelős TDM-et.

A Π_1 állapot azért lehet jelentős a disszociációs dinamikában és ezáltal a gerjesztő tér által indukált bezárás hatékonyságának alakításában, mert tisztán disszociatív állapot, így várhatóan az ezen állapotba gerjesztett populáció gyorsan képes disszociálni.

A bezáródási hatékonyságot vizsgáló magdinamikai szimulációkat segítve a LiF molekula elektronszerkezetének számolását végeztem, amiben az alapvető hozzájárulásom rejlik ehhez a munkához. Ezek folyamán MOLPRO segítségével számolásokat végeztem a későbbi dinamikai szimulációkban figyelembe vett három elektronállapothoz ($\Sigma_1, \Sigma_2, \Pi_1$) tar-

tozó potenciális energiák, az ezekhez tartozó permanens dipólok és az állapotok közti átmeneti dipólok meghatározására. Ezek jó egyezést mutattak korábbi publikációkban fellelhető értékekkel.

A LiF molekula egyik legérdekesebb elektronszerkezeti tulajdonsága egy elkerült kereszteződés (*avoided crossing*, AC) a Σ_1 és Σ_2 állapotok között és az ezzel kapcsolatos erős nemadiabatikus csatolódás ezen két állapot között az AC közelében. Ennek jelenléte a LiF molekula elektronszerkezetének beépített tulajdonsága, így nemadiabatikus dinamikai folyamatok természetes forrása a rendszerben. Különösen érdekes, hogy az AC hogyan hat kölcsön a 2D-s számolásokban kialakulni képes LICI-vel és az általa indukált nemadiabatikus folyamatokkal.

A magdinamikai számolások eredményei a bezárási effektusra vonatkozóan egyértelműen azt mutatták, hogy a bezáródás veszít hatékonyságából, ha a molekula forgását is figyelembe vesszük, függetlenül attól, hogy a Π_1 állapot jelen van vagy sem. Másrészről, a kétállapot (csak Σ állapotok) és háromállapot (Σ állapotok és a Π állapot) szimulációk eredményei is jelentős eltéréseket mutatnak, bizonyítva, hogy a Π_1 állapot hatása a disszociációs folyamatokra nem elhanyagolható.

Acknowledgements

First and foremost, I would like to express my immense gratitude to my supervisor, dr. Ágnes Vibók. Her help and instructions always steered my PhD studies forward, allowing me to take the best directions with all the works I have done.

I am also incredibly indebted to dr. Gábor Halász for all his help and kindness, always finding the time to answer my questions, be those questions of physical or technical nature. His elaborate approach to physics and numerics has always motivated me to get more thorough on everything I do.

I am greatly thankful to dr. András Csehi. The projects he introduced me to are, in more ways than one, some of the most interesting works I have done. It is also thanks to him that I was introduced to methods of doing my own electronic structure calculations and I thank him for sharing his experience with MOLPRO.

I am glad I have had the opportunity to work with dr. Attila Tóth. Sharing ideas and experience of MCTDH with him were some of the most helpful discussions I have had.

Last, but in no way least, I would like to express how indescribably grateful I am for the support from my dear Mother and Grandmother. All your unwavering support is something I can only hope to be able to return to the fullest some day. But I will try my best.

Thank you.

References

[1] H. Nakamura. *Nonadiabatic Transition: Concepts, Basic Theories and Applications*. World Scienfitic, 2 edition, 2002.

[2] M. Baer. *Beyond Born-Oppenheimer: electronic nonadiabatic coupling terms and conical intersection*. Wiley, 2006.

[3] H. Köppel, W. Domcke, and L. S. Cederbaum. *Multimode Molecular Dynamics Beyond the Born-Oppenheimer Approximation*. John Wiley and Sons, Ltd, 2007.

[4] K. Takatsuka, T. Yonehara, K. Hanasaki, and Y. Arasaki. *Chemical Theory beyond the Born-Oppenheimer Paradigm*. World Scientific, 2015.

[5] F. Hund. Zur Deutung der Molekelspektren. I. *Zeitschrift für Physik*, 40(10):742–764, 1927.

[6] E. Teller. The crossing of potential surfaces. *The Journal of Physical Chemistry*, 41(1):109–116, 1937.

[7] J. von Neumann and E.P. Wigner. Über das verhalten von eigenwertend bei adiabatischen prozessen. *Physikalische Zeitschrift*, 30:467–470, 1939.

[8] N. Moiseyev, M. Šindelka, and L. S. Cederbaum. Laser-induced conical intersections in molecular optical lattices. *Journal of Physics B: Atomic, Molecular and Optical Physics*, 41(22):221001, 2008.

[9] M. Šindelka, N. Moiseyev, and L. S. Cederbaum. Strong impact of light-induced conical intersections on the spectrum of diatomic molecules. *Journal of Physics B: Atomic, Molecular and Optical Physics*, 44(4):045603, 2011.

[10] G. J. Halász, Á. Vibók, M. Šindelka, N. Moiseyev, and Nimrod L. S. Cederbaum. Conical intersections induced by light: Berry phase and wavepacket dynamics. *Journal of Physics B: Atomic, Molecular and Optical Physics*, 44:175102, 08 2011.

[11] G. J. Halász, M. Šindelka, N. Moiseyev, L. S. Cederbaum, and Á. Vibók. Light-Induced Conical Intersections: Topological Phase, Wave Packet Dynamics, and Molecular Alignment. *The Journal of Physical Chemistry A*, 116(11):2636–2643, 2012.

[12] M. Born and R. Oppenheimer. Zur Quantentheorie der Molekeln. *Annalen der Physik*, 84:457 – 484, 1927.

[13] H. J. Werner, P. J. Knowles, G. Knizia, F. R. Manby, and M. Schütz. MOLPRO: A general-purpose quantum chemistry program package. *Wiley Interdisciplinary Reviews: Computational Molecular Science*, 2:242 – 253, 03 2012.

[14] H. D. Meyer, U. Manthe, and L. S. Cederbaum. The multi-configurational time-dependent Hartree approach. *Chemical Physics Letters*, 165:73–78, 1990.

[15] H. D. Meyer, G. A. Worth, and F. Gatti. *Multidimensional Quantum Dynamics: MCTDH Theory and Applications*. Wiley-VCH, Weinheim, 2009.

[16] G. A. Worth, M. H. Beck, A. Jackle, H. D. Meyer, F. Otto, M. Brill, and O. Vendrell. *The Heidelberg MCTDH Package: A set of programs for multi-dimensional quantum dynamics, User's Guide*, version 8, release 4, revision 16 edition, 2018.

[17] M. Galassi, J. Davies, J. Theiler, B. Gough, G. Jungman, P. Alken, M. Booth, and F. Rossi. *GNU Scientific Library Reference Manual*. Network Theory Ltd., United Kingdom, third edition edition, 2018.

[18] P. Atkins and R. Friedman. *Molecular Quantum Mechanics*. Oxford University Press, New York, 3rd edition, 2005.

[19] M. Baer. Adiabatic and diabatic representations for atom-molecule collisions: Treatment of the collinear arrangement. *Chemical Physics Letters*, 35(1):112 – 118, 1975.

[20] I. Mayer. *Simple Theorems, Proofs and Derivations in Quantum Chemisty*. Kluver Academic/Plenum Publishers, New York, 1st edition, 2003.

[21] K. L. Schuchardt, B. T. Didier, T. Elsethagen, L. Sun, V. Gurumoorthi, J. Chase, J. Li, and T. L. Windus. Basis Set Exchange: A Community Database for Computational Sciences. *Journal of Chemical Information and Modeling*, 47(3):1045–1052, 2007.

[22] J. C. Slater. Atomic shielding constants. *Phys. Rev.*, 36:57–64, 1930.

[23] S. F. Boys. Electronic wave functions. I. A general method of calculation for the stationary states of any molecular system. *Proceedings of the Royal Society of London Series A*, 200:542–554, 1950.

[24] B. O. Roos, P. R. Taylor, and P. E. M. Siegbahn. A complete active space SCF method (CASSCF) using a density matrix formulated super-CI approach. *Chemical Physics*, 48(2):157 – 173, 1980.

[25] Y. Frenkel. *Wave Mechanics; Advanced General Theory*. Clarendon Press, Oxford, 1st edition edition, 1934.

[26] A. Jäckle and H.-D. Meyer. Reactive scattering using the multiconfiguration time-dependent Hartree approximation: General aspects and application to the collinear $H+H_2 \rightarrow H_2+H$ reaction. *J. Chem. Phys.*, 102:5605, 1995.

[27] M.-C. Heitz and H.-D. Meyer. Rotational and diffractive inelastic scattering of a diatom on a corrugated surface: A multiconfiguration time-dependent Hartree (MCTDH) study on N_2/LiF(001). *J. Chem. Phys.*, 114:1382–1392, 2001.

[28] R. Milot and A. P. J. Jansen. Ten dimensional wavepacket simulations of methane scattering. *J. Chem. Phys.*, 109:1966, 1998.

[29] A. D. Hammerich, U. Manthe, R. Kosloff, H.-D. Meyer, and L. S. Cederbaum. Time-dependent photodissociation of methyl iodide with five active modes. *J. Chem. Phys.*, 101:5623, 1994.

[30] J.-Y. Fang and H. Guo. Multiconfiguration time-dependent Hartree studies of the CH_3I/MgO photodissociation dynamics. *J. Chem. Phys.*, 101:5831, 1994.

[31] S. Woittequand, C. Toubin, B. Pouilly, M. Monnerville, S. Briquez, and H.-D. Meyer. Photodissociation of a HCl molecule adsorbed on ice. *Chem. Phys. Lett.*, 406:202–209, 2005.

[32] G. A. Worth, H.-D. Meyer, and L. S. Cederbaum. The effect of a model environment on the S_2 absorption spectrum of pyrazine: A wavepacket study treating all 24 vibrational modes. *J. Chem. Phys.*, 105:4412, 1996.

[33] D. Peláez and H.-D. Meyer. On the infrared absorption spectrum of the hydrated hydroxide ($H_3O_2^-$) cluster anion. *Chem. Phys.*, 482:100–105, 2017.

[34] A. Raab, G. Worth, H.-D. Meyer, and L. S. Cederbaum. Molecular dynamics of pyrazine after excitation to the S_2 electronic state using a realistic 24-mode model Hamiltonian. *J. Chem. Phys.*, 110:936–946, 1999.

[35] G. A. Worth, H.-D. Meyer, and L. S. Cederbaum. State filtering by a bath: Up to 24 mode numerically exact wavepacket propagations. *Chem. Phys. Lett.*, 299:451, 1999.

[36] H.-D. Meyer, U. Manthe, and L. S. Cederbaum. The multi-configurational time-dependent Hartree approach. *Chem. Phys. Lett.*, 165:73–78, 1990.

[37] U. Manthe, H.-D. Meyer, and L. S. Cederbaum. Wave-packet dynamics within the multiconfiguration Hartree framework: General aspects and application to NOCl. *J. Chem. Phys.*, 97:3199–3213, 1992.

[38] M. H. Beck, A. Jäckle, G. A. Worth, and H.-D. Meyer. The multiconfiguration time-dependent Hartree method: A highly efficient algorithm for propagating wavepackets. *Physics Reports*, 324:1–105, 2000.

[39] P. A. M. Dirac. Note on exchange phenomena in the Thomas atom. *Mathematical Proceedings of the Cambridge Philosophical Society*, 26(3):376–385, 1930.

[40] G. Floquet. Sur les équations différentielles linéaires à coefficients périodiques. *Annales scientifiques de l'École Normale Supérieure*, 12:47–88, 1883.

[41] S.-I. Chu and D. A. Telnov. Beyond the Floquet theorem: generalized Floquet formalisms and quasienergy methods for atomic and molecular multiphoton processes in intense laser fields. *Physics Reports*, 390(1):1 – 131, 2004.

[42] J. H. Shirley. Solution of the Schrödinger equation with a Hamiltonian periodic in time. *Physical Reviews*, 138:B979–B987, 1965.

[43] S.-I. Chu. Floquet theory and complex quasivibrational energy formalism for intense field molecular photodissociation. *The Journal of Chemical Physics*, 75(5):2215–2221, 1981.

[44] P. H. Bucksbaum, A. Zavriyev, H. G. Muller, and D. W. Schumacher. Softening of the H_2^+ molecular bond in intense laser fields. *Phys. Rev. Lett.*, 64:1883–1886, 1990.

[45] A. Zavriyev, P. H. Bucksbaum, H. G. Muller, and D. W. Schumacher. Ionization and dissociation of H_2 in intense laser fields at 1.064 μm, 532 nm, and 355 nm. *Phys. Rev. A*, 42:5500–5513, 1990.

[46] A. D. Bandrauk and M. L. Sink. Laser induced preassociation in the presence of natural predissociation. *Chemical Physics Letters*, 57(4):569 – 572, 1978.

[47] A. D. Bandrauk and M. L. Sink. Photodissociation in intense laser fields: Predissociation analogy. *The Journal of Chemical Physics*, 74(2):1110–1117, 1981.

[48] E. E. Aubanel, J.-M. Gauthier, and A. Bandrauk. Molecular stabilization and angular distribution in photodissociation of H_2^+ in intense laser fields. *Phys. Rev. A*, 48:2145–2152, 1993.

[49] E. E. Aubanel, A. Conjusteau, and A. D. Bandrauk. Effect of rotations on stabilization in high-intensity photodissociation of H_2^+. *Phys. Rev. A*, 48:R4011–R4014, 1993.

[50] P. Badankó, G. J. Halász, and Á. Vibók. Molecular vibrational trapping revisited: a case study with D_2^+. *Scientific Reports*, 6(31871), 2016.

[51] A. Zavriyev, P. H. Bucksbaum, J. Squier, and F. Saline. Light-induced vibrational structure in H_2^+ and D_2^+ in intense laser fields. *Phys. Rev. Lett.*, 70:1077–1080, 1993.

[52] A. Flores-Riveros and J. F. Rivas-Silva. Variational description of the 3-body Coulomb problem through a correlated Eckart-Gaussian wavefunction. *Brazilian Journal of Physics*, 29:529 – 540, 1999.

[53] Y. Ning and Z.-C. Yan. Variational energy bounds for the hydrogen molecular ion. *Phys. Rev. A*, 90:032516, 2014.

[54] F. V. Bunkin and I. I. Tugov. Multiphoton processes in homopolar diatomic molecules. *Phys. Rev. A*, 8:601–612, 1973.

[55] D. T. Colbert and W. H. Miller. A novel discrete variable representation for quantum mechanical reactive scattering via the S-matrix Kohn method. *The Journal of Chemical Physics*, 96(3):1982–1991, 1992.

[56] D. Kosloff and R. Kosloff. A fourier method solution for the time dependent Schrödinger equation as a tool in molecular dynamics. *Journal of Computational Physics*, 52(1):35 – 53, 1983.

[57] Á. Vibók and G. G. Balint-Kurti. Reflection and transmission of waves by a complex potential—a semiclassical Jeffreys–Wentzel–Kramers–Brillouin treatment. *The Journal of Chemical Physics*, 96(10):7615–7622, 1992.

[58] U. V. Riss and H.-D. Meyer. Calculation of resonance energies and widths using the complex absorbing potential method. *Journal of Physics B: Atomic, Molecular and Optical Physics*, 26(23):4503–4535, 1993.

[59] U. V. Riss and H.-D. Meyer. Investigation on the reflection and transmission properties of complex absorbing potentials. *The Journal of Chemical Physics*, 105(4):1409–1419, 1996.

[60] G. J. Halász, A. Csehi, Á. Vibók, and L. S. Cederbaum. Influence of light-induced conical intersection on the photodissociation dynamics of D_2^+ starting from individual vibrational levels. *The Journal of Physical Chemistry A*, 118(51):11908–11915, 2014.

[61] G. Herzberg and H. C. Longuet-Higgins. Intersection of potential energy surfaces in polyatomic molecules. *Discuss. Faraday Soc.*, 35:77–82, 1963.

[62] H. C. Longuet-Higgins. The Intersection of Potential Energy Surfaces in Polyatomic Molecules. *Proceedings of the Royal Society of London Series A*, 344:147–156, 1975.

[63] C. A. Mead and D. G. Truhlar. On the determination of Born-Oppenheimer nuclear motion wave functions including complications due to conical intersections and identical nuclei. *The Journal of Chemical Physics*, 70(5):2284–2296, 1979.

[64] V. M. Berry. Quantal phase factors accompanying adiabatic changes. *Proc. R. Soc. Lond. A*, 392:45–57, 1984.

[65] M. Baer and R. Englman. A modified Born-Oppenheimer equation: application to conical intersections and other types of singularities. *Chemical Physics Letters*, 265(1):105 – 108, 1997.

[66] R. Baer, D. M. Charutz, R. Kosloff, and M. Baer. A study of conical intersection effects on scattering processes: The validity of adiabatic single-surface approximations within a quasi-Jahn–Teller model. *The Journal of Chemical Physics*, 105(20):9141–9152, 1996.

[67] S. C. Althorpe, T. Stecher, and F. Bouakline. Effect of the geometric phase on nuclear dynamics at a conical intersection: Extension of a recent topological approach from one to two coupled surfaces. *The Journal of Chemical Physics*, 129(21):214117, 2008.

[68] L. Joubert-Doriol, I. G. Ryabinkin, and A. F. Izmaylov. Geometric phase effects in low-energy dynamics near conical intersections: A study of the multidimensional linear vibronic coupling model. *The Journal of Chemical Physics*, 139(23):234103, 2013.

[69] H. A. Jahn, E. Teller, and F. G. Donnan. Stability of polyatomic molecules in degenerate electronic states – I - Orbital degeneracy. *Proceedings of the Royal Society of London. Series A - Mathematical and Physical Sciences*, 161(905):220–235, 1937.

[70] R. Englman. *The Jahn-Teller Effect in Molecules and Crystals*. Wiley-Interscience, 1972.

[71] N. Mukunda and R. Simon. Quantum kinematic approach to the geometric phase. I. General formalism. *Annals of Physics*, 228(2):205 – 268, 1993.

[72] G. J. Halász, P. Badankó, and Á. Vibók. Geometric phase of light-induced conical intersections: adiabatic time-dependent approach. *Molecular Physics*, 116(19-20):2652–2659, 2018.

[73] U. M. Ascher and L. M. Petzold. *Computer Methods for Ordinary Differential Equations and Differential-Algebraic Equations*. SIAM: Society for Industrial and Applied Mathematics, 1998.

[74] G. J. Halász, Á. Vibók, and L. S. Cederbaum. Direct signature of light-induced conical intersections in diatomics. *The Journal of Physical Chemistry Letters*, 6(3):348–354, 2015.

[75] T. Szidarovszky, G. J. Halász, A. G. Császár, L. S. Cederbaum, and Á. Vibók. Direct signatures of light-induced conical intersections on the field-dressed spectrum of Na_2. *The Journal of Physical Chemistry Letters*, 9(11):2739–2745, 2018.

[76] A. Bertelsen, I. S. Vogelius, S. Jørgensen, R. Kosloff, and M. Drewsen. Photo-dissociation of cold MgH^+ ions. *The European Physical Journal D - Atomic, Molecular, Optical and Plasma Physics*, 31(2):403–408, 2004.

[77] P. F. Staanum, K. Højbjerre, P. S. Skyt, A. K. Hansen, and M. Drewsen. Rotational laser cooling of vibrationally and translationally cold molecular ions. *Nature Physics*, 6:271–274, 2010.

[78] M. Tacconi, F. A. Gianturco, E. Yurtsever, and D. Caruso. Cooling and quenching of $^{24}MgH^+(X^1\Sigma^+)$ by $^4He(^1S)$ in a coulomb trap: A quantum study of the dynamics. *Phys. Rev. A*, 84:013412, 2011.

[79] S. Kahra, G. Leschhorn, M. Kowalewski, A. Schiffrin, E. Bothschafter, W. Fuß, R. de Vivie-Riedle, R. Ernstorfer, F. Krausz, R. Kienberger, and T. Schaetz. A molecular conveyor belt by controlled delivery of single molecules into ultrashort laser pulses. *Nature Physics*, 8(3):238–242, 2012.

[80] D. Leibfried. Quantum state preparation and control of single molecular ions. *New Journal of Physics*, 14(2):023029, 2012.

[81] N. Deb, B. R. Heazlewood, M. T. Bell, and T. P. Softley. Blackbody-mediated rotational laser cooling schemes in MgH^+, DCl^+, HCl^+ LiH and CsH. *Phys. Chem. Chem. Phys.*, 15:14270–14281, 2013.

[82] J. M. Berglund, M. D., and C. P. Koch. Femtosecond wavepacket interferometry using the rotational dynamics of a trapped cold molecular ion. *New Journal of Physics*, 17(2):025007, 2015.

[83] F. Wolf, Y. Wan, J. C. Heip, F. Gebert, C. Shi, and P. O. Schmidt. Non-destructive state detection for quantum logic spectroscopy of molecular ions. *Nature*, 530:457–460, 2016.

[84] P. V. Demekhin and L. S. Cederbaum. Light-induced conical intersections in polyatomic molecules: General theory, strategies of exploitation, and application. *The Journal of Chemical Physics*, 139(15):154314, 2013.

[85] A. Csehi, G. J. Halász, L. S. Cederbaum, and Á. Vibók. Intrinsic and light-induced nonadiabatic phenomena in the NaI molecule. *Phys. Chem. Chem. Phys.*, 19:19656–19664, 2017.

[86] P. Badankó, G. J. Halász, L. S. Cederbaum, Á. Vibók, and A. Csehi. Communication: Substantial impact of the orientation of transition dipole moments on the dynamics of diatomics in laser fields. *The Journal of Chemical Physics*, 149(18):181101, 2018.

[87] H. H. Telle and A. J. Tambini. Photofragmentation of NaI at 355 nm: excited-state symmetries. *Journal of Physics B: Atomic, Molecular and Optical Physics*, 22(12):L315–L319, 1989.

[88] J. L. Collier and H. H. Telle. Resonance ionization mass spectroscopy of atomic products formed by photodissociation of sodium iodide molecules. *Rapid Communications in Mass Spectrometry*, 7(6):519–523, 1993.

[89] O. Vasyutinskii, K. Korovin, and B. Picheev. Formation of oriented cesium atoms upon photodissociation of CsI molecules via the second excited state. *Optics and Spectroscopy*, 82:171–175, 1997.

[90] K. Korovin, A. A. Veselov, E. Mikheev, O. Vasyutinskii, and D. Zimmermann. Determination of the amplitudes and phases of the scattering matrix upon photodissociation of molecules. *Optics and Spectroscopy*, 99:880–889, 2005.

[91] K. Korovin, E. Heinecke, A. Patzer, T. Liebig, O. Vasyutinskii, and D. Zimmermann. Photofragment space distribution in the photodissociation of NaI in the spectral range 315-370 nm: The role of molecular axis rotation. *The European Physical Journal D*, 44:57–63, 2007.

[92] Y. Hu, Y. Guo, Y. Wang, Z. Chen, X. Sun, J. Feng, T.-M. Lu, E. Wertz, and J. Shi. A review on low dimensional metal halides: Vapor phase epitaxy and physical properties. *Journal of Materials Research*, 32(21):3992–4024, 2017.

[93] W. Langheinrich, B. Spangenberg, and H. Beneking. Nanostructure fabrication using lithium fluoride films as an electron beam resist. *Journal of Vacuum Science & Technology B: Microelectronics and Nanometer Structures Processing, Measurement, and Phenomena*, 10(6):2868–2872, 1992.

[94] F. Bonfigli, N. J. Hartley, Y. Inubushi, M. Koenig, T. Matsuoka, S. Makarov, R. M. Montereali, E. Nichelatti, N. Ozaki, M. Piccinini, S. Pikuz, T. Pikuz, D. Sagae, M. A. Vincenti, M. Yabashi, and T. Yabuuchi. Photoluminescence properties and characterization of LiF-based imaging detector irradiated by 10 keV XFEL beam. In *Optics Damage and Materials Processing by EUV/X-ray Radiation VII*, volume 11035, pages 56 – 66. International Society for Optics and Photonics, SPIE, 2019.

[95] H.-J. Werner and W. Meyer. MCSCF study of the avoided curve crossing of the two lowest $^1\Sigma^+$ states of LiF. *The Journal of Chemical Physics*, 74(10):5802–5807, 1981.

[96] A. D. Bandrauk and J. M. Gauthier. Infrared multiphoton dissociation of lithium fluoride by a coupled equation method. *The Journal of Physical Chemistry*, 93(22):7552–7554, 1989.

[97] A. D. Bandrauk and J. M. Gauthier. Above-threshold molecular photodissociation in ionic molecules: a numerical simulation. *J. Opt. Soc. Am. B*, 7(8):1420–1427, 1990.

[98] A. Csehi, G. J. Halász, L. S. Cederbaum, and Á. Vibók. Competition between light-induced and intrinsic nonadiabatic phenomena in diatomics. *The Journal of Physical Chemistry Letters*, 8(7):1624–1630, 2017.

[99] Y. Arasaki, Y. Mizuno, S. Scheit, and K. Takatsuka. Stark-assisted quantum confinement of wavepackets. a coupling of nonadiabatic interaction and CW-laser. *The Journal of Chemical Physics*, 144(4):044107, 2016.

[100] A. Tóth, P. Badankó, G. J. Halász, Á. Vibók, and A. Csehi. Importance of the lowest-lying Π electronic state in the photodissociation dynamics of LiF. *Chemical Physics*, 515:418 – 426, 2018.

[101] A. Hofmann and R. de Vivie-Riedle. Adiabatic approach for ultrafast quantum dynamics mediated by simultaneously active conical intersections. *Chemical Physics Letters*, 346(3):299 – 304, 2001.

[102] A. J. C. Varandas. Accurate ab initio potential energy curves for the classic Li-F ionic-covalent interaction by extrapolation to the complete basis set limit and modeling of the radial nonadiabatic coupling. *The Journal of Chemical Physics*, 131(12):124128, 2009.

[103] J. F. Triana, D. Peláez, and J. L. Sanz-Vicario. Entangled photonic-nuclear molecular dynamics of LiF in quantum optical cavities. *The Journal of Physical Chemistry A*, 122(8):2266–2278, 2018.